DSPACE

https://dspace.org/

# Solvothermal synthesis of amorphous TiO2-BiOBr-Bentonite heterostructures for the abatement of phenol in water under visible light irradiation

**Dlamini, Menelisi Celumusa**

**2022**

https://hdl.handle.net/10539/34551

Downloaded from a DSpace repository. https://dspace.org/

# Solvothermal synthesis of amorphous $TiO_2$-BiOBr-Bentonite heterostructures for the abatement of phenol in water under visible light irradiation




**By**

**Menelisi Celumusa Dlamini**
**Student number: 1490516**

A dissertation submitted in fulfillment of the requirements for the degree of
**Master of Science**
in the Faculty of Science, University of the Witwatersrand, Johannesburg.

**June 2022**

**Supervisor: Dr John Moma**

**Co-supervisor: Dr Manoko Maubane-Nkadimeng**

# Declaration

The work reported in this dissertation for a Master of Science degree is original and was carried out in the School of Chemistry at the University of the Witwatersrand. It is my unaided work under the supervision of Dr John Moma and Dr Manoko Maubane-Nkadimeng and has not been submitted for any qualification in any institution. Pictures and ideas of others used in this work have been acknowledged accordingly.

Signed: 

**Menelisi Celumusa Dlamini**

On this 8th day of June 2022

# Abstract

A simplistic solvothermal process has been used to fabricate novel amorphous $TiO_2$-BiOBr-Bentonite (A-$TiO_2$-BiOBr-Bt) multidimensional photocatalysts with A-$TiO_2$:BiOBr:Bt mass ratios fixed at 1:3:4, 1:1:2, and 3:1:4 respectively. The obtained photocatalysts were characterized using techniques such as Powder X-Ray Diffraction (PXRD), Scanning electron microscopy (SEM), Transmission Electron Microscopy (TEM), X-Ray Photoelectron Spectroscopy (XPS), Brunauer-Emmett-Teller (BET) analysis, Ultra-Violet Visible (UV-vis) spectroscopy, Photoluminescence spectroscopy (PL), pH drift method, and Thermo-Gravimetric Analysis (TGA). The A-$TiO_2$-BiOBr-Bt heterostructure with an A-$TiO_2$:BiOBr:Bt mass ratio of 1:1:2 ($Ti_1Bi_1Bt_2$) displayed the highest BET surface area, low bandgap, and sufficiently low electron-hole pair recombination rate. The high number of A-$TiO_2$-BiOBr p-n heterojunctions, and the Ti-O-Si and Bi-O-Si bonds between A-$TiO_2$-BiOBr and Bt in $Ti_1Bi_1Bt_2$ lowered its electron-hole recombination rate and enhanced its visible light-harvesting ability. It is for these reasons that $Ti_1Bi_1Bt_2$ exhibited the best photocatalytic activity compared to the other ternary heterostructures with different mass ratios. Within 70 min of visible light irradiation, 150 mg of $Ti_1Bi_1Bt_2$ gave 100% conversion of 100 mL of 20 ppm of phenol with a pseudo-first-order rate constant of 0.0322 $min^{-1}$ at pH 4.0. Scavenging experiments were conducted and it was demonstrated that superoxide radicals ($O_2^{\bullet-}$) and electrons ($e^-$) were the most dominant reactive oxidation species (ROS) responsible for the phenol photodegradation process while holes ($h^+$) and hydroxyl radicals ($OH^{\bullet}$) also exerted appreciable participation.

# Dedications

This work is dedicated to my family, especially my elder brother Nhlanhla Dlamini for their moral, material, and financial support throughout my Post Graduate studies at the University of the Witwatersrand.

# Acknowledgments

This work would have been impossible to do without the generous support of some persons. I would like to thank my supervisors Dr John Moma, and Dr Manoko Maubane-Nkadimeng for their support, guidance, insight, and reviewing all the research papers from this work. They allowed me to think independently and share my thoughts openly with them. I would also like to thank Prof Neil Coville for his input in reviewing and curating the published review paper. I would also acknowledge Dr Pumza Mente for securing some of the chemicals used in this work and for reviewing and curating the paper submitted for publication in the Journal of Industrial and Engineering Chemistry. Profound thanks also go to Mbongiseni L. Dlamini who helped with the HPLC analysis presented in this work and Dr Rudolph Erasmus who helped with PL analysis.

For moral, material, and financial support, I would like to thank my family and close friends especially Prosper Makhanya and Mafihlo Dlamini.

I am also grateful to members of Lab 117 and the CATMAT group (Wits University) for all their contributions in discussions and constructive criticism during seminars.

My sincere gratitude also goes to the microscopy and microanalysis unit (MMU) for TEM and PXRD analyses, the school of Chemical Engineering & Metallurgy for SEM analysis, and the National Metrology Institute of South Africa (NMISA) for XPS analysis. Special thanks to Motlatsi Phali, Thuli Buthelezi, and Boitumelo Tlhaole for their help in some of the analyses presented in this study.

This work is based on a research supported in part by the National Research Foundation of South Africa (Grant Numbers: 122205) and the University of the Witwatersrand.



# Publications and Presentations

**Publications**

1. **Menelisi C. Dlamini**, Manoko S. Maubane-Nkadimeng and John Moma; The use of $TiO_2$/Clay heterostructures in the photocatalytic remediation of water containing organic pollutants: A Review; Journal of Environmental Chemical Engineering 9, 106546, https://doi.org/10.1016/j.jece.2021.106546.
2. **Menelisi C. Dlamini**, Mbongiseni L. Dlamini, Pumza Mente, Boitumelo Tlhaole, Rudolph Erasmus, Manoko S. Maubane-Nkadimeng and John Moma; Photocatalytic abatement of phenol on amorphous $TiO_2$-BiOBr-Bentonite heterostructures under visible light irradiation, Journal of Industrial and Engineering Chemistry (2022); https://doi.org/10.1016/j.jiec.2022.04.023.

**Presentations**

1. Title: Solvothermal synthesis of oxygen vacancy-rich amorphous $TiO_2$-BiOBr-Bentonite heterostructures for the abatement of phenol in water. **Poster presentation**. Authors: **Menelisi C. Dlamini**, Manoko Maubane-Nkadimeng, and John Moma. Conference: $10^{th}$ Annual Nanosciences Young Researchers' Symposium (NYRS-2020/21)-National, 7-8 October 2021, Virtual Symposium, University of the Witwatersrand.
2. Title: Solvothermal synthesis of oxygen vacancy-rich amorphous $TiO_2$-BiOBr-Bentonite heterostructures for the abatement of phenol in water. **Oral presentation**. Authors: **Menelisi C. Dlamini**, Manoko Maubane-Nkadimeng, and John Moma. Conference: The 31st Catalysis Society of South Africa (CATSA) international conference, 7-10 November 2021, Virtual Symposium, University of KwaZulu-Natal.

# Table of contents

**Declaration**.....ii

**Abstract**..... iii

**Dedications**.....iv

**Acknowledgments**.....v

**Publications and Presentations**.....vi

**Table of contents**.....vii

**List of Figures**.....xi

**List of Tables**.....xiv

**List of abbreviations and nomenclature**.....xvi

**Chapter 1: Introduction to the study**.....1

1.0. Introduction.....1

1.1. Background.....1

1.2. Problem statement.....3

1.3. Justification.....5

1.4. Purpose of the study.....6

1.4.1. Aims of the study.....6

1.4.2. Objectives.....6

1.5. Scope of this dissertation.....6

References.....7

**Chapter 2: Literature review**.....12

2.0. Introduction.....12

2.1. Background $TiO_2$ photocatalysis in water remediation.....12

2.2. Dynamics of Single electron transfer $TiO_2$ photocatalysis.....16

2.3. Efficient amorphous $TiO_2$ photocatalysts.....19

2.4. Amorphous $TiO_2$-BiOBr heterostructures .....20
2.5. General chemistry of clay as support of $TiO_2$ photocatalysts .....23
2.6. Processes used to synthesize $TiO_2$/clay composites .....25
2.7. Review on $TiO_2$/Bentonite composites for water remediation .....28
2.8. Amorphous $TiO_2$-BiOBr/clay photocatalysts .....35
2.9. Reaction kinetics of $TiO_2$/clay composites in the photodegradation of organic water contaminants .....36
2.10. Phenol degradation mechanism on $TiO_2$/clay composites .....38
2.11. Fabricating usable $TiO_2$/clay products .....38
2.12. Overview of the latest trends in the fabrication of effective $TiO_2$/clay composites .....39
References .....42

**Chapter 3: Synthesis and characterization of A-$TiO_2$-BiOBr-Bt heterostructures and analytical methods used in testing their photocatalytic activity** .....61
3.0. Introduction .....61
3.1. Materials .....61
3.2. Synthesis .....61
3.3. Characterization .....63
3.4. Photodegradation experiments .....64
3.5. Analytical methods .....65
References .....66

**Chapter 4: Characterization results** .....67
4.0. Introduction .....67
4.1. PXRD .....68
4.2. SEM analyses .....71
4.3. TEM analysis .....75

4.4. XPS ..... 76
4.5. $N_2$ adsorption-desorption studies ..... 80
4.6. UV-Vis analysis ..... 82
4.7. PL analysis ..... 83
4.8. Point of zero charge ($pH_{PZC}$) determination ..... 85
4.9. TGA analysis ..... 90
4.10. Conclusion ..... 91
References ..... 93

**Chapter 5: Photocatalysis of phenol and optimization of operational conditions** ..... 99
5.0. Introduction ..... 99
5.1. Selecting a catalyst ..... 99
5.2. Effect of the initial solution pH on the abatement of phenol ..... 102
5.3. Influence of photocatalyst dosage on the removal of phenol ..... 103
5.4. The effect of initial concentration on the removal of phenol ..... 104
5.5. Kinetic Studies ..... 105
5.6. Catalyst reusability studies ..... 107
5.7. Free radical scavenging experiments ..... 108
5.8. Proposed charge transfer mechanism and phenol photodegradation ..... 110
5.9. Conclusion ..... 111
References ..... 112

**Chapter 6: General conclusions and recommendations** ..... 115
6.0. Introduction ..... 115
6.1. Conclusion ..... 115
6.2. Recommendations ..... 116
References ..... 117

**Appendix A: Supplementary information** ..... 118

# List of Figures

## Chapter 2

**Figure 2.1.** Crystal structures of (a) rutile, (b) anatase, (c) bronze, and (d) brookite adapted from Aravindan et al. [41]. .....13

**Figure 2.2.** 216-atom models of solid (300 K, 3.57 g/cm$^3$) A-$TiO_2$, as obtained from AIMD simulations.$TiO_4$, $TiO_5$, $TiO_6$, and $TiO_7$ polyhedra are shown in yellow, red, blue, and green, respectively [44].....14

**Figure 2.3.** Coordination number distribution in the amorphous $TiO_2$ model for (a) titanium and (b) oxygen, when the cutoff distance for calculating the neighbors $r$=2.6 Å.....15

**Figure 2.4.** Anticipated application of $TiO_2$ photocatalytic water treatment in various localities. .....15

**Figure 2.5.** ROS generated during $TiO_2$ photocatalysis [55]. .....17

**Figure 2.6.** Schematic model of principal processes in the application of single-electron $TiO_2$ photocatalysis using anatase where CB: conduction band; VB: valence band; $A_{ad}$: adsorbed electron acceptor; $D_{ad}$: adsorbed electron donor [57], and timescales for each process Fujishima et al. [58]. .....18

**Figure 2.7.** A typical Mott-Schottky measurement plot A-$TiO_2$ [59]. .....19

**Figure 2.8.** The Mott-Schottky measurement of BiOBr [59].....21

**Figure 2.9.** Crystal structure of the BiOBr systems (space group *P4/nmm, $D_{4h}$* symmetry) with stoichiometric Br−Bi−O−Bi−Br bilayers stacked along the c axis [83]. .....21

**Figure 2.10.** The formation and photocatalytic mechanism scheme of the amorphous $TiO_2$/BiOBr composite [78]. .....23

**Figure 2.11.** The arrangement of tetrahedral (T) and octahedral (O) layers in 1:1 and 2:1 clays [95].....24

**Figure 2.12.** Classification of cationic clays (phyllosilicates), adapted from Bailey et al. [96]. .....24

**Figure 2.13.** Structure showing the tetrahedral and octahedral sheets of Mt and the top view of Mt layers [141].....28

**Figure 2.14.** Synthesis scheme for $Fe_2O_3$-Bt-$TiO_2$ [146]. .....31

**Figure 2.15.** (a) HRTEM image of (b) g-$C_3N_4$, (c) $TiO_2$/Bt nanocomposite, (d) g-$C_3N_4$-$TiO_2$/Bt nanocomposite (40 CTB) and (d) high resolution image of $TiO_2$ showing lattice fringes [151]. .....33

**Figure 2.16.** The synthesis of the oxygen vacancy-rich amorphous $TiO_2$-BiOBr-sepiolite catalysts [59]. ..... 35
**Figure 2.17.** Possible mechanism of the enhanced photocatalytic performance for A$TiO_2$-BiOBr-Sepiolite towards formaldehyde and oxytetracycline under visible light irradiation [59]. ..... 36
**Figure 2.18.** (a) Reaction mechanism of the photodegradation of phenol on $TiO_2$-pyrophyllite composite proposed El Gaidoumi [157] and (b) their follow-up study [158]. ..... 38

## Chapter 3

**Figure 3.1.** Synthesis scheme for A-$TiO_2$-BiOBr-Bt heterostructures..... 62
**Figure 3.2.** Design of the Lelesil photochemical reactor system used..... 64

## Chapter 4

**Figure 4.1.** PXRD diffraction patterns of Bt and the different photocatalysts. The (♣) designates the quartz peaks in the Bt diffraction pattern. ..... 70
**Figure 4.2.** The SEM images of Bt and the different photocatalysts (a)-(j), the EDS spectra, and atomic (%) of $Ti_1Bi_1Bt_2$ are shown in (k) and (l). ..... 73
**Figure 4.3.** EDS elemental mapping images of $Ti_1Bi_1$. ..... 75
**Figure 4.4.** Elemental mapping images of $Ti_1Bi_1Bt_2$ and the area selected for the analysis.. 75
**Figure 4.5.** TEM images of Bt and the different photocatalysts. ..... 76
**Figure 4.6.** XPS spectra of $Ti_1Bi_1Bt_2$, $Ti_1Bi_1Bt_2$-400, $Ti_1Bi_1$, BiOBr and A-$TiO_2$: (a) survey of $Ti_1Bi_1Bt_2$, (b) survey of $Ti_1Bi_1Bt_2$-400, (c) Br 3d, (d) Bi 4f, (e)-(f) Ti 2p, (g) O 1s and (h) Si 2p..... 79
**Figure 4.7.** $N_2$ adsorption-desorption isotherms of raw Bt and the different photocatalysts. 81
**Figure 4.8.** The UV-Vis spectra and Tauc plots of Bt and the different photocatalysts. ..... 82
**Figure 4.9.** The PL spectra of Bt and the different photocatalysts..... 84
**Figure 4.10.** $pH_{final}$ vs $pH_{initial}$ graph of raw Bt and the different photocatalysts. ..... 86
**Figure 4.11.** Interactions of Ala and Trp with the noncalcined $TiO_2$ surface [51]. ..... 89
**Figure 4.12.** TGA (a) and DTG (b) curves of Bt and the different materials. ..... 91

## Chapter 5

**Figure 5.1.** Removal of phenol under visible light irradiation using Bt and the different photocatalysts. ..... 101

**Figure 5.2.** Removal of phenol on $Ti_1Bi_1Bt_2$ under visible light irradiation in different pH environments. ..... 102

**Figure 5.3.** Resonance stabilization of a phenolate anion through the delocalization of the electron pair [7]. ..... 103

**Figure 5.4.** Influence of $Ti_1Bi_1Bt_2$ dosage on the removal of phenol under visible light irradiation. ..... 104

**Figure 5.5.** Influence of initial concentration on the removal of phenol over $Ti_1Bi_1Bt_2$ under visible light irradiation. ..... 105

**Figure 5.6.** Pseudo-first-order reaction kinetics of the photodegradation of 20 ppm phenol over 150 mg of $Ti_1Bi_1Bt_2$. ..... 106

**Figure 5.7.** Reusability performance of $Ti_1Bi_1Bt_2$ during the first six photocatalytic runs towards phenol. ..... 107

**Figure 5.8.** Photocatalytic removal of phenol on $Ti_1Bi_1Bt_2$ in the presence of scavengers of ROS. ..... 109

**Figure 5.9.** A proposed conceptual charge transfer mechanism for the degradation of phenol on $Ti_1Bi_1Bt_2$. ..... 111

## Appendix A

**Figure S1**. A typical chromatogram of an external phenol standard with a 3.25 min retention time used in calibrating the concentration of phenol during HPLC analyses. ..... 118

**Figure S2**. Pore size distribution curves of Bt and all the photocatalysts. ..... 119

**Figure S3**. PXRD diffractogram of $Ti_1Bi_1Bt_2$ before and after being used in 6 photocatalytic cycles. ..... 120

**Figure S4**. SEM micrograph of $Ti_1Bi_1Bt_2$ after being used in 6 photocatalytic cycles. ..... 120

**Figure S5**. EDS spectra of $Ti_1Bi_1Bt_2$ after being used in 6 photocatalytic cycles. ..... 121

**Figure S6**. BET isotherm and pore size distribution curve for $Ti_1Bi_1Bt_2$ after being used in 6 photocatalytic cycles. ..... 121

# List of Tables

## Chapter 2

**Table 2.1.** Structural and physical properties of rutile, anatase, brookite, and Bronze $TiO_2$ [41,42]. ..... 13

**Table 2.2.** $TiO_2$/Bt composites commonly applied in the degradation of various organic water pollutants. ..... 34

## Chapter 3

**Table 3.1.** Amounts of TBOT, $Bi(NO_3)_3 \cdot 5H_2O$, and KBr that were used in the fabrication of the ternary composites. ..... 62

**Table 3.2.** Operational conditions optimized for effective phenol photocatalysis. ..... 65

## Chapter 4

**Table 4.1.** Chemical analysis showing the approximate atomic % of the different elements in Bt and the different photocatalysts obtained from EDS analysis. ..... 74

**Table 4.2.** BET Surface Area, Pore Volume, and Pore size of Bt and the different photocatalysts ..... 81

**Table 4.3.** Bandgap energies of Bt and the different photocatalysts extracted from the Tauc plots. ..... 83

**Table 4.4.** The $pH_{PZC}$ of Bt and the different photocatalysts ..... 86

## Chapter 5

**Table 5.1.** Rate constant ($K_{app}$) for the photodegradation of phenol using $Ti_1Bi_1Bt_2$. ..... 106

**Table 5.2.** Phenol conversion efficiency on $Ti_1Bi_1Bt_2$ after 6 photocatalytic cycles. ..... 108

**Table 5.3.** Phenol conversion efficiency on $Ti_1Bi_1Bt_2$ in the presence of scavengers for ROS. ..... 109

## Chapter 6

**Table 6.1.** $TiO_2$/clay-based composites applied in the removal of phenol under visible light .....115

## Appendix A

**Table S1.** Elemental composition of $Ti_1Bi_1Bt_2$ after being used in 6 photocatalytic cycles. 121

**Table S2.** BET Specific Surface Area, Pore Volume, and Pore size of reused $Ti_1Bi_1Bt_2$. ...122

# List of abbreviations and nomenclature

| Abbreviation | Description |
|---|---|
| AIMD | *ab-initio* Molecular Dynamics |
| Ala | Alanine |
| AO | Ammonium Oxalate |
| AOPs | Advanced Oxidation Processes |
| A-$TiO_2$ | Amorphous Titania |
| BET | Brunauer-Emmett-Teller |
| BJH | Barrett-Joyner-Halenda |
| BQ | Benzoquinone |
| Bt | Bentonite |
| *ca.* | Approximately |
| CB | Conduction Band |
| CEC | Cation Exchange Capacity |
| COD | Chemical Oxygen Demand |
| CTAB | Cetyltrimethylammonium bromide |
| DL | Detection Limit |
| DPCHs | Delaminated Porous Clay Heterostructures |
| DRS | Direct Reflectance Spectroscopy |
| DTG | Derivative Thermogravimetry |
| EDS | Energy Dispersive X-ray Spectroscopy |
| EG | Ethylene Glycol |
| EIS | Electron Impedance Spectroscopy |
| EPR | Electron Paramagnetic Resonance |
| EPs | Emerging Pollutants |
| EtOH | Ethanol |
| EU | European Union |
| $e^-$ | Electron |
| FESEM | Field Electron Scanning Electron Microscopy |
| g-$C_3N_4$ | Graphitic Carbon Nitride |
| GO | Graphene Oxide |

| | |
|---|---|
| HPLC | High Pressure Liquid Chromatography |
| HPLC/MS | High Pressure Liquid Chromatography/ Mass Spectrometry |
| $h^+$ | hole |
| $H_2O_2$ | hydrogen peroxide |
| IPA | Isopropanol |
| IR | Infrared |
| IUPAC | International Union of Pure and Applied Chemistry |
| LRC | Linear Regression Curve |
| MO | Methyl orange |
| Mt | Montmorillonite |
| NPs | Nanoparticles |
| $^1O_2$ | Singlet oxygen |
| $O_2^{\bullet-}$ | Superoxide radical |
| OECD | Organization for Economic Cooperation and Development |
| $OH^{\bullet}$ | Hydroxyl radical |
| OV | Oxygen Vacancies |
| PAHs | Polycyclic Aromatic Hydrocarbons |
| PCHs | Porous Clay Heterostructures |
| PCPs | Personal Care Products |
| $pH_{pzc}$ | point of zero charge |
| PL | Photoluminescence |
| PMS | Peroxymonosulfate |
| POPs | Persistent Organic Pollutants |
| ppb | parts per billion |
| ppm | parts per million |
| PXRD | Powder X-Ray Diffraction |
| ROS | Reactive Oxidation Species |
| $R^2$ | Variational Constant |
| SEM | Scanning Electron Microscopy |
| TBOT | Tetrabutyl titanate |

| | |
|---|---|
| TEM | Transmission Electron Microscopy |
| TGA | Thermo-Gravimetric Analysis |
| $TiO_2$-B | Bronze $TiO_2$ |
| $Ti_xBi_yBt_z$ | Amorphous $TiO_2$-BiOBr-Bentonite |
| Trp | Tryptophan |
| USEPA | US Environmental Protection Agency |
| UV | Ultraviolet |
| UV-Vis | Ultraviolet-Visible |
| VB | Valence Band |
| WHO | World Health Organization |
| XPS | X-Ray Photoelectron Spectroscopy |

# Chapter 1: Introduction to the study

## 1.0.Introduction

This is the first chapter of the dissertation which presents the background, problem statement, justification, purpose, and scope of the study. It contains excerpts from a paper published as **Menelisi C. Dlamini**, Manoko S. Maubane-Nkadimeng, and John Moma; The use of $TiO_2$/clay heterostructures in the photocatalytic remediation of water containing organic pollutants: A Review; Journal of Environmental Chemical Engineering 9, 106546, https://doi.org/10.1016/j.jece.2021.106546. The paper was curated and reviewed by Prof Neil Coville.

## 1.1. Background

The provision of clean water is among the principal national imperatives for governments of various countries, including South Africa. However, the main environmental challenge has been the increasing number and amounts of hazardous contaminants that are released from manufacturing industries [1], farms [2], our homes [3], and various localities directly into water and land. The general trend is that most anthropogenic land pollutants are washed by water runoff into streams and rivers adding to the multifarious anthropogenic pollutants that are directly deposited into such waterways and then collectively transported into oceans and seas. Rivers have been identified as the main channel for 85% of land-based natural materials and anthropogenic contaminants that enter the oceans [4].

Dyes and phenolic compounds are the anthropogenic organic pollutants drawing the most attention owing to their high level of toxicity and preponderance in various textile and industrial wastewaters. Such pollutants are also found in wastewaters from other localities where they are used as raw materials or useful products. It has been reported that there exist more than 10 000 types of dyes and their annual production of over 700 000 tons and *ca.* 200 000 tonnes is discharged untreated into the environment due to inefficient dyeing processes resulting in colored water [5,6]. Phenolic compounds are dominant pollutants in wastewaters of refineries, coking operations, coal processing, petrochemical plants, pharmaceuticals, plastics, wood products, paint, pulp, and paper industries [7].

Among phenolic compounds, phenol is widely used as a raw material for the production of various useful products in various industries [7,8] and this is why its global production is projected to reach 14.5 million tons per year in 2022 [4]. When phenol is poorly discharged from industries it becomes ubiquitous in the environment mostly in aquatic ecosystems due to its high water solubility, environmental mobility, and chemical stability [9,10]. Moreover, phenol is known to cause ecological harm and scare to human health even in low concentrations in the order of mg/L [11]. The main challenge with phenol water pollution detection is that it is colorless [12] unlike pollutants such as dyes where their presence in water is visible through the discoloration of water [13]. It can only be observed by human senses at high concentrations through its unpleasant phenolic odor and taste [14,15]. Its toxicity is in the 10-24 mg/L range for humans and 9-25 mg/L range for fish, and the lethal blood concentration is about 150 mg/100 mL [16].

On account of the health and environmental concerns associated with careless disposal of partially treated or untreated phenolic water into waterways, several environmental regulatory bodies such as the World Health Organization (WHO), US Environmental Protection Agency (USEPA), Canadian Environmental Protection, and the European Union (EU) have listed phenol as a priority pollutant and have set purification standards [17–20]. The World Health Organization has set the phenol concentration limit to 1 μg/L for water to be considered safe for drinking [17]. The USEPA has set a water purification standard of less than 1 ppb of phenol for surface waters, while the EU has set 0.5 ppb for mineral waters, 0.5 ppm for wastewater emissions, and 1 mg/L for sewerage systems [20]. In South Africa, phenol has been found at a concentration of up to 140 ng/L in the buffalo river in the Eastern Cape [21] and in the 69-163 μg/L range in selected wastewater treatment plants [22], and these concentrations are higher than the USEPA recommended limits.

To meet the set phenol regulatory standards in water, several separation and destructive phenol abatement methods such as adsorption, extraction, distillation, air oxidation processes, chemical oxidation, electrochemical oxidation, membrane-based processes and photo-oxidation processes such as photocatalysis can be applied [7]. Of these methods, semiconductor photocatalysis (a catalytic photo-oxidation process) is considered ideal as it uses atmospheric oxygen to nonselectively degrade refractory pollutants without chemical input or output [23] and also has high effectiveness to cost ratio [24] making it a financially sound water treatment technology for small-scale applications in areas that do not have access to clean drinking water.

The other methods are either slow, facilitate incomplete phenol removal, are energy-intensive, or require expensive equipment and chemicals.

Among semiconductor photocatalysts used in the treatment of water containing refractory organic pollutants, $TiO_2$ is revered as the standard photocatalyst [25]. Although crystalline $TiO_2$ has been widely investigated for water remediation, recently there is a growing interest in the application of amorphous $TiO_2$ (A-$TiO_2$) due to its high adsorption capacity and better ability to avert electron-hole recombination [26].

Recently interest is on the rational design and fabrication of robust $TiO_2$-based photocatalysts through coupling $TiO_2$ with suitable supports and composite formers. Clays are one of the suitable supports for $TiO_2$ catalytic materials and several studies reviewed by Dlamini et al. [27] have reported on the rational design and fabrication of efficient binary, ternary and quaternary clay heterostructures of crystalline and A-$TiO_2$ with good visible light absorption capacity, low electron-hole recombination, and good adsorption capacity for the removal of the various organic pollutants.

$TiO_2$/clay-based photocatalysts are widely used as adsorbents, photocatalysts, and antifouling agents in membranes [27] and this has strong relevance to the future of photocatalytic water remediation for both industrial and domestic applications. Our present work is on the in situ growth of A-$TiO_2$-BiOBr structures on bentonite (Bt) resulting in a ternary structure with high oxygen vacancies, low excitation energy, better adsorption capacity, and high surface area. Since Bt lacks permanent porosity, the in situ growth of A-$TiO_2$-BiOBr within its galleries induces permanent porosity in the clay resulting in a porous multidimensional structure that effectively removes organic water pollutants through a “capture, degrade and release” process. The advantage of such catalysts is that they are cheap, effective, and fabricated from cheap materials and resist fouling through a dispersion-photodegradation synergy mechanism previously reported on $TiO_2$@Palygorskite [28].

## 1.2. Problem statement

The scarcity of clean drinking water and poor sanitation are fundamental global concerns because they have a direct bearing on human health, mortality rate, and life expectancy. In 2015, it was reported that almost 2 million children below 5 years of age die yearly due to the lack of clean water and proper sanitation [29] and around 748 million people did not have access to clean drinking water sources [30]. In 2012, the Organization for Economic Cooperation and Development (OECD) projected that the global manufacturing water demand

was expected to increase by almost 400% while domestic water demand was to increase by almost 130% between the years 2000 to 2050 [31]. The projected increase in the manufacturing water demand is inherently associated with an increase in the release of some anthropogenic hazardous wastes into effluent streams of industries and processing plants which may pollute drinking sources in various communities. Most industrial hazardous organic pollutants include dyes [3], phenols [32], triazines [33], multifarious polycyclic aromatic hydrocarbons [29,32], multifarious volatile organic pollutants [32] among others.

Recently attention is on a new class of water pollutants with no regulatory status despite having adverse consequences on the environment and human health which are known as "emerging pollutants" or "contaminants of emerging concerns" [34,35]. From the norman database, there are more than 700 chemicals listed as emerging pollutants (EPs) grouped into 20 classes [36,37]. Some of the EPs are found in our personal care products (PCPs) that we use daily [36,38] and most of them fall into the category of refractory organic pollutants making them have serious consequences primarily in human and animal health mostly aquatic animals. In most cases, EPs find their way to waterways and water sources from urban and agricultural run-offs and are sometimes discharged from wastewater plants after ineffective treatment [39]. Given the preponderance of toxic organic pollutants of different types and forms that are released into water sources, there is a need to develop efficient catalysts and systems involving cheap and effective Advanced Oxidation Processes (AOPs) so that the pollutants can be removed or inactivated in a non-selective manner in aquatic systems. In our context, AOPs are water treatment methods applied at room temperature and normal pressure which act through the in situ generation of effective oxidizing agents at concentrations that allow them to remediate polluted water [40]. A majority of AOPs are facilitated by heterogeneous catalysts, and their effectiveness is strongly reliant on the quality and properties of the stand-alone, composite, and combination of catalysts. The effective treatment of wastewaters allows sustainable industrial development with limited pollution.

Currently, researchers are making strides in the development of robust, porous green chemistry catalysts that are cheap, easy to fabricate and recover, are applied under mild conditions, and are capable of degrading concentrated pollutants completely into harmless substances. This class of catalysts also includes semiconductor photocatalysts immobilized on clays which is the basis of this study. Phenol has been chosen as a model pollutant to test the photocatalytic activity of A-$TiO_2$-BiOBr-Bt due to its stability and resistance to removal using conventional methods which renders it a good representative for persistent organic pollutants.

## 1.3. Justification

Owing to the resistance of recalcitrant hazardous organic water pollutants like phenol to abatement using universal water treatment processes and the overhead costs and high energy consumption of efficient industrial wastewater treatment technologies, there is a need for the development of cheaper and efficient "green chemistry" catalysts and systems for water remediation through AOPs.

In South Africa, phenols and other persistent organic pollutants (POPs) have been quantified in rivers and freshwater systems [21,22], dams [41], and wastewater treatment plants [22] at concentrations higher than the USEPA recommended limits. Visible light active $TiO_2$/clay-based photocatalysts form part of a class of "green chemistry" catalysts and systems that can be applied in the treatment of water containing such refractory organic pollutants. The ascendancy of applying visible light active $TiO_2$/clay-based photocatalysts in water remediation is that they can be applied directly in real-life matrices and can also be used as platform materials for the development of various engineered materials such as photoresponsive thin films, membranes, and photoreactors [27]. Moreover, $TiO_2$/clay photocatalysts also have potential use as reactive coating materials for the inner wall of clay pots to purify drinking water in rural communities that depend on rivers as the sole source of water.

As $TiO_2$/clay photocatalysis research evolves, the main goal is to fabricate affordable porous catalysts with high specific surface area, high visible light-harvesting ability, lower electron-hole recombination rate, higher adsorption capacity, and outstanding ability to degrade nuisance organic pollutants [27]. Our take is on the fabrication of oxygen vacancy rich A-$TiO_2$-BiOBr-Bt multidimensional heterostructures with enhanced visible light phenol photodegradation owing to the ternary heterojunction between A-$TiO_2$, BiOBr, and Bt. To test the photocatalytic performance of the multidimensional photocatalyst, phenol was chosen as a model colorless refractory pollutant due to its stability and ubiquity in the environment. A similar photocatalyst, A-$TiO_2$-BiOBr-Sepiolite with a low bandgap of 2.53 eV was fabricated and tested on the degradation of formaldehyde and oxytetracycline under visible light [26]. Apart from using Bt due to its abundance in South Africa instead of sepiolite, this study also interrogates the effect of varying the amounts of A-$TiO_2$ and BiOBr with fixed bentonite mass on the properties and performance of the A-$TiO_2$:BiOBr:Bt photocatalysts.

## 1.4. Purpose of the study

*1.4.1. Aims of the study*

This study proposes that the in situ growth of A-$TiO_2$ and BiOBr semiconductors on Bt gives a ternary multidimensional heterostructure with improved visible light-harvesting ability, reduced electron-hole recombination rate, improved adsorption capacity, and consequently enhanced conversion efficiency of phenol under visible light irradiation. The above hypothesis leads to the main aim of the project which is:

- To fabricate, characterize and apply visible light photoresponsive A-$TiO_2$-BiOBr-Bt heterostructures in the photocatalytic degradation of phenol as a model refractory pollutant.

*1.4.2. Objectives*

- To fabricate A-$TiO_2$-BiOBr-Bt photocatalysts using a one-pot solvothermal process.
- To characterize the as-synthesized materials using various techniques such as PXRD, SEM, EDS, TEM, XPS, $N_2$-Adsorption and desorption, UV-Vis spectroscopy, PL spectroscopy, pH drift, and TGA.
- To investigate the photocatalytic performance of the as-synthesized materials.
- To evaluate the effect of operating conditions such as pH, catalyst dosage, and initial phenol concentration on the efficiency of the phenol photodegradation process on the most effective photocatalyst.
- To study the reaction kinetics of the phenol photodegradation on the most effective photocatalyst under optimum operating conditions.
- To study the effect of reusing the most effective photocatalyst on its effectiveness and structural integrity.
- To identify the most dominant reactive oxidation species (ROS) responsible for the photodegradation process using different radical scavengers.

## 1.5. Scope of this dissertation

This study is focused on the synthesis, characterization, and application of A-$TiO_2$-BiOBr-Bt heterostructures in the photodegradation of phenol in water. The scope of this project is limited to executing the specific aims and objectives listed above.

## References


[1] K. Sellami, A. Couvert, N. Nasrallah, R. Maachi, N. Tandjaoui, M. Abouseoud, A. Amrane, Bio-based and cost-effective method for phenolic compounds removal using cross-linked enzyme aggregates, J. Hazard. Mater. 403 (2021) 124021. https://doi.org/10.1016/j.jhazmat.2020.124021.

[2] A. Buah-Kwofie, M.S. Humphries, X. Combrink, J.G. Myburgh, Accumulation of organochlorine pesticides in fat tissue of wild Nile crocodiles (Crocodylus niloticus) from iSimangaliso Wetland Park, South Africa, Chemosphere. 195 (2018) 463–471. https://doi.org/10.1016/j.chemosphere.2017.12.084.

[3] S. Hena, L. Gutierrez, J. Croué, Removal of pharmaceutical and personal care products (PPCPs) from wastewater using microalgae: A review, J. Hazard. Mater. 403 (2021) 124041. https://doi.org/10.1016/j.jhazmat.2020.124041.

[4] Z. Zhao, X. Gong, L. Zhang, M. Jin, Y. Cai, X. Wang, Riverine transport and water-sediment exchange of polycyclic aromatic hydrocarbons (PAHs) along the middle-lower Yangtze River, China, J. Hazard. Mater. 403 (2021) 123973. https://doi.org/10.1016/j.jhazmat.2020.123973.

[5] M.R. Al-mamun, S. Kader, M.S. Islam, M.Z.H. Khan, Photocatalytic activity improvement and application of UV-$TiO_2$ photocatalysis in textile wastewater treatment : A review, J. Environ. Chem. Eng. 7 (2019) 103248. https://doi.org/10.1016/j.jece.2019.103248.

[6] H. Zhu, R. Jiang, J. Li, Y. Fu, S. Jiang, J. Yao, Magnetically recyclable $Fe_3O_4$/$Bi_2S_3$ microspheres for effective removal of Congo red dye by simultaneous adsorption and photocatalytic regeneration, Sep. Purif. Technol. 179 (2017) 184–193. https://doi.org/10.1016/j.seppur.2016.12.051.

[7] S. Mohammadi, A. Kargari, H. Sanaeepur, K. Abbassian, A. Najafi, E. Mofarrah, Phenol removal from industrial wastewaters: a short review, Desalin. Water Treat. (2014) 1–20. https://doi.org/10.1080/19443994.2014.883327.

[8] M. Choquette-Labbé, W.A. Shewa, J.A. Lalaman, S. Shanmugam, Photocatalytic Degradation of Phenol and Phenol Derivatives Using a Nano-$TiO_2$ Catalyst: Integrating Quantitative and Qualitative Factors Using Response Surface Methodology, Water. 6 (2014) 1785–1806. https://doi.org/10.3390/w6061785.

[9] J.S. Park, M.T. Brown, T. Han, Phenol toxicity to the aquatic macrophyte Lemna paucicostata, Aquat. Toxicol. 106–107 (2012) 182–188.

https://doi.org/10.1016/j.aquatox.2011.10.004.

[10] J. Moma, J. Baloyi, T. Ntho, Influence of Operational Parameters and Kinetic Modelling of Catalytic Wet Air Oxidation of Phenol by Al/Zr Pillared Clay Catalyst, Iran. J. Chem. Chem. Eng. 38 (2019) 189–203.

[11] M.C. Tomei, D. Mosca Angelucci, E. Clagnan, L. Brusetti, Anaerobic biodegradation of phenol in wastewater treatment: achievements and limits, Appl. Microbiol. Biotechnol. (2021) 2195–2224. https://doi.org/10.1007/s00253-021-11182-5.

[12] S. Kundu, B. Satpati, T. Kar, S.K. Pradhan, Microstructure characterization of hydrothermally synthesized PANI/$V_2O_5{\cdot}nH_2O$ heterojunction photocatalyst for visible-light-induced photodegradation of organic pollutants and non-absorbing colorless molecules, J. Hazard. Mater. 339 (2017) 161–173. https://doi.org/10.1016/j.jhazmat.2017.06.034.

[13] M.L. Dlamini, M. Bhaumik, K. Pillay, A. Maity, Heliyon Polyaniline nanofibers, a nanostructured conducting polymer for the remediation of Methyl orange dye from aqueous solutions in fixed-bed column studies, Heliyon. 7 (2021) e08180. https://doi.org/10.1016/j.heliyon.2021.e08180.

[14] L. Fuentes-López, C. Amézquita-Marroquín, L. Edith Barba-Ho, C.H. Cruz-Vélez, P. Torres-Lozada, Application of double filtration with activated carbon for the removal of phenols in drinking water treatment processes, J. Water Supply Res. Technol. 67 (2018) 227–235. https://doi.org/10.2166/aqua.2018.165.

[15] M.L. Davì, F. Gnudi, Phenolic compounds in surface water, Water Res. 33 (1999) 3213–3219. https://doi.org/10.1016/S0043-1354(99)00027-5.

[16] J.P. Kulkarni, Sunil J, and Kaware, Review on research for removal of phenol from wastewater, Int. J. Sci. Res. Publ. 3 (2013) 1–5.

[17] A. Barrios-Martinez, E. Barbot, B. Marrot, P. Moulin, N. Roche, Degradation of synthetic phenol-containing wastewaters by MBR, J. Membr. Sci. 281. 281 (2006) 288–296. https://doi.org/10.1016/j.memsci.2006.03.048.

[18] EPA's Guide for Industrial Waste Management, Protecting Surface Water (2000) 1–478.

[19] K.W. Taylor, R. Chénier, Introduction to ecological risk assessments of priority substances under the Canadian Environmental Protection Act, 1999, Hum. Ecol. Risk Assess. 9 (2003) 447–451. https://doi.org/10.1080/713609917.

[20] G. Busca, S. Berardinelli, C. Resini, L. Arrighi, Technologies for the removal of phenol from fluid streams: A short review of recent developments, J. Hazard. Mater. 160 (2008) 265–288. https://doi.org/10.1016/j.jhazmat.2008.03.045.

[21] A. Yahaya, O.O. Okoh, F.O. Agunbiade, A.I. Okoh, Occurrence of phenolic derivatives in Buffalo River of Eastern Cape South Africa: Exposure risk evaluation, Ecotoxicol. Environ. Saf. 171 (2019) 887–893. https://doi.org/10.1016/j.ecoenv.2019.01.037.

[22] O.O. Olujimi, O.S. Fatoki, J.P. Odendaal, A.P. Daso, Chemical monitoring and temporal variation in levels of endocrine-disrupting chemicals (priority phenols and phthalate esters) from selected wastewater treatment plant and freshwater systems in the Republic of South Africa, Microchem. J. 101 (2012) 11–23. https://doi.org/10.1016/j.microc.2011.09.011.

[23] J. Chen, F. Qiu, W. Xu, S. Cao, H. Zhu, General Recent progress in enhancing photocatalytic efficiency of $TiO_2$-based materials, Appl. Catal. A Gen. 495 (2015) 131–140. https://doi.org/10.1016/j.apcata.2015.02.013.

[24] C.B. Molina, E. Sanz-Santos, A. Boukhemkhem, B. Jorge, C. Belver, J.J. Rodriguez, Removal of emerging pollutants in aqueous phase by heterogeneous Fenton and photo-Fenton with $Fe_2O_3$-$TiO_2$-clay heterostructures, Environ. Sci. Pollut. Res. 27 (2020) 38434–38445. https://doi.org/doi.org/10.1007/s11356-020-09236-8.

[25] L.G. Devi, R. Kavitha, A review on nonmetal ion-doped titania for the photocatalytic degradation of organic pollutants under UV/solar light: Role of photogenerated charge carrier dynamics in enhancing the activity, Appl. Catal. B Environ. 140–141 (2013) 559–587. https://doi.org/10.1016/j.apcatb.2013.04.035.

[26] X. Hu, C. Li, J. Song, S. Zheng, Z. Sun, Multidimensional assembly of oxygen vacancy-rich amorphous $TiO_2$-BiOBr-sepiolite composite for rapid elimination of formaldehyde and oxytetracycline under visible light, J. Colloid Interface Sci. 574 (2020) 61–73. https://doi.org/10.1016/j.jcis.2020.04.035.

[27] M.C. Dlamini, M.S. Maubane-Nkadimeng, J.A. Moma, The use of $TiO_2$/clay heterostructures in the photocatalytic remediation of water containing organic pollutants: A review, J. Environ. Chem. Eng. 9 (2021) 106546. https://doi.org/10.1016/j.jece.2021.106546.

[28] C. Li, L. Yan, Y. Li, D. Zhang, M. Bao, L. Dong, $TiO_2$@ palygorskite composite for the efficient remediation of oil spills via a dispersion-photodegradation synergy, Front. Environ. Sci. Eng. 15 (2021) 72. https://doi.org/10.1007/s11783-020-1365-3

[29] J. Eliasson, The rising pressure of global water shortages, Nature. 517 (2015) 6. https://doi.org/10.1038/517006a.

[30] WWAP, The United Nations World Water Development Report 2015: Water for a Sustainable World; UNESCO: Paris, 2015.

[31] V. Marchal, R. Dellink, D. Van Vuuren, C. Clapp, J. Chateau, B. Magn´e, J. van Vliet, OECD Environmental Outlook to 2050, Organ. Econ. Coop. Dev. OECD (2011). https://www.oecd.org/env/indicators-modelling-outlooks/49844953.pdf.

[32] A. Mishra, A. Mehta, S. Basu, Clay supported $TiO_2$ nanoparticles for photocatalytic degradation of environmental pollutants: A review, J. Environ. Chem. Eng. 6 (2018) 6088–6107. https://doi.org/10.1016/j.jece.2018.09.029.

[33] S. Komtchou, A. Dirany, P. Drogui, N. Delegan, M. Ali, E. Khakani, D. Robert, P. Lafrance, Chemosphere Degradation of atrazine in aqueous solution with electrophotocatalytic process using $TiO_{2-x}$ photoanode, Chemosphere. 157 (2016) 79–88. https://doi.org/10.1016/j.chemosphere.2016.05.022.

[34] Y. Patiño, E. Díaz, S. Ordóñez, E. Gallegos-Suarez, A. Guerrero-Ruiz, I. Rodríguez-Ramos, Adsorption of emerging pollutants on functionalized multiwall carbon nanotubes, Chemosphere. 136 (2015) 174–180. https://doi.org/10.1016/j.chemosphere.2015.04.089.

[35] I.C. Vasilachi, D.M. Asiminicesei, D.I. Fertu, M. Gavrilescu, Occurrence and fate of emerging pollutants in water environment and options for their removal, Water. 13 (2021) 1–34. https://doi.org/10.3390/w13020181.

[36] V. Geissen, H. Mol, E. Klumpp, G. Umlauf, M. Nadal, M. van der Ploeg, S.E.A.T.M. van de Zee, C.J. Ritsema, Emerging pollutants in the environment: A challenge for water resource management, Int. Soil Water Conserv. Res. 3 (2015) 57–65. https://doi.org/10.1016/j.iswcr.2015.03.002.

[37] D.D. Snow, D.A. Cassada, M.L. Larsen, N.A. Mware, X. Li, M.D. Alessio, Y. Zhang, J.B. Sallach, Detection, Occurrence and Fate of Emerging Contaminants in Agricultural Environments, Water Environ. Res. 89 (2021) 897–920. https://doi.org/10.2175/106143017X15023776270160.

[38] A. Gogoi, P. Mazumder, V. Kumar, G.G.T. Chaminda, A. Kyoungjin, M. Kumar, Groundwater for Sustainable Development Occurrence and fate of emerging contaminants in water environment: A review, Groundw. Sustain. Dev. 6 (2018) 169–180. https://doi.org/10.1016/j.gsd.2017.12.009.

[39] D.B. Miklos, C. Remy, M. Jekel, K.G. Linden, J.E. Drewes, U. Hübner, Evaluation of advanced oxidation processes for water and wastewater treatment – A critical review, Water Res. 139 (2018) 118–131. https://doi.org/10.1016/j.watres.2018.03.042.

[40] M.A. Oturan, J.J. Aaron, Advanced oxidation processes in water/wastewater treatment: Principles and applications. A review, Crit. Rev. Environ. Sci. Technol. 44 (2014) 2577–

2641. https://doi.org/10.1080/10643389.2013.829765.

[41] L.N. Nthunya, N.P. Khumalo, A.R. Verliefde, B.B. Mamba, S.D. Mhlanga, Quantitative analysis of phenols and PAHs in the Nandoni Dam in Limpopo Province, South Africa : A preliminary study for dam water quality management, Phys. Chem. Earth. 112 (2019) 228–236. https://doi.org/10.1016/j.pce.2019.02.003.

# Chapter 2: Literature review

## 2.0. Introduction

This second chapter of the dissertation discusses the application of $TiO_2$ and $TiO_2$/clay-based composites in photocatalytic water remediation processes. This chapter consists of extensive excerpts from a paper published as **Menelisi C. Dlamini**, Manoko S. Maubane-Nkadimeng, and John Moma; The use of $TiO_2$/Clay heterostructures in the photocatalytic remediation of water containing organic pollutants: A Review; Journal of Environmental Chemical Engineering 9, 106546, https://doi.org/10.1016/j.jece.2021.106546. The paper was curated and reviewed by Prof Neil Coville.

## 2.1. Background $TiO_2$ photocatalysis in water remediation

Semiconductor photocatalysis is one the most ideal and attractive technologies with interesting applications in energy, environmental remediation processes, and catalysis [1–3]. This is because semiconductor photocatalysis is based on the ability of semiconductors to harvest the inexhaustible, safe, and clean solar energy from the sun for application in cheap and sustainable technologies [4]. It has been exploited in several areas of photo-electrochemistry including energy production processes such as catalytic water splitting, energy storage in batteries, and photocatalytic reduction of $CO_2$ into valuable solar fuels such as $CH_4$, $HCO_2H$, $CH_2O$, and $CH_3OH$ [5]. It has also been applied in the photodegradation of air pollutants and inactivation of airborne pathogens [6–8]. Furthermore, $TiO_2$-based materials have wide applications in the photocatalytic removal of multifarious pollutants in water such as refractory organic and inorganic water pollutants [9], toxic metals, and the inactivation of pathogenic and virulent waterborne microorganisms [10–12].

While all the above-mentioned applications of semiconductor photocatalysis in energy production and various environmental remediation processes have strong relevance in solving today's problems and for sustainable development, our interest is on the application of photocatalysts in the abatement of refractory organic water pollutants. The competence of semiconductor photocatalysis in the abatement of refractory organic pollutants in water is due to its ability to nonselectively degrade all organic pollutants into final products without producing toxic byproducts [13]. Semiconductors such as $TiO_2$ [14,15], $Fe_2O_3$ [16,17], $CeO_2$ [18,19], CuO [20], $WO_3$ [21], ZnO [22], $SnO_2$ [23,24], ZrO [25], $BiVO_4$ [26,27], BiOBr

[28,29], $SiO_2$ [25,30], $WS_2$ [31], graphitic carbon nitride [32–34], graphene oxide [34] and carbon quantum dots [35] among others, have been tested in the photocatalytic remediation of water containing multifarious environmental pollutants. Generally, metal oxide-based semiconductors are promising candidates for photocatalytic applications due to their light absorption properties, charge-transfer characteristics, extended lifetime of excited-state, and suitable electronic structures [36].

Of all semiconductor photocatalysts studied, $TiO_2$ is the most studied and established ideal photocatalyst for water remediation due to its low price, high oxidation potential, physical and chemical stability, non-toxicity [4,37–40], suitable band edge [39,40], water insolubility, multifaceted electronic properties, surface acid-base properties, super hydrophilicity and so on [40]. In 2015, more than 13 crystalline $TiO_2$ polymorphs were reportedly in existence. However, in nature, crystalline $TiO_2$ exists in four crystallographic phases viz: rutile, anatase, brookite, and bronze ($TiO_2$-B) [41] and these four have strong relevance in photocatalytic applications. The crystal structures of rutile, anatase, brookite, and bronze $TiO_2$ are shown in **Figure 2.1**. The structural properties and physical properties i.e. shapes, space groups, lattice parameters, and densities of the rutile, anatase, brookite, and bronze $TiO_2$ phases are shown in **Table 2.1**.

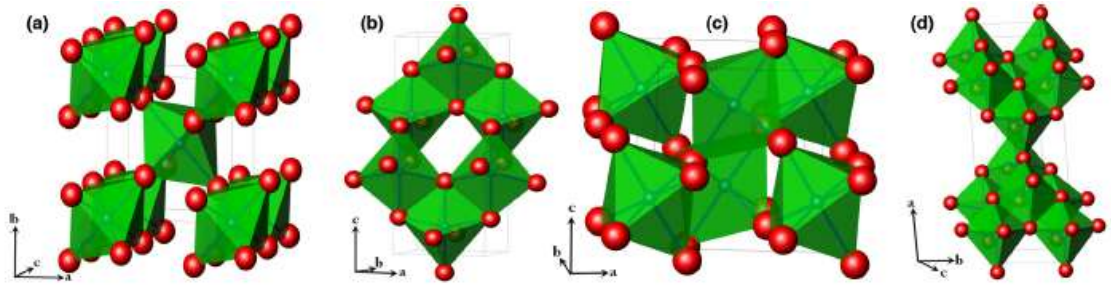



**Figure 2.1.** Crystal structures of (a) rutile, (b) anatase, (c) bronze, and (d) brookite adapted from Aravindan et al. [41].

**Table 2.1. Structural and physical properties of rutile, anatase, brookite, and Bronze $TiO_2$ [41,42].**

| Structure | Shape | Space group | Lattice parameters | Density ($g/cm^3$) |
|---|---|---|---|---|
| Rutile | Tetragonal | $P4_2/mnm$ | a=4.59, c=2.96 | 4.13 |
| Anatase | Tetragonal | $I4_1/amd$ | a=3.79, c=9.51 | 3.79 |

| | | | | |
|---|---|---|---|---|
| Brookite | Orthorhombic | *Pbca* | a=9.17, b=5.46, c=5.14 | 3.99 |
| Bronze ($TiO_2$-B) | Monoclinic | *C2/m* | a=12.17, b=3.74, c=6.51 | 3.64 |

Lately, there has been considerable interest in the use of amorphous $TiO_2$ (A-$TiO_2$) for various photocatalytic applications owing to the abundant disorders and defects including oxygen vacancies and $Ti^{3+}$ in its structure which accept electrons during photoactivation availing an alternative electron-hole pair separation pathway [43,44]. Ideally, perfectly crystalline $TiO_2$ constitutes $TiO_6$ octahedral units [45,46] such that each O atom has three Ti neighbors forming $Ti_3O$ units [46]. The $Ti_3O$ units assume a Y-shaped conformation in rutile, an almost T-shaped conformation in anatase, and both T- and Y-shaped conformations exist in brookite [47]. However, in A-$TiO_2$ some Ti atoms have 5-fold or 7-fold coordination to O atoms; and O atoms have 2-fold or 4-fold coordination to Ti atoms hence the loss of periodicity in the unit cells [46]. Several studies using *ab initio* molecular dynamics (AIMD) simulations have been done to get the structure of A-$TiO_2$ and the structure presented in **Figure 2.2** was reported by Mavračić et al. [44].

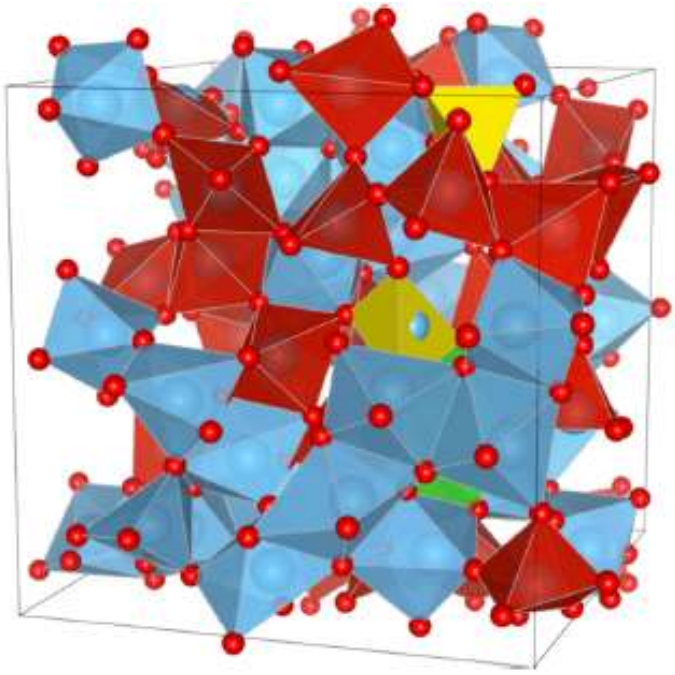


**Figure 2.2.** 216-atom models of solid (300 K, 3.57 g/cm$^3$) A-$TiO_2$, as obtained from AIMD simulations.$TiO_4$, $TiO_5$, $TiO_6$, and $TiO_7$ polyhedra are shown in yellow, red, blue, and green, respectively [44].

In another separate but related study by Pham et al. [46], the proportions of the ideal ($TiO_6$ and $OTi_3$) and non-ideal coordination numbers were calculated. They reported that the proportion of octahedral $TiO_6$ units in the amorphous phase remains higher than that of the non-ideal units ($TiO_4$, $TiO_5$, and $TiO_7$) and $OTi_3$ exert dominance compared to $OTi_2$ and $OTi_4$ units as shown in **Figure 2.3**.

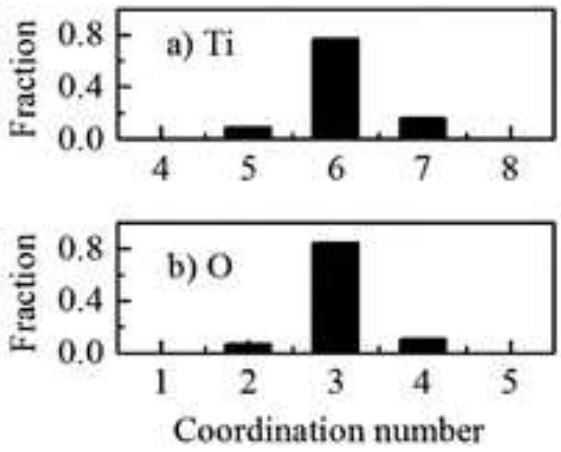



**Figure 2.3.** Coordination number distribution in the amorphous $TiO_2$ model for (a) titanium and (b) oxygen, when the cutoff distance for calculating the neighbors $r$=2.6 Å.

The application of crystalline and A-$TiO_2$ as environmental remediation photocatalysts in various areas has been explored, and **Figure 2.4** below shows some multifarious places where $TiO_2$ has been applied or has potential application as an environmental remediation photocatalyst.

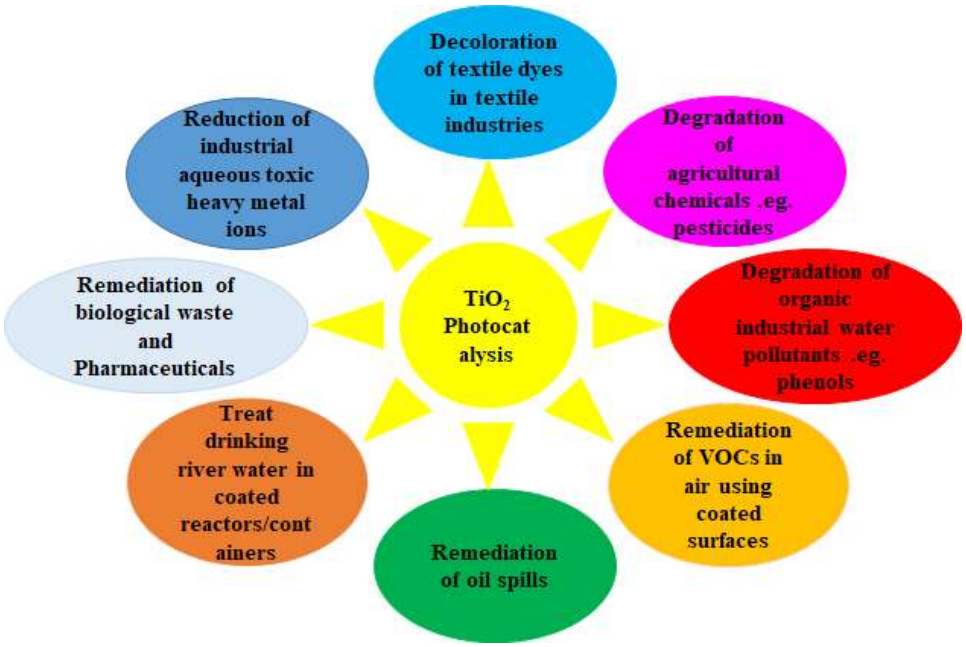



**Figure 2.4.** Anticipated application of $TiO_2$ photocatalytic water treatment in various localities.

## 2.2. Dynamics of Single electron transfer $TiO_2$ photocatalysis

A common property among semiconductors, like $TiO_2$, is that they lack a continuum of interband states and therefore allow an extended lifetime of photogenerated electrons and holes after photoactivation, and this property is exploited in interfacial single electron transfer applications [48,49]. $TiO_2$ photocatalysis is a surface phenomenon based on the interfacial redox reactions of electrons and holes on the surface of $TiO_2$ photocatalysts to generate active reactive oxidation species (ROS). Before the surface redox processes can occur, several dynamical steps have to occur through the simplistic four-step tandem process: light-harvesting, charge generation, charge separation, and transport to the surface for the surface redox reactions [40,50]. However, charge recombination processes occur within the volume of the photocatalyst within femtoseconds to microseconds and these are deactivating, as only photogenerated charge carriers that reach the surface of $TiO_2$ can be used for photocatalytic redox reactions [50–52]. The electron-hole recombination rate is suppressed by several point defects within the $TiO_2$ structure mainly oxygen vacancies and $Ti^{3+}$ [53,54]. The oxygen vacancies arise to maintain electrical neutrality when two Ti ions are in 3+ states [54]. The net result is that $Ti^{3+}$, oxygen vacancies, and Ti interstitials as intrinsic defects within $TiO_2$ crystal structures lower the electron-hole recombination rate during their transport within the $TiO_2$ catalyst bulk [54].

**Figure 2.5** shows the main intrinsic ROS responsible for the degradation of organic pollutants which include holes ($h^+$), electrons ($e-$), hydroxyl radicals ($OH^\bullet$), superoxide anion radicals ($O_2^{\bullet-}$), hydrogen peroxide ($H_2O_2$), and singlet oxygen ($^1O_2$) [55]. Hydroxyl radicals, in particular, are extremely reactive species capable of attacking most organic molecules, with rate constants usually in the order of $10^6$-$10^9$ $M^{-1}s^{-1}$ [56]. As can be seen in **Figure 2.5**, $h^+$ and $e-$ are the primary ROS, and the other ROS are generated through intricate series of redox reactions involving $h^+$ and $e-$.




**Figure 2.5.** ROS generated during $TiO_2$ photocatalysis [55].

Qian et al. [51] and Kohtani et al. [57] proposed a slightly different mechanism and used **equations 2.1-2.8** and **Figure 2.6** to resolve and detail the principal simplistic reactions involved in $TiO_2$ photocatalysis. The proposed $TiO_2$ photocatalysis mechanism included the contributions of various structural parameters including crystallographic defects and titanol groups (Ti-OH) and **Figure 2.6** provides their approximate time scales.

Electron–hole pair photogeneration

$$TiO_2 + h\nu \rightarrow TiO_2\,(e^-_{CB} + h^+_{VB}) \qquad 2.1$$

Trapping conduction band (CB) electrons ($e^-_{CB}$) at defect $Ti^{4+}$ sites($Ti^{4+}_{ds}$)

$$Ti^{4+}_{ds} + h\nu \rightarrow Ti^{3+}_{ds} \qquad 2.2$$

Trapping valence band holes ($h^+_{VB}$) at terminal Ti–OH or surface Ti–O–Ti sites Ti-$O_S$H

$$Ti - O_sH \text{ or } Ti - O_s - Ti + h^+_{VB} \rightarrow Ti - O_sH^{\bullet+} \text{ or } Ti - O_s^{\bullet+} - Ti \qquad 2.3$$

Reduction of adsorbed electron acceptor ($A_{ad}$) with $e^-_{CB}$ at reduction sites

$$e^-_{CB} + A_{ad} \rightarrow A^{\bullet-}_{ad} \qquad 2.4$$

Reduction of $A_{ad}$ with electrons trapped at defect sites ($Ti^{3+}_{ds}$)

$$Ti^{3+}_{ds} + A_{ad} \rightarrow Ti^{4+}_{ds} + A^{\bullet-}_{ad} \qquad 2.5$$

Oxidation of adsorbed electron donor ($D_{ad}$) by trapped holes at oxidation sites

$$Ti - O_sH^{\bullet+} \text{ or } Ti - O_s^{\bullet+} - Ti + D_{ad} \rightarrow Ti - O_sH \text{ or } Ti - O_s - Ti + D_{ad}^{\bullet+} \quad 2.6$$

Recombination of $e_{CB}^-$ with trapped holes

$$e_{CB}^- + Ti - O_sH^{\bullet+} \text{ or } Ti - O_s^{\bullet+} - Ti \rightarrow Ti - O_sH \text{ or } Ti - O_s - Ti \quad 2.7$$

Recombination of $Ti_{ds}^{3+}$ with trapped holes $Ti_{ds}$

$$Ti_{ds}^{3+} + Ti - O_sH^{\bullet+} \text{ or } Ti - O_s^{\bullet+} - Ti \rightarrow Ti_{dt}^{4+} \; Ti - O_sH \text{ or } Ti - O_s - Ti \quad 2.8$$

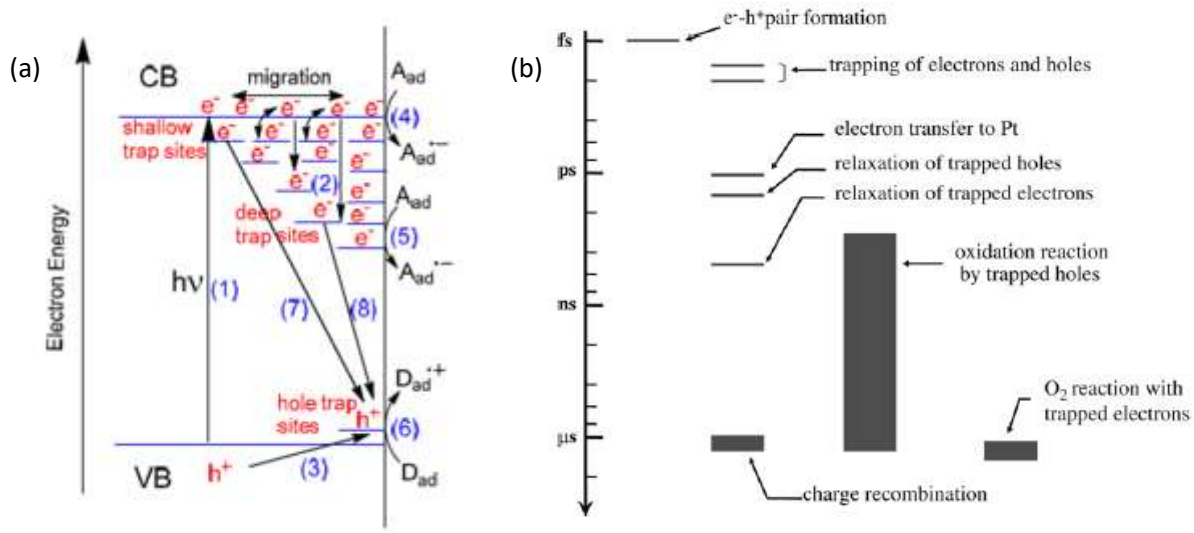



**Figure 2.6.** Schematic model of principal processes in the application of single-electron $TiO_2$ photocatalysis using anatase where CB: conduction band; VB: valence band; $A_{ad}$: adsorbed electron acceptor; $D_{ad}$: adsorbed electron donor [57], and timescales for each process Fujishima et al. [58].

Although the exciton photogeneration, transfer, recombination, and trapping mechanism have been widely reported for crystalline $TiO_2$, they also apply to A-$TiO_2$. As can be seen in **equation (2)**, the Ti-OH groups which are preponderant in A-$TiO_2$ also play a role in electron trapping mechanisms.

## 2.3. Efficient amorphous $TiO_2$ photocatalysts

A-$TiO_2$ is a typical n-type semiconductor as illustrated by the positive slope in its Mott-Schottky measurement plot in **Figure 2.7** [59]. Owing to the non-periodicity of the unit cell of A-$TiO_2$ there are various defects in its structure including point defects such as $Ti^{3+}$, and oxygen vacancies which accept photogenerated electrons thereby availing alternative channels for electron-hole pair separation [43,60,61].

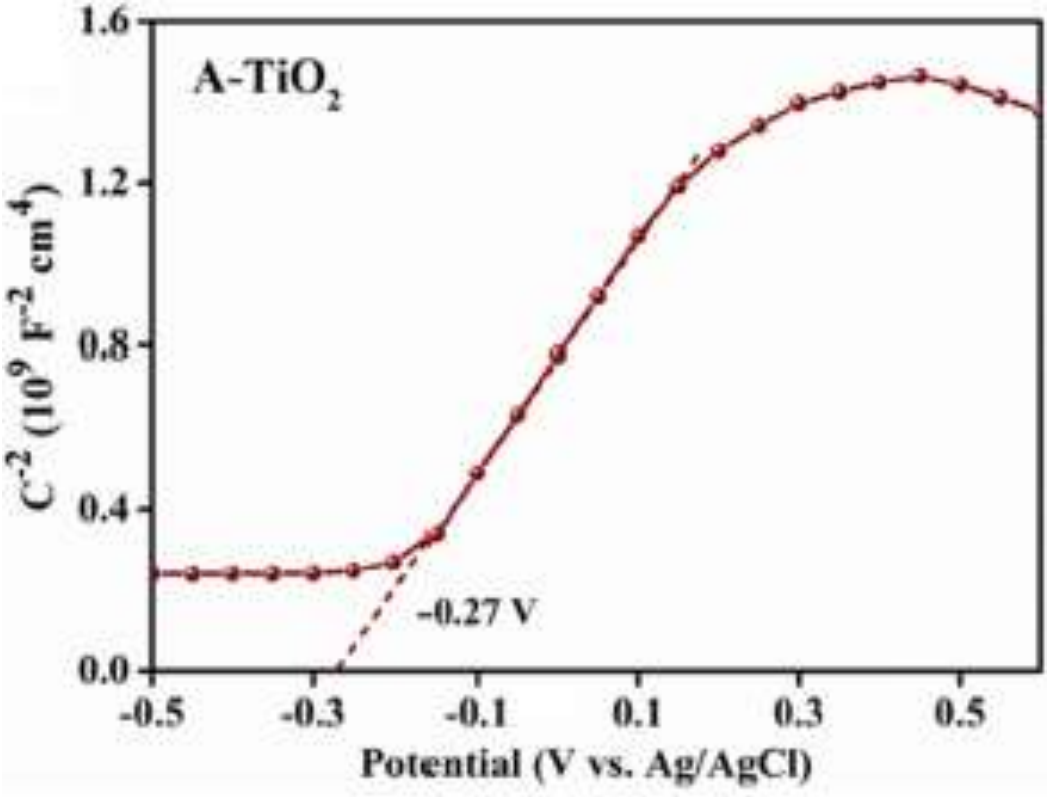



**Figure 2.7.** A typical Mott-Schottky measurement plot A-$TiO_2$ [59].

Undercoordination defects exert dominance compared to other defects within the A-$TiO_2$ structure due to the small dimensions of A-$TiO_2$ [61]. Although the action of defects in delaying electron-hole recombination is widely reported, there is still limited information on why localized charges in A-$TiO_2$ preferentially form trapping centers which consequentially avert the creation of recombination centers [62]. Apart from favoring electron-hole trapping as opposed to recombination, the ascendancy of A-$TiO_2$ as a water remediation photocatalyst in comparison to crystalline $TiO_2$ lies on the abundant surface hydroxyl groups and chemically adsorbed water suitable for adsorption [60,63,64]. Under UV irradiation A-$TiO_2$ may also exhibit better photocatalytic activity than crystalline $TiO_2$ as demonstrated by Wang et al. [63] in the photodegradation of rhodamine B.

Several techniques have been used in the fabrication of A-$TiO_2$ from various common precursors. The general synthesis strategy is that drying should be done below 80 °C to avoid crystallization. The common synthesis techniques include sol-gel and hydrolytic processes where the $TiO_2$ precursors are dispersed into water, organic solvents, or a mixture of solvents [61,63,64].

Despite its consequential ability to avert electron-hole recombination rate and high adsorption capacity, A-$TiO_2$ has one major disadvantage which is its high bandgap [60,64]. Several strategies such as doping and formation of heterojunctions with other semiconductors have been widely adopted to improve the visible light-harvesting ability and further enhance the trapping dynamics in the resulting composites. Dopants that have been used so far include sulphur [65], carbon [66,67], gold [68,69] and Pt [70] among others. Common heterostructures are between A-$TiO_2$ and semiconductors such as AgI [71], CoO [72], graphene [73], $Ag_2CO_3$ [74], g-$C_3N_4$ [75], $Bi_2WO_6$ [76] and the oxygen vacancy rich BiOBr [77–79] among others. The semiconductors coupled to A-$TiO_2$ generally have small band offsets with A-$TiO_2$ which allow the transfer of electrons from the CB of these semiconductors to that of A-$TiO_2$ and the holes in the opposite direction.

## 2.4. Amorphous $TiO_2$-BiOBr heterostructures

In this study, the binary heterostructure of interest is that involving coupling A-$TiO_2$ with BiOBr. BiOBr is a p-type visible light-responsive semiconductor characterized by a negative slope in its Mott-Schottky measurement plot (**Figure 2.8**) [59]. It has an indirect-transition band gap between 2.64 and 2.91 eV and belongs to the group of V-VI-VII ternary semiconductors [80,81]. Like all Bismuth-based compounds, it is inexpensive [82] and therefore has economic potential for large-scale applications. Typically, BiOBr has a tetragonal matlockite structure (**Figure 2.9**) where the accumulation of the layered structure is thought to be through the embedment of $[Bi_2O_2]^{2+}$ slabs in double slabs of $Br^+$ [81,83]. The related atoms and orbitals possess enough space for polarization which aids the separation of electrons and holes during photoactivation [81]. While BiOBr has a better visible light absorption ability it is seldom used in practical photocatalytic applications due to its high electron-hole pair recombination rate [84] which reduces their diffusion radius through the catalyst bulk.

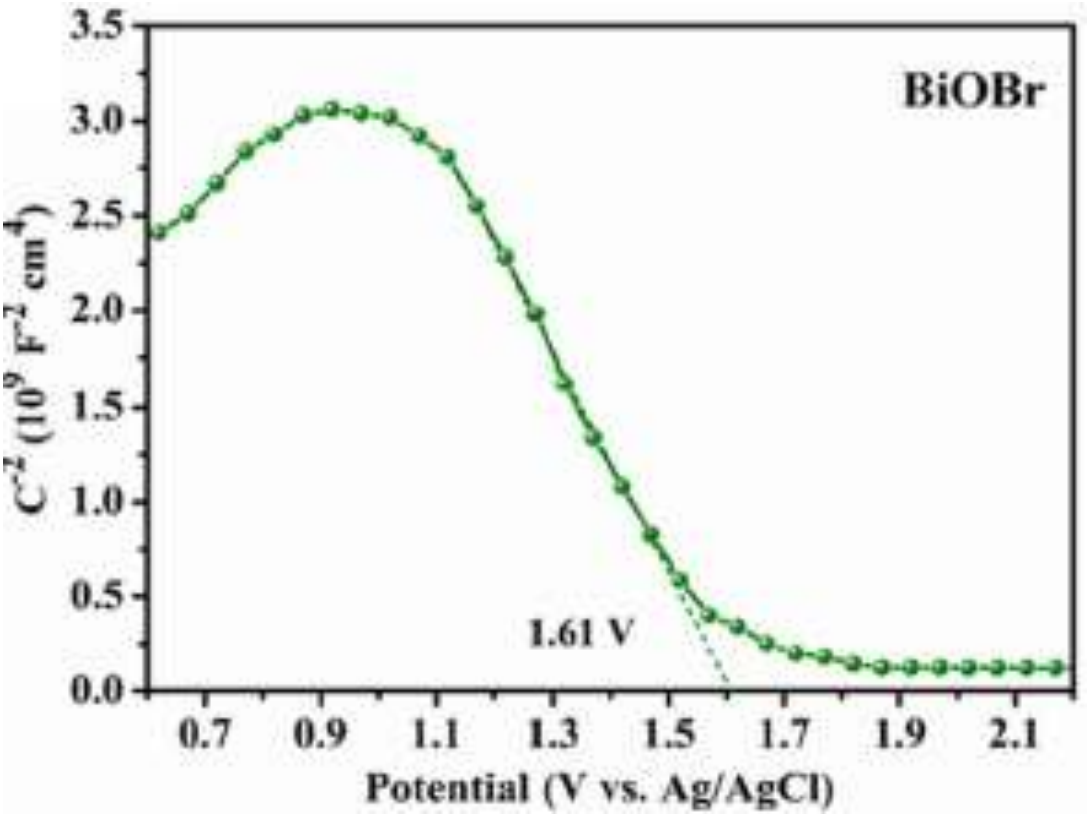



**Figure 2.8.** The Mott-Schottky measurement of BiOBr [59].

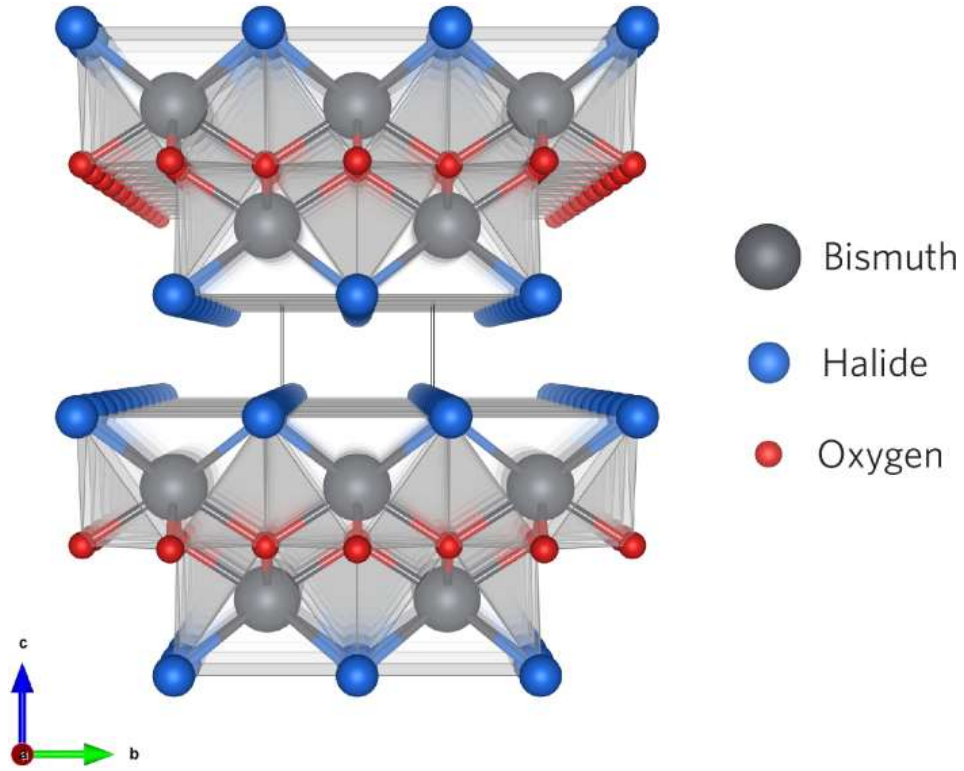



**Figure 2.9.** Crystal structure of the BiOBr systems (space group *P4/nmm*, $D_{4h}$ symmetry) with stoichiometric Br−Bi−O−Bi−Br bilayers stacked along the c axis [83].

Coupling A-$TiO_2$ and BiOBr results in a useful p-n heterojunction which results in a visible light active binary hybrid with a lower exciton lifetime and a bandgap narrower than that of A-$TiO_2$ [85]. Over the years, a limited number of reports on the fabrication of A-$TiO_2$-BiOBr composites for photocatalytic water remediation have been presented [77–79]. Deng et al. [79] and Wei et al. [77] used similar solvothermal processes while Wang et al. [78] used an in situ direct growth process under microwave irradiation in fabricating A-$TiO_2$-BiOBr photocatalysts.

In the solvothermal process by Deng et al. [79], $Bi(NO_3)_3 \cdot 5H_2O$, cetyltrimethylammonium bromide (CTAB), and tetrabutyl titanate (TBOT) were dissolved sequentially in ethylene glycol under stirring before heating under autogenous conditions at 160 °C in an autoclave. After that, the mixture was cooled and then washed in ethanol and distilled water before air-drying at 80 °C. The hybrid structure with a unit atomic ratio of TBOT to bismuth nitrate had the best activity in the removal of methyl orange. In the report by Wei et al. [77], a similar process was used but with ethanol as a solvent under a solvothermal temperature of 150 °C. The composite with a Ti/Bi molar ratio of 10 exhibited the best photocatalytic activity in the removal of rhodamine B.

In the in situ direct growth process (**Figure 2.10**) presented by Wang et al. [78], $Bi(NO_3)_3 \cdot 5H_2O$ and NaBr were dissolved sequentially in water and transferred into an autoclave and heated at 160 ºC. The resulting suspension was cooled and then washed with deionized water and finally air-dried at 60 °C to form BiOBr. A-$TiO_2$ was formed by stirring a mixture of metatitanic acid ($H_2TiO_3$), purified water, $H_2O_2$, and $NH_3 \cdot H_2O$ in an ice-water bath. The mixture was then mixed with a dispersion of BiOBr powder and microwave-irradiated. The A-$TiO_2$-BiOBr heterostructures obtained vacuum filtration and dried in an oven at 60 °C. It was demonstrated through PXRD analysis that the coupling between A-$TiO_2$ and BiOBr occurred through the (001) faces of BiOBr and the heterostructures with 15% A-$TiO_2$ had the highest photocatalytic activity towards methyl orange (MO) through a mechanism shown in **Figure 2.10**.

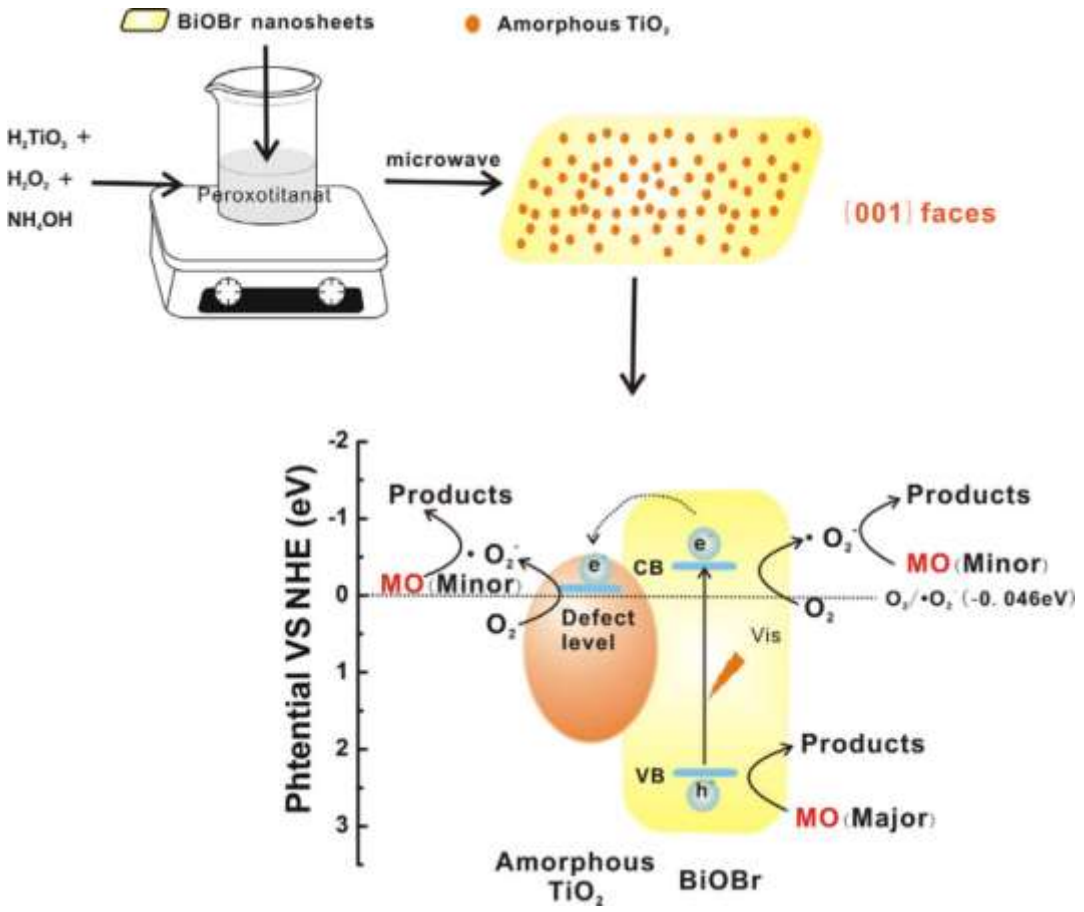



**Figure 2.10.** The formation and photocatalytic mechanism scheme of the amorphous $TiO_2$/BiOBr composite [78].

## 2.5. General chemistry of clay as support of $TiO_2$ photocatalysts

Clay is a naturally occurring material composed of fine-grained minerals whose plasticity index is equal to or higher than half its liquid limit so that it is plastic or highly plastic at water contents that are between the liquid and plastic limits [86]. The plasticity index is the difference in the amount of water contained in clay between the liquid and plastic limits [87]. The liquid limit is at comparatively high water content such that the clay is altered from its liquid to plastic state and the plastic limit is at comparatively low water content such that the clay is altered from the plastic to solid state [87]. Important characteristics of clays are related to their applications in the immobilization of metal (oxide) catalysts and include large specific surface area, viscosity, dry and fired strength, plasticity, favorable absorption, and high adsorption capacities [88]. Other attributes of clay include their small grain size, large cation exchange capacity, large chemically active surface area, and capability of interacting with both inorganic and organic liquids [89].

Clays are described as 1:1 phyllosilicates if they are composed of one tetrahedral and one octahedral sheet per clay layer or 2:1 phyllosilicates if they are composed of two tetrahedral sheets sandwiching one octahedral sheet per clay layer [90]. Among 2:1 phyllosilicates, smectites such as bentonite and vermiculites are known for their expansibility [91,92]. The generalized structures of 1:1 and 2:1 clays are presented in **Figure 2.11** and a detailed classification of clays, with common examples, is shown in **Figure 2.12**. However, rectorite (allevardite) occurs naturally as an interstratified composite consisting of two 2:1 clays i.e. a dioctahedral mica layer and a dioctahedral beidellite smectite layer in a 1:1 ratio [93,94].

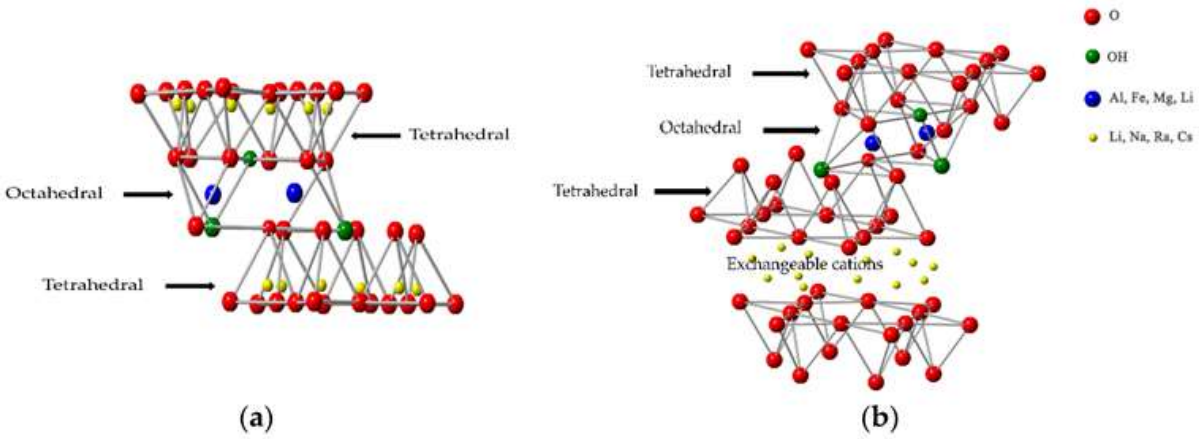



**Figure 2.11.** The arrangement of tetrahedral (T) and octahedral (O) layers in 1:1 and 2:1 clays [95].

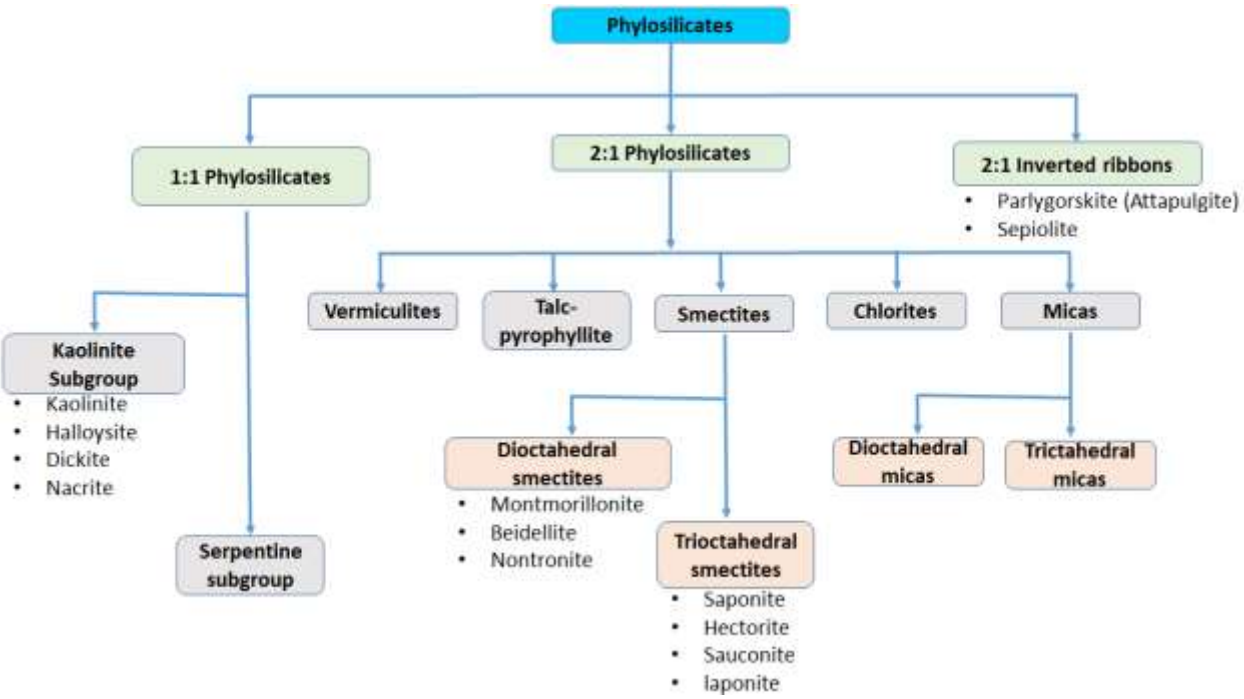



**Figure 2.12.** Classification of cationic clays (phyllosilicates), adapted from Bailey et al. [96].

To fabricate $TiO_2$/clay heterostructures, an exchange process between $TiO_2$ powder, $TiO_2$ suspension, $TiO_2$ precursors or $TiO_2$ sols, and exchangeable cations in the clay interlayer spacing has to occur. The incoming $TiO_2$ architectures induce permanent porosity in the clay and the interaction between the $TiO_2$ architectures and the clay is through the formation of the Ti-O-Si bonds seen in the infrared (IR) spectrum at around 957 $cm^{-1}$ [13]. For 1:1 clays an Al-O-Ti peak at 530.05 eV in an X-ray photoelectron spectrum (XPS) also confirms the $TiO_2$/clay interaction [97]. The overall effect Ti-O-Si and Al-O-Ti bonds in $TiO_2$/clay heterostructures is the induction of favorable physicochemical and optoelectrical parameters into $TiO_2$ such as suppressed sintering, suppressed the anatase to rutile transformation [98–100], narrowed bandgap [13,101] resulting in stable composites with high porosity, higher specific surface area, and improved catalytic activity.

Since the photocatalytic abatement of organic pollutants on $TiO_2$/clay photocatalysts is through the "adsorb-degrade-release" mechanism, therefore higher porosity is principal as it allows easy shuttle of the pollutants and degradation products within the photocatalyst porous framework. Moreover, a higher surface area associated with $TiO_2$/clay photocatalysts allows a large number of pollutant molecules to come into contact with the active sites and also allows the light used to reach wider areas to activate the photogeneration of the electrons and holes within the photoactive $TiO_2$ centers.

Quantifying the Si-O-H/Si-O-Ti ratio gives a general idea of the interaction of $TiO_2$ and clay in binary $TiO_2$/clay heterostructures. The extent of reduction in the Si-O-H/Si-O-Ti ratio as $TiO_2$ gets intercalated into clay is associated with a high degree of chemical interaction between the $TiO_2$ and the aluminosilicate platelets which is evidence of chemical bonding of $TiO_2$ on the clay surfaces [102].

## 2.6. Processes used to synthesize $TiO_2$/clay composites

Several processes are used to fabricate binary, ternary, and quaternary $TiO_2$/clay-based photocatalysts. The chosen fabrication process is dependent upon the properties that are required in the resulting powders.

Generally, the synthetic methods used in the fabrication of binary $TiO_2$/clay nanocomposites can be classified into two broad classes, viz: simple dry diffusion (grinding) techniques between clays and $TiO_2$ powder and wet chemical or pillaring processes. With ternary and quaternary composites, single and multistep processes are normally used to improve or induce specific properties of interest in the corresponding $TiO_2$/clay binary composites.

In diffusion processes, clay and $TiO_2$ powders are mixed through grinding for homogenization [98], and sometimes a small amount of solvent may be added to improve the distribution of the $TiO_2$/clay powders before high-temperature calcination [103]. However, diffusion methods are seldom used due to the poor interaction between $TiO_2$ NPs and the clay surfaces in the composites. This is evidenced by the limited number of Si-O-Ti bonds formed, i.e. the high Si-O-H/Si-O-Ti ratio which induces insignificant influence on the properties of $TiO_2$ [98].

Wet chemical or pillaring processes are the most commonly used synthetic methods in the fabrication of $TiO_2$/clay composites. In general, wet chemical processes are based on the substitution of exchangeable ions between the aluminosilicate layers of clay by polymerized hydroxyl titanium ions prepared by mixing a $TiO_2$ precursor and a solvent of interest which are then calcined to crystallize the $TiO_2$ [104]. Sometimes the $TiO_2$ precursors are intercalated directly into clay in their pure form without treatment in any solvent [105]. In the case of amorphous $TiO_2$/clay composites, the calcination step is omitted to maintain the disorder and the non-periodicity of the unit cells of $TiO_2$.

We attempted to describe wet chemical processes using representative examples in a generalized form where necessary. In a generic sense, wet chemical processes can be broadly divided into sol-gel processes, heterocoagulation processes, hydrothermal processes, solvothermal processes, and impregnation processes. The most commonly used $TiO_2$ precursors under such processes include tetrabutyl titanate, titanium isopropoxide, titanium chloride, titanium sulfate, titanium ethoxide, titanium oxychloride, and titanium (IV) bis(ammonium lactato) dihydroxide.

In a typical sol-gel process, a $TiO_2$ sol is prepared by dispersing $TiO_2$ precursors in aqueous systems or alcohol-water systems to form a white suspension which is then hydrolyzed to form a clear solution before intercalation into a clay dispersion [106]. The $TiO_2$ sol and clay mixture is then subjected to thermal treatment at temperatures below 200 ºC, washed, dried and calcined. Furnace calcination has been the main method of thermal treatment used to crystallize $TiO_2$. However, microwave calcination is now a common thermal treatment strategy [107,108]. A microwave-assisted sol-gel technique where a $TiO_2$ sol is intercalated into clay under microwave irradiation followed by furnace calcination was reported by Sun et al. [109].

For hydrothermal processes, $TiO_2$ (precursor) and clay are mixed with water as the main solvent and then treated under autogenous pressure in an autoclave at elevated temperatures in the 80-200 °C range before washing, drying, and calcination [106,110]. Recent advances in hydrothermal processes have led to its modification by incorporating microwave radiation into the systems used during synthesis [111,112]. However, there is another technique, the

solvothermal process, akin to hydrothermal treatment processes where different solvents such as alcohols which may be mixed with some water are used to disperse the clay and $TiO_2$ precursors before thermal treatment under autogenous pressure in an autoclave [113,114].

Generally, in impregnation processes, clay powder is dispersed into $TiO_2$ sols or solutions and stirred under mild temperatures [115] or room temperature [102], washed, dried, and then calcined. Sometimes clay powder can be directly dispersed into a $TiO_2$ precursor such as titanium (IV) isopropoxide [105] or in water dispersed $TiO_2$ powder under mild heating [116]. While impregnation may be regarded as a simplistic process, there is a report on the use of supercritical ethanol to impregnate $TiO_2$ precursors into the clay before calcination and this makes the technique somehow complicated and expensive [117]. It is noteworthy that the heterocoagulation process is akin to the sol-gel and impregnation processes [118] except that in a heterocoagulation process $TiO_2$ is first precipitated from the $TiO_2$ sol to form aggregates under adjusted pH before intercalation into a clay suspension [119,120].

The fabrication of ternary and quaternary $TiO_2$/clay materials is necessary to improve specific properties of the binary composites such as their visible, surface area, and porosity among others for improved photocatalytic activity. There are three main techniques used to fabricate ternary $TiO_2$/clay composites which are described by Carriazo et al. [121] with iron-loaded $TiO_2$-Montmorillonite as a model composite. In the first method, a single pillaring solution containing precursors of $TiO_2$ and the other active species is intercalated into a clay dispersion to fabricate doped $TiO_2$/clay composites. With the other two methods, $TiO_2$/clay powders are first fabricated and then the solution containing a precursor of the third component is then loaded into $TiO_2$/clay composites. The solution is normally loaded either through direct impregnation into $TiO_2$/clay powders or using a cationic exchange process where the precursor solution is mixed with a $TiO_2$/clay dispersion. Some plasmonic metals like Au can be impregnated into $TiO_2$/clay composites through a deposition-precipitation process where the Au is precipitated through heating a $TiO_2$/clay in an Au precursor under controlled pH and temperature [122]. With plasmonic metal-based $TiO_2$/clay composites, it is sometimes necessary to reduce the plasmonic metals either through photoreduction [123–125] or chemical reduction [126,127] to get zerovalent plasmonic metal NPs in the composite. Sometimes the clay is treated with the other semiconductor before intercalating $TiO_2$ [128].

Quarternary $TiO_2$/clay heterostructures are seldom synthesized for use in photocatalytic applications. However, ternary $TiO_2$/clay composites are synthesized using two main methods. The most commonly used technique is preparing a single solution with a $TiO_2$ precursor and precursors of the other two components resulting in co-doped $TiO_2$/clay composites. The co-

dopants may be metal-nonmetal pairs [129–131] or non-metal pairs [132,133]. The second synthesis technique involves quaternizing ternary $TiO_2$/clay composites accordingly with a suitable precursor of the fourth component [134,135].

## 2.7. Review on $TiO_2$/Bentonite composites for water remediation

Bt is widely considered as impure montmorillonite (Mt) with smaller percentages of quartz, cristobalite, feldspar, pyrite, carbonates, chlorite, kaolinite, mica, illite [136], calcite, and muscovite [137]. Mt is a cationic, dioctahedral smectite clay with an idealized formula $M^{n+}_{x/n} \cdot yH_2O[Al_{4.0-x},Mg_x]Si_{8.0}O_{20}(OH)_4$, where $M^{n+}$ is the exchangeable metallic species in each formula and the cations enclosed in brackets are occupants of the octahedral sites and the cations in parentheses are the occupants of the tetrahedral sites [138]. Layers of montmorillonite and other smectite clay minerals are negatively charged because of the positive charge deficiencies in the 0.4-1.2 e range per $Si_8O_{20}$ unit as a result of the isomorphous substitution of tetrahedral $Si^{4+}$ by octahedral $Al^{3+}$ which allow small hydrated cations with a low charge to be intercalated between the silicate layers to balance these deficiencies [139]. There are other reports on the isomorphous substitution of $Al^{3+}$ in octahedral layers by $Mg^{2+}$ [140]. The small monovalent and divalent exchangeable cations constituting $Na^+$, $K^+$, $Ca^{2+,}$ and $Mg^{2+}$ within the interlayer spacing of montmorillonite imparts its cation exchange capacity (CEC). The CEC is the total capacity of the clay to electrostatically attract the exchangeable cations into its negatively charged surfaces [137]. The generalized clay-stacking pattern of the octahedral and tetrahedral structural layers of Mt is shown in **Figure 2.13.**

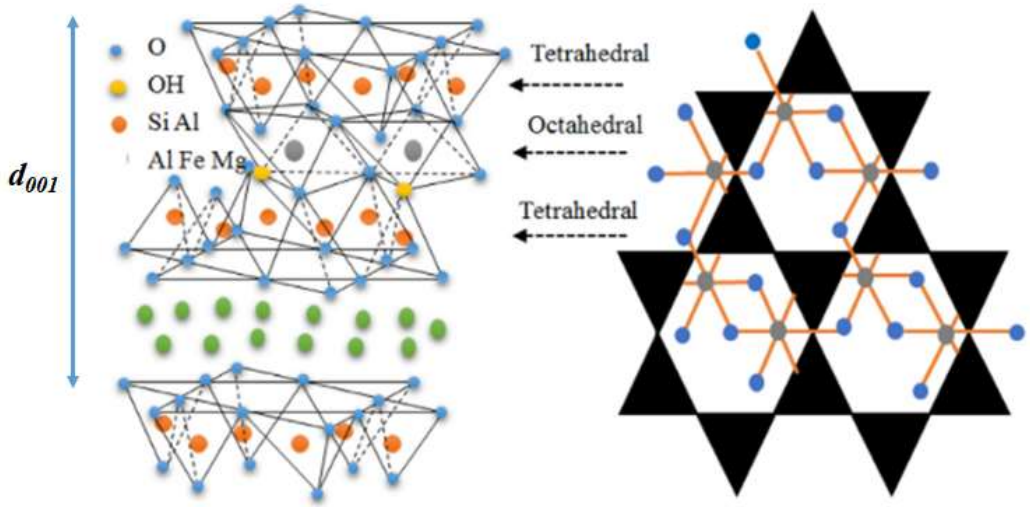



**Figure 2.13.** Structure showing the tetrahedral and octahedral sheets of Mt and the top view of Mt layers [141].

Several investigations have been conducted to quantify Mt in various Bt clays [136]. It was generalized that any clayey material with 70-95% Mt is considered bentonite [142]. Mt and Bt/$TiO_2$-based account for a majority of $TiO_2$/clay-based photocatalysts studied and their effectiveness in water remediation is highlighted in most cases.

As already stated, Bt is among the most widely used clays in the fabrication of $TiO_2$/clay-based photocatalysts. It has strong relevance in the South African perspective as large Bt deposits are located at the cretaceous beds of the Southern Cape, South of the Langeberg in the district of Heidelberg, South Africa, and ECCA holdings is the main supplier of Bt in South Africa. Bt is among the cheapest catalyst carriers found in South Africa both in terms of procurement price and in the sense that it can be applied directly in catalytic fabrication without processing. The different synthetic methods used to fabricate binary, ternary, and quaternary $TiO_2$/Bt-based composites are discussed in this section. An effort has been made to correlate the properties induced by each method in the resulting composites and their ability to photodegrade multifarious organic water pollutants.

The sol-gel process is among the methods used in the fabrication of binary $TiO_2$/Bt composites for water treatment. Ali and Hosein [143] used the sol-gel process to load onto HCl/$NH_3$ pre-treated Bt. The composites obtained from their study were tested on the removal of multifarious organic pollutants in Kermanshah Refinery plant [143]. Through this study, which is among the earliest ever presented on real-life matrices, the binary $TiO_2$/Bt composite removed all the organic pollutants in the miscellaneous refinery wastewater with initial chemical oxygen demand (COD) of 700 ppm at pH 4.5 where the $TiO_2$/Bt dosage was 1 g/L.

However, it has been observed that microwave-assisted methods reign supreme in inducing high pore volume, large BET surface area, and single-phase anatase $TiO_2$ within a short time [116,144]. It is for this reason that Mishra et al. [144] immobilized anatase $TiO_2$ NPs of sizes between 10-25 nm on Bt within 10 min through the intercalation of titanium (IV) butoxide into a Bt suspension, followed by hydrolysis and the subsequent microwave treatment at 180 °C. Optimum $TiO_2$ loading for the highest photocatalytic activity was 50 wt% owing to its relatively large number of active sites exposed, high BET surface area, and the high pore volume of the nanocomposite. In a separate but slightly similar study, Laysandra et al. [116] impregnated up to 20% water dispersed Degussa $TiO_2$ into $H_2O_2$ purified Bt and heated the resulting suspension for an hour at 100 °C followed by 10 min of microwave irradiation before drying. The $TiO_2$/Bt composite constituted of anatase $TiO_2$ NPs and exhibited effective methylene blue and rhodamine B decoloration under UV irradiation and the order of

effectiveness increased with increasing $TiO_2$ content due to the increase of pore volume, BET surface, and the number of active sites.

Fe-based $TiO_2$/Bt composites are the most studied ternary and quaternary $TiO_2$/Bt composites. Carriazo et al. [121] prepared Fe-Ti-Bt nanocomposites using three methods, viz: intercalation of a bimetallic $Fe^{3+}/Ti^{4+}$ pillaring solution into bentonite to form Fe-Ti-PILB, incorporation of $Fe^{3+}$ by cationic exchange species into Ti-PILB to form Fe-Ti-CE, and wet impregnation of $Fe^{3+}$ ions into Ti-PILB to form Fe-Ti-IMP. The phenol photodegradation efficiency increased in the order Fe-Ti-IMP< Fe-Ti-CE< Ti-PILB< Fe-Ti-PILB respectively.

Recently Molina et al. [145] attempted to improve the porosity of $Fe_2O_3$-$TiO_2$/Bt heterostructures through immobilizing $TiO_2$ NPs into a $CTA^+$/Bentonite organoclay followed by calcination of the organo-inorganic clay to remove the organic structural regulators. Iron (III) ($FeCl_3 \cdot 6H_2O$) was subsequently loaded through wet impregnation. The fabricated $Fe_2O_3$-$TiO_2$/Bt nanocomposite had a mesoporous, disordered layered structure with improved catalytic removal of two pharmaceutical drugs: acetaminophen and antipyrine under the Fenton and photo-Fenton processes.

For a synergic effect of better visible light activation and extension of the exciton lifetime of $TiO_2$/Bt photocatalysts, Cao et al. [129] loaded N/Fe co-modified $TiO_2$ nanoparticles on Bt through the sol-gel method. The Bt-N/Fe-$TiO_2$ composite had superior absorption in the UV-visible region due to the induced $Fe^{3+}$ and N 2p intraband energy states which provide an alternative low energy photoactivation mechanism leading to improved removal of methylene blue at room temperature under UV and visible light irradiation.

Several magnetically recyclable iron-containing $TiO_2$/Bt nanocomposites have been fabricated using a variety of synthetic methods. A sol-gel technique was used to load $TiO_2$ NPs onto $Fe_3O_4$-modified Bt which had been prepared through a co-precipitation technique under a nitrogen atmosphere [128]. Upon thermally treating the colloidal suspension in a muffle furnace at 773 K the $TiO_2$ and $Fe_3O_4$ NPs were perfectly immobilized on the Bt nanoneedles. This magnetically recoverable composite removed 90% of methylene blue under UV light with a 20% mass loss incurred after six cycles. Another magnetically recoverable, but visible light active $Fe_2O_3$-Bt-$TiO_2$ heterostructured photocatalyst was synthesized by Cao et al. [146] using a facile sol-gel method illustrated in **Figure 2.14**. The $Fe_2O_3$-Bt-$TiO_2$ composite efficiently degraded MB and maintained high photocatalytic activity after being regenerated several times.

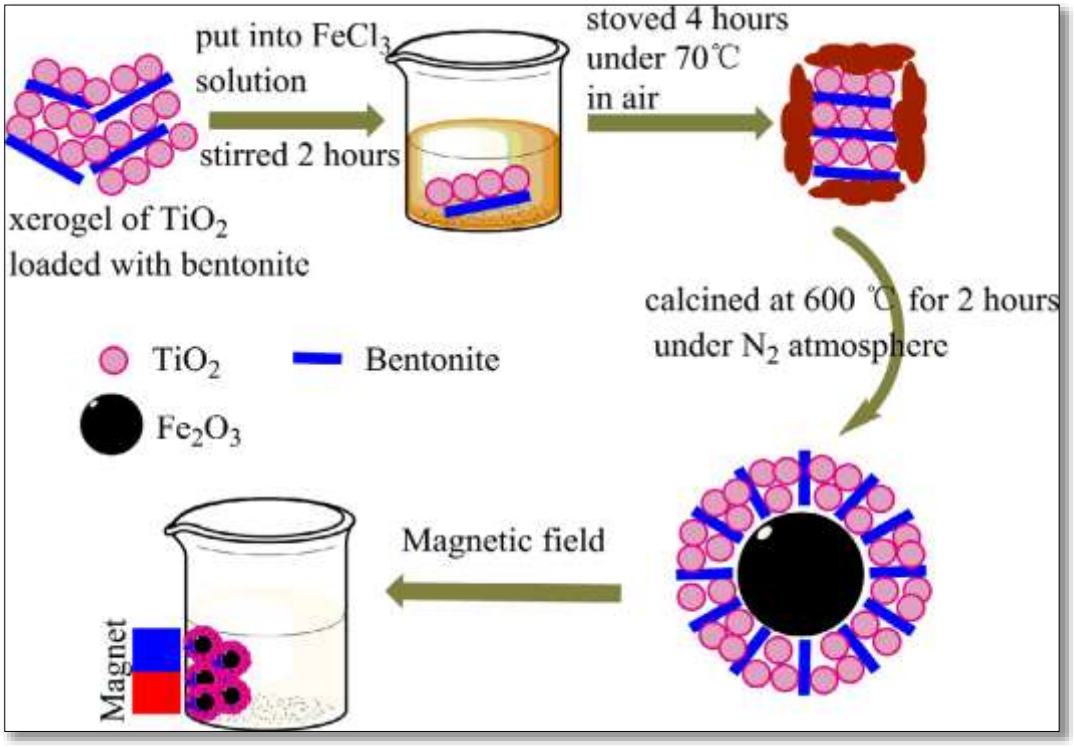



**Figure 2.14.** Synthesis scheme for $Fe_2O_3$-Bt-$TiO_2$ [146].

Elsewhere, Cao et al. [147] fabricated a mesoporous visible light active magnetic heterostructure, CST/γ-$Fe_2O_3$-Bt, by loading sulfur-doped $TiO_2$ hollow spheres into γ-$Fe_3O_4$-Bt which had been modified by composite surfactant mixture of CTAB and sodium dodecyl sulfate. The multifunctional catalyst had good adsorption and photodegradation performance against bisphenol A, with an adsorption capacity of 77.36 mg/g and the ability to maintain a 91% bisphenol A removal efficiency after 5 catalytic cycles.

There have been several reports on the different synthesis methods of Cu, Au, and Ag-based $TiO_2$/Bt plasmonic nanocomposites with low $TiO_2$ excitation energy. Recently, Ahmad and Yasin [148] fabricated a Cu-$TiO_2$/Bt composite using a thermal decomposition and reduction method. They mixed copper (II) nitrate and a $TiO_2$ sol (titanium butoxide + butanol) to a single pillaring solution which was dispersed in a bentonite dispersion followed by washing in ethanol, drying, and calcination. The ternary composite exhibited excellent photocatalytic abatement of deltamethrin insecticide during sunlight exposure. Li et al. [122] used a deposition-precipitation method to fabricate Au-$TiO_2$/Bt photocatalysts. In the deposition-precipitation process, $TiO_2$/Bt was dispersed in a $HAuCl_4$ solution heating at 80 °C and pH 8. After washing and drying they calcined the materials in the 300-600°C range and the optimum calcination temperature is 400 °C for effective photocatalytic removal of sulforhodamine B.

Bang et al. [149] fabricated Ag–$TiO_2$/Bt using the sol-gel process where an Ag-$TiO_2$ composite sol was deposited into a Bt suspension embedding the $TiO_2$ and Ag NPs onto the clay layers. The superiority of these plasmonic photocatalysts is attributed to the enhanced charge separation and the induced localized surface plasmonic resonance effect.

According to Mishra et al. [150], the influence of different plasmonic metals in enhancing the activity of $TiO_2$/Bt nanocomposites is reliant on the metal used. They correlated the effects of impregnating 1% by wt of Ag, Au, Pd into $TiO_2$/Bt to the photocatalytic activity of the resulting M–$TiO_2$/Bt nanocomposites. The incorporation of these plasmonic metals slightly increased the BET surface area and induced surface plasmonic peaks in UV-visible DRS spectra (peak max at 502, 503, and 541 nm for Pd, Ag, and Au) of the composites. Consequently, there was an increase in the exciton lifetime between 2.50 and 2.60 ns due to the action of the plasmonic metal centers as electron sinks which favored the generation of superoxide and hydroxyl radicals thereby aiding in the photodegradation of chlorobenzene and benzaldehyde. The highest photocatalytic activity was afforded by the Ag-$TiO_2$/Bt nanocomposite which had a rate constant of 0.055 and 0.0178 $min^{-1}$ for chlorobenzene and 0.027 and 0.004 $min^{-1}$ for benzaldehyde degradation under UV and visible light respectively.

Recently, graphitic carbon nitride (g-$C_3N_4$) and graphene oxide (GO) have been used to fabricate excellent visible light active $TiO_2$/Bt ternary composites due to effective charge carrier separation and visible light-harvesting ability induced by the heterojunction between the $TiO_2$ NPs and these carbonaceous photosensitizers [151–153]. Mishra et al. [151] loaded 10-50 wt% of g–$C_3N_4$ prepared from urea into a $TiO_2$/Bt nanocomposite through wet impregnation at room temperature to form porous heterostructures. The 40% g-$C_3N_4$/$TiO_2$/Bt composite (40 CTB) removed 90% of a reactive brilliant red dye (RBR–X3BS) in 100 min under visible light. This was due in part to the inhibition of charge carrier recombination through a simple mechanism that involved electron transfer from g-$C_3N_4$ to $TiO_2$ narrowing the bandgap below 2.80 eV and the strong electrostatic interaction between the long, thin, g–$C_3N_4$ nanosheets and Bt clay. The HRTEM image in **Figure 2.15** shows the lattice fringes with a fringe spacing of 0.32 nm for $TiO_2$ which is ascribed to an inter-planar spacing of (110) rutile $TiO_2$. It has also been observed that g-$C_3N_4$ precursors used in the sensitization of $TiO_2$/Bt induce different morphologies g-$C_3N_4$-$TiO_2$/Bt heterostructures which direct their activity. According to Mishra et al. [152] among urea, thiourea, and their 1:1 w/w mixture, urea gave thin and long g-$C_3N_4$ nanosheets that interacted intimately with $TiO_2$/Bt resulting in a superior catalyst.

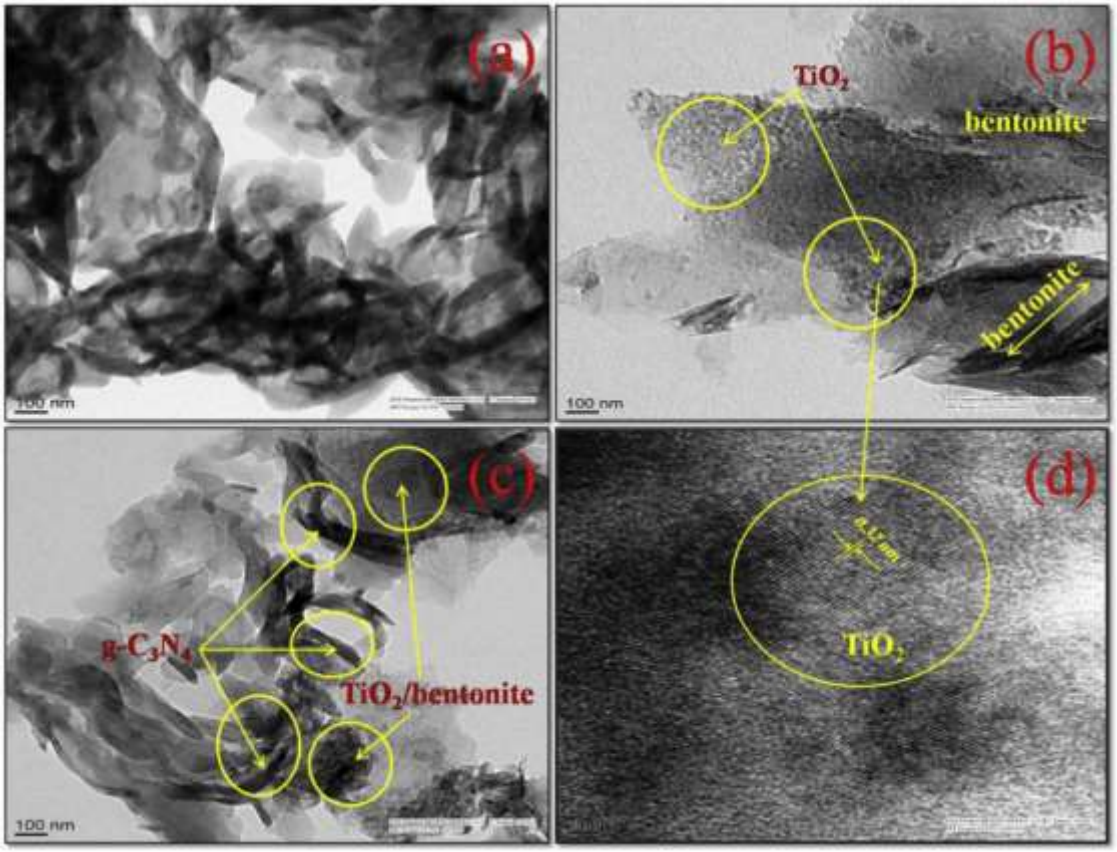



**Figure 2.15.** (a) HRTEM image of (b) g-$C_3N_4$, (c) $TiO_2$/Bt nanocomposite, (d) g-$C_3N_4$-$TiO_2$/Bt nanocomposite (40 CTB) and (d) high resolution image of $TiO_2$ showing lattice fringes [151].

In addition to enhancing the visible light absorption, charge separation, and other optoelectronic properties when incorporated into $TiO_2$/Bt, GO also improve the recoverability of the composites [153]. Liu et al. [153] mixed 5-15% w/w GO sponge, which had been prepared by the Hummers' method with $TiO_2$/Bt powder through in situ hydrothermal methods at 175 °C for 10 h. The GO-$TiO_2$/Bt sponge was conveniently obtained after freeze-drying and the 10% w/w GO sample effectively removed MB within 80 min. This was attributed to the excellent charge separation and visible light absorption capacity afforded by the material due to the Ti-O-C bond in the $TiO_2$-GO interface extending its absorption edge to 467 nm.

**Table 2.2** shows a comparative summary of the photodegradation of organic pollutants using $TiO_2$/Bt composites. Reaction parameters such as catalyst dosage, initial concentration of pollutant, light source, conversion efficiency, rate constant, and the reaction time are shown for each photocatalyst. Of great importance in the review of the use of $TiO_2$/Bt composites in water remediation, is that there are no reports on the fabrication and use of A-$TiO_2$-BiOBr-Bt heterostructures. This is simply because studies on such materials have not yet been undertaken.

**Table 2.2. $TiO_2$/Bt composites commonly applied in the degradation of various organic water pollutants.**

| Clay composites | Organic contaminant | Catalyst dosage (mg/mL) | Initial contaminant level | Light source | Conversion efficiency (%) | Rate constant ($min^{-1}$) | Reaction time (min) | Ref |
|---|---|---|---|---|---|---|---|---|
| $TiO_2$/Bt | Naphthol blue-black | 16 | 5 mg/L | A 6W UV lamp (λ=365 nm). | 99.83 (UV)<br>99.83 (Vis) | - | 120 (UV)<br>90 (Vis) | [154] |
| $TiO_2$/Bt | Methylene Blue | 0.2 | 0.019 mM | A 64 W mercury UV lamp. | 98 | - | 20 | [144] |
| Fe-$TiO_2$-Bt | Phenol | 5 | $5\times10^{-4}$ M | A UV lamp (P=0.4 W, λ=330-390 nm). | *ca*. 90 | - | 240 | [121] |
| $Fe_2O_3$-$TiO_2$/Bt | Acetaminophen | 0.25 | 5 mg/L | A 765–250 W/$m^2$ Xe lamp with I= 600 W/$m^2$. | 100 | - | 240 | [145] |
| $Fe_2O_3$-$TiO_2$/Bt | Antipyrine | 0.25 | 5 mg/L | A 765–250 W/$m^2$ Xe lamp with I= 600 W/$m^2$. | 100 | - | 240 | [145] |
| Bt-N/Fe-$TiO_2$ | Methylene Blue | 1 | 10 mgL | A 250 W high-pressure Hg lamp and xenon lamp equipped with a UV cut-off filter. | 100 | - | 50 | [129] |
| $TiO_2$-$Fe_3O_4$/Bt | Methylene Blue | 0.3 | 30 mg/L | A 350 W xenon UV lamp equipped with a 288 K constant temperature circulator. | >90 | - | 60 | [128] |
| $Fe_2O_3$-Bt-$TiO_2$ | Methylene Blue | 1 | 10 mg/L | A 500 W xenon lamp equipped with a UV cut-off filter as a source of visible light. | 100 | - | 120 | [146] |
| CST/γ-$Fe_2O_3$-Bt | Bisphenol A | 0.67 | 20 mg/L | Visible light. | - | 0.00104 | 300 | [147] |
| Ag-$TiO_2$/Bt | Phenol | 1.7 | 100 mg/L | Sunlight or solar simulator (Newport, USA). | 98.94 | - | 90 | [149] |
| g-$C_3N_4$-$TiO_2$/Bt | RBR–X3BS | 1 | 40 ppm | A 65 W CFL lamp. | 90 | - | 100 | [151] |
| g-$C_3N_4$-$TiO_2$/Bt | RBR–X3BS | 1 | 40 ppm | A 65 W CFL lamp. | 85 | 0.008 | 100 | [152] |
| GO-$TiO_2$/Bt | Methylene Blue | 0.05 | 100 mg/L, | A Xe lamp (λ=2020-1050 nm, I=86 mW/$cm^2$). | 80 | - | 90 | [153] |
| A-$TiO_2$-BiOBr-Bt | Phenol | 1.5 | 20 ppm | A 300 W visible light lamp in a Lelesil photoreactor | 100 | - | 60 | This study |

## 2.8. Amorphous $TiO_2$-BiOBr/clay photocatalysts

To our knowledge, there is one report on the synthesis of A-$TiO_2$-BiOBr-clay photocatalysts and it was reported by Hu et al. [59]. They fabricated a novel visible light photoactive and oxygen vacancy-rich A-$TiO_2$-BiOBr-Sepiolite through a one-pot solvothermal method as shown in **Figure 2.16**. The mass ratio of BiOBr:$TiO_2$:sepiolite was fixed at 3:1:4. Ethylene glycol acted as a reducing agent and induce oxygen vacancies on the surface BiOBr through the removal of surface oxygen atoms. The oxygen vacancies and the ternary heterojunction between BiOBr, $TiO_2$, and Sepiolite resulted in the narrowing of the bandgap to 2.53 eV.

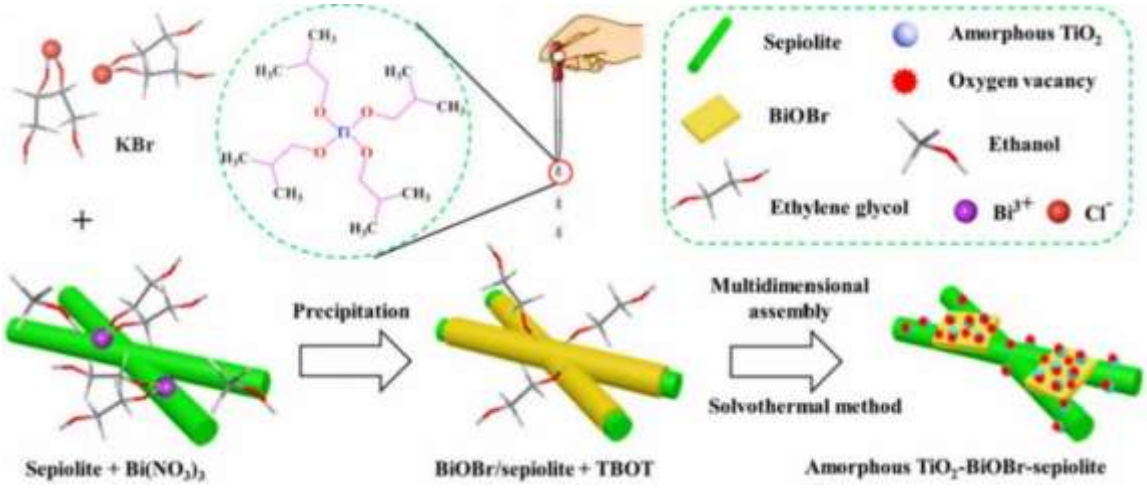



**Figure 2.16.** The synthesis of the oxygen vacancy-rich amorphous $TiO_2$-BiOBr-sepiolite catalysts [59].

During photocatalysis, electrons are injected from the conduction band of BiOBr to the conduction band of $TiO_2$ such that the $TiO_2$/oxytetracycline solution interface becomes concentrated with electrons allowing easy reduction of molecular oxygen into the active superoxide radical (**Figure 2.17**). The holes are injected from the valence band of A-$TiO_2$ to the valence band of BiOBr such that the BiOBr/oxytetracycline interface becomes a site of direct oxidation of the oxytetracycline molecules from the photogenerated hole. The sepiolite provided high surface area and favorable adsorption capacity such that the removal efficiency of oxytetracycline was 85% after four consecutive cycles within 2 h irradiation time.

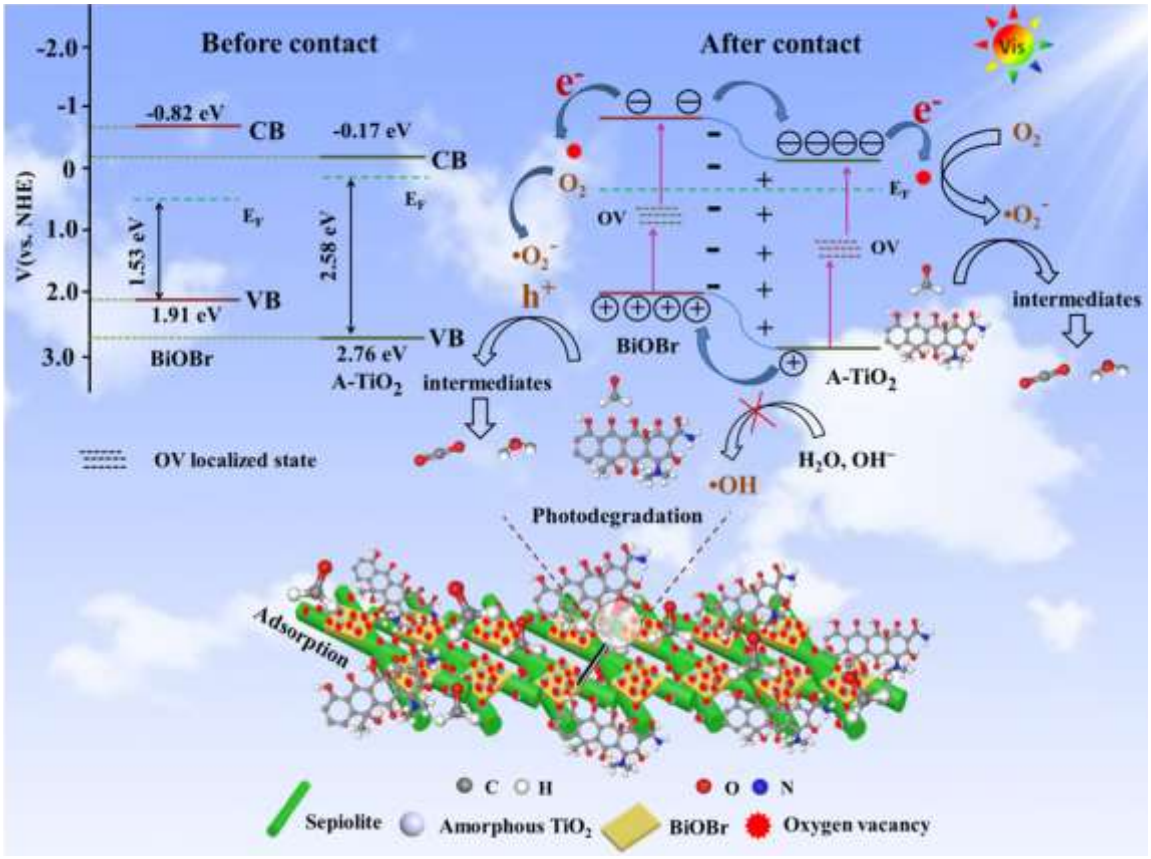



**Figure 2.17.** Possible mechanism of the enhanced photocatalytic performance for $ATiO_2$-BiOBr-Sepiolite towards formaldehyde and oxytetracycline under visible light irradiation [59].

## 2.9. Reaction kinetics of $TiO_2$/clay composites in the photodegradation of organic water contaminants

The action of $TiO_2$/clay photocatalysts on organic pollutants is through the adsorption of the pollutants on the catalyst surface, and the subsequent photodegradation and mineralization of the adsorbed pollutants facilitated by the photogenerated ROS to release products. This type of process has been termed the "adsorb and shuttle mechanism" because it is predicated on the highly adsorbing domains of clay which increases the density of pollutants near the $TiO_2$ photoactive sites which then facilitate the photodegradation processes [155]. The photodegradation mechanism can be explained using two main kinetic models: the pseudo-first-order rate law and the Langmuir−Hinshelwood kinetic model [156].

If the photooxidation of organic pollutants obeys the pseudo-first-order rate law, a linear regression curve (LRC) of $ln\left(\frac{C}{C_0}\right)$ against *t* is observed: where *C* is the concentration at time t, $C_0$ is the initial concentration at t=0, and the slope of the LRC is equal to the negative value of the pseudo-first-order rate constant (*k*). If the deviation from linearity is low then the reaction

obeys the pseudo-first-order rate law shown in **equation 2.9** which can also be presented as a decaying exponential in **equation 2.10.**

$$ln\left(\frac{C}{C_0}\right) = -kt \quad (2.9)$$

$$C = C_o e^{-kt} \quad (2.10)$$

Most photodegradation processes involving $TiO_2$/clay heterostructures are explained using the pseudo-first-order rate law [156].

Chen et al. [128] and Mishra et al. [156] explained the $TiO_2$/clay photodegradation process of organic pollutants according to the Langmuir−Hinshelwood model in **equation 2.11**.

$$R = -\frac{dC}{dt} = \frac{kKC}{1+KC}, \quad (2.11)$$

where *C* is the concentration, *R* is the instantaneous rate of reaction at time *t*, *k* is the intrinsic rate constant and *K* is the adsorption equilibrium constant. When the adsorption is weak or when the concentration is very low, $K \ll 1$ and therefore $1 + KC \sim 1$ and the Langmuir−Hinshelwood equation is reduced to the pseudo-first-order model shown in **equation 2.12** where the apparent rate constant $K_{app} = kK$.

$$R = -\frac{dC}{dt} = kKC \quad (2.12)$$

Solving the simplified first-order differential model gives **equation 2.13** shown below.

$$ln\left(\frac{C}{C_0}\right) = -K_{app}t \quad (2.13)$$

where $C_0$ is the initial concentration and $-K_{app}$ is the slope from the LRC of the $ln\left(\frac{C}{C_0}\right)$ against t plot.

At t=0, **equation 2.11** can be written as the initial rate shown in **equation 2.14** which when reciprocated gives **equation 2.15** [156]**.** Therefore plotting $\frac{1}{R_0}$ against $\frac{1}{C_0}$ gives an LRC if the reaction is explained by the Langmuir−Hinshelwood model [156].

$$R_0 = \frac{kKC_0}{1+KC_0} \quad (2.14)$$

$$\frac{1}{R_0} = \frac{1}{KC_0} + \frac{1}{k} \quad (2.15)$$

## 2.10. Phenol degradation mechanism on $TiO_2$/clay composites

Over the years there has been limited information on the proposal of a reaction mechanism for photodegradation of phenol on $TiO_2$/clay photocatalysts. The success of proposing a reasonable mechanism is based on the successful study of the dominant ROS that are responsible for the photodegradation process and the accuracy of the chromatographic technique used to track the reaction intermediates. Recently, two studies have been carried out to study the photodegradation mechanism of phenol on $TiO_2$-pyrophyllite heterostructures shown in **Figure 2.18** [157,158]. Pyrophyllite is considered as the simplest prototype for 2:1 dioctahedral phyllosilicates (clays) with $Al_2[Si_4O_{10}](OH)_2$ as its chemical structure [159].

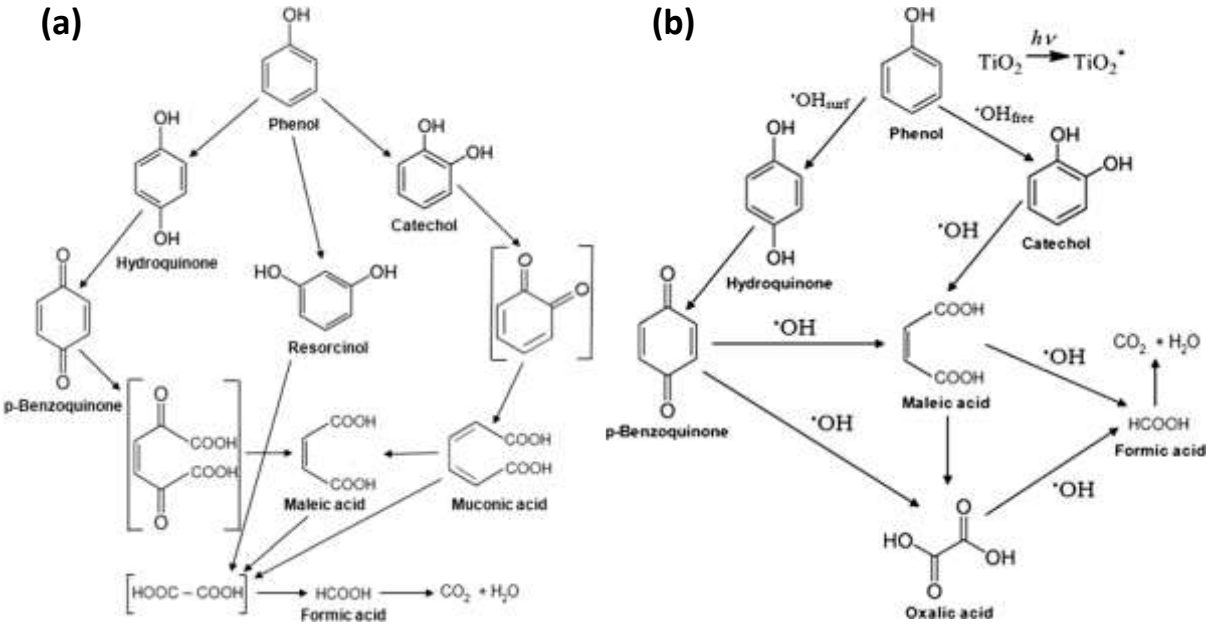



**Figure 2.18.** (a) Reaction mechanism of the photodegradation of phenol on $TiO_2$-pyrophyllite composite proposed El Gaidoumi [157] and (b) their follow-up study [158].

## 2.11. Fabricating usable $TiO_2$/clay products

While $TiO_2$/clay nanocomposites are generally regarded as promising light active adsorbents due to their resistance to fouling, good adsorption capacity, and improved porosity induced through pillarization exposing more surfaces for contact with pollutant molecules in water, there is still a need to process them into industrially applicable products. Recently, tuning the morphologies of $TiO_2$/clay composites through pressing $Fe_2O_3$-$TiO_2$/clay into plates [160] and the recent Alginate/Bentonite/$TiO_2$ beads [161] have been explored as ways to improve the recyclability of $TiO_2$/clay composites for possible large scale application. However, there are

scanty reports on the application of non-engineered $TiO_2$/clay nanocomposites in larger pilot-scale and full-scale water remediation systems. Therefore the need to engineer viable and industrially usable $TiO_2$/clay-based products cannot be overemphasized. Currently, the most promising mode of application of $TiO_2$/clay photocatalysts in large-scale water remediation systems is through engineered products such as photoresponsive thin films [162–165], and membranes [166–170]. Most of the engineered materials can be dipped into the wastewater during water remediation and provide high photocatalytic activity and excellent recyclability. Specific photoreactors based on films [171] and membranes [172] have also been fabricated.

Despite the transition from application $TiO_2$/clay powders to the application of their engineered products, the need to fabricate quality $TiO_2$/clay powders is still relevant. This is because the chemical, physical and optoelectronic properties of the $TiO_2$/clay powders which are platform materials of the products remain unchanged in the products and this has consequences on the performance of the products.

## 2.12. Overview of the latest trends in the fabrication of effective $TiO_2$/clay composites

Recent trends in $TiO_2$/clay chemistry lay more emphasis on the induction of favorable physicochemical and optoelectronic properties. Suitable physicochemical properties include high porosity, high surface area, and improved surface acidity. Favorable optoelectronic parameters include narrowed bandgap, extended exciton lifetime, charge separation, induction of oxygen vacancies.

Strategies such as the pre-treatment of the clay minerals, the use of specific synthetic conditions, and post-treatment methods impart specific physicochemical and morphological properties of the resulting composites. Clay pre-treatment procedures include the use of acids [102], sodium salts and bases [13,154], thermal exfoliation [173], magnetizing clays [128,146,147], and the use of organic sacrificial templates as swelling agents [145,174–183]. While acid treatment dredges acid-soluble materials from the clay pore channels resulting in a larger specific surface area clay supports [184], concentrated acids may remove the Mg and Al cations resulting in increased silica concentration in the resulting high surface area silica nanolayers with good adsorption capacities [185]. Sodium salts and bases replace polyvalent cations with monovalent sodium ions improving the adsorption capacity of the clay [13].

Thermal exfoliation expands the expansible clays so that they have a lower density suitable for the fabrication of easily recyclable floating $TiO_2$/clay catalysts [173].

Synthesis conditions such as microwave irradiation, intensified hydrothermal treatment, and acidic conditions also direct the physicochemical properties. Generally, microwave-prepared $TiO_2$/clay composites have high anatase content, high porosity, and specific surface area [108,109,111,112,186]. Hydrothermal processes result in efficient catalysts with large crystalline $TiO_2$ grains but their surface area is low [101,187–189]. The inclusion of sacrificial organic polymer templates leads to porous clay heterostructures (PCHs) and delaminated porous clay heterostructures (DPCHs) with improved photocatalytic activity. The chain length and concentration of the surfactant which functions as a clay swelling agent and structural regulator influence the delamination of the $TiO_2$/clay composites and the shape of the $TiO_2$ pillars [145,174–183]. In the hydrothermal treatment process under acidic conditions, the type of strong acid used directs the $TiO_2$ phases that can be formed. It has been observed that nitric acid favors all three $TiO_2$ phases, and sulfuric acid favors the anatase phase [185].

The efficiency of $TiO_2$/clay heterostructures in any photocatalytic application is based on the number and diffusion radius of electrons and holes generated which are responsible for the in situ formation of ROS. Therefore, the ease of generation, separation, and extension of recombination of electrons and holes, and good interaction between them and the various pollutants are principal thermodynamical parameters. To improve these optoelectronic abilities of $TiO_2$/clay composites, strategies to incorporate foreign species such as doping, co-pillaring, impregnation, deposition of plasmonic metals, and formation of heterojunctions with species graphitic carbon nitride, graphene oxide, and various semiconductor heterostructures are employed. The incorporated photosensitizers result in narrowed bandgap as low as 2.53 eV for amorphous $TiO_2$-BiOBr-Sep [59]. Lately, post-synthesis organic functionalization using organics such as acetic acid has been used to improve the $OH^{\bullet}$ generation [190].

$TiO_2$/clay-based composites have been used to develop a new class of simultaneous hybrid AOP configurations and systems. Configurations include the simultaneous photocatalysis and Fenton processes afforded $Fe_2O_3$-$TiO_2$/clay composite heterostructures attributed to the existence of iron in its $Fe^{3+}$ form rather than the iron (III) oxide form during photocatalysis in the presence of $H_2O_2$ [191,192] A novel AOP system reviewed in our work is the use of $TiO_2$/clay-based composites in activating peroxymonosulfate (PMS) [193] to generate $SO_4^{\bullet-}$ as an extra ROS in addition to the $H_2O_2$, $^1O_2$, $O_2^{\bullet-}$, $OH^{\bullet}$ and holes. Much research will be needed to explore the use of clay-based $TiO_2$ composites in the generation of other ROS in addition to the traditional ones.

While the development of efficient $TiO_2$/clay-based heterostructures for the treatment of water among other photocatalytic applications is a never-ending quest, strides in the direction of ideal $TiO_2$/clay photocatalysts have been undertaken. An ideal catalyst should be porous, have high adsorption capacity, have good catalytic activity in visible light, have a sufficient number of oxygen vacancies, have functionalized surfaces for $OH^{\bullet}$ generation, degrade high pollutant concentration, and be easy to recover after application.

In as much as developing ideal $TiO_2$/clay photocatalysts is principal, the development of materials and systems that exploit the $TiO_2$/clay photocatalysts maximally to remediate aqueous matrices with miscellaneous pollutants under optimized conditions is essential. Going forward, much focus is expected on the fabrication of engineered photoresponsive $TiO_2$/clay materials with antifouling properties, enhanced recyclability, and activity in the remediation of high volume multifarious organic matrices. More research outputs on designs of engineered photoresponsive membranes [166–168,170] and thin films [162–165] fabricated from $TiO_2$/clay nanocomposites as nanofillers or active layers are expected due to their resistance to fouling and high rejection coefficients. Moreover, a plethora of photoreactor designs based on $TiO_2$/clay nanocomposites, photoresponsive $TiO_2$/clay films [171], and membranes [172] as photoactive species are also expected as they have the potential for real-life applications.

## References


[1] N.R. Khalid, A. Majid, M.B. Tahir, N.A. Niaz, S. Khalid, pollutants: A review, Ceram. Int. 43 (2017) 14552–14571. https://doi.org/10.1016/j.ceramint.2017.08.143.

[2] H. Miyabe, S. Kohtani, Photocatalytic single electron transfer reactions on $TiO_2$, Sci. China Chem. 62 (2019) 1439–1449. https://doi.org/10.1007/s11426-019-9626-9.

[3] Y. Cai, Y. Ping, Review on charge transfer and chemical activity of $TiO_2$: Mechanism and applications, Prog. Surf. Sci. 91 (2016) 183–202. https://doi.org/10.1016/j.progsurf.2016.11.001.

[4] J. Schneider, M. Matsuoka, M. Takeuchi, J. Zhang, Y. Horiuchi, M. Anpo, D.W. Bahnemann, Understanding $TiO_2$ Photocatalysis: Mechanisms and Materials, Chem. Rev. 114 (2014) 9919–9986. doi.org/10.1021/cr5001892.

[5] J. Low, B. Cheng, J. Yu, Surface modification and enhanced photocatalytic $CO_2$ reduction performance of $TiO_2$: a review, Appl. Surf. Sci. 392 (2017) 658–686. https://doi.org/10.1016/j.apsusc.2016.09.093.

[6] F. Salvadores, O.M. Alfano, M.M. Ballari, Assessment of the indoor air purification by photocatalytic paints, Lat. Am. Appl. Res. 50 (2020) 71–76.

[7] C. Pei, J. Zhu, F. Xing, Photocatalytic property of cement mortars coated with graphene/$TiO_2$ nanocomposites synthesized via sol-gel assisted electrospray method, J. Clean. Prod. 279 (2021) 123590. https://doi.org/10.1016/j.jclepro.2020.123590.

[8] Z. Liu, H. Jiang, M. Yuan, Study on $TiO_2$ photocatalytic materials in the purification of highway tunnel tail gas, E3S Web Conf. 233 (2021) 01073 https://doi.org/10.1051/e3sconf/202123301073.

[9] D. Zhu, Q. Zhou, Action and mechanism of semiconductor photocatalysis on degradation of organic pollutants in water treatment: A review, Environmental Nanotechnology, Monitoring & Management 12 (2019) 100255. https://doi.org/10.1016/j.enmm.2019.100255.

[10] Y.C. Chen, C.H. Liao, W.T. Shen, C. Su, Y.C. Wu, M. H. Tsai, S.S. Hsiao, K.P. Yu, C. heng Tseng, Effective disinfection of airborne microbial contamination in hospital wards using a zero-valent nano-silver/$TiO_2$-chitosan composite, Indoor Air. 29 (2019) 439–449. https://doi.org/10.1111/ina.12543.

[11] V. Rodríguez-González, S. Obregón, O.A. Patrón-Soberano, C. Terashima, A. Fujishima, An approach to the photocatalytic mechanism in the $TiO_2$-nanomaterials microorganism interface for the control of infectious processes, Appl. Catal. B Environ.

270 (2020) 118853. https://doi.org/10.1016/j.apcatb.2020.118853.

[12] I. De Pasquale, C. Lo Porto, M. Dell'Edera, F. Petronella, A. Agostiano, M.L. Curri, R. Comparelli, Photocatalytic $TiO_2$-Based Nanostructured Materials for Microbial Inactivation, Catalysts. 10 (2020) 1–46. https://doi.org/10.3390/catal10121382.

[13] E. Tao, X. Xiao, S. Yang, A new synthesizing method of $TiO_2$ with montmorillonite: Effective photoelectron transfer to degrade Rhodamine B, Sep. Purif. Technol. 258 (2021) 118070. https://doi.org/10.1016/j.seppur.2020.118070.

[14] X. Hu, X. Hu, Q. Peng, L. Zhou, X. Tan, L. Jiang, C. Tang, H. Wang, S. Liu, Y. Wang, Z. Ning, Mechanisms underlying the photocatalytic degradation pathway of ciprofloxacin with heterogeneous $TiO_2$, Chem. Eng. J. 380 (2020) 122366. https://doi.org/10.1016/j.cej.2019.122366.

[15] A. Fernandes, P. Mako, Z. Wang, G. Boczkaj, Synergistic effect of $TiO_2$ photocatalytic advanced oxidation processes in the treatment of refinery effluents, Chem. Eng. J. 391 (2020) 123488. https://doi.org/10.1016/j.cej.2019.123488.

[16] S.P. Keerthana, R. Yuvakkumar, G. Ravi, P. Kumar, M. Soliman, H.H. Alkhamis, A.F. Alrefaei, D. Velauthapillai, Chemosphere A strategy to enhance the photocatalytic efficiency of α-$Fe_2O_3$, Chemosphere. 270 (2021) 129498. https://doi.org/10.1016/j.chemosphere.2020.129498.

[17] L. Song, G. Wang, X. Su, J. Hu, Y. Cao, Facile synthesis of hollow α-$Fe_2O_3$ nanospindle and its superior photocatalytic performance for water oxidation, Catal. Commun. 154 (2021) 106306. https://doi.org/10.1016/j.catcom.2021.106306.

[18] K. Hamidian, A. Najafidoust, A. Miri, M. Sarani, Photocatalytic performance on degradation of Acid Orange 7 dye using biosynthesized un-doped and Co-doped $CeO_2$ nanoparticles, Mater. Res. Bull. 138 (2021) 111206. https://doi.org/10.1016/j.materresbull.2021.111206.

[19] R. Fiorenza, S.A. Balsamo, L.D. Urso, S. Scir, M.V. Brundo, R. Pecoraro, E.M. Scalisi, V. Privitera, G. Impellizzeri, Advanced Oxidation Processes, Catalysts. 10 (2020) 1–16. https://doi:10.3390/catal10040446.

[20] P. Uthirakumar, M. Devendiran, T. Hwan, S. Kalaiarasan, I. Lee, Materials Science & Engineering B Fabrication of flexible sheets of Cu/CuO/$Cu_2O$ heterojunction nanodisks: A dominant performance of multiple photocatalytic sheets under natural sunlight, Mater. Sci. Eng. B. 260 (2020) 114652. https://doi.org/10.1016/j.mseb.2020.114652.

[21] M.G. Peleyeju, E.L. Viljoen, $WO_3$-based catalysts for photocatalytic and photoelectrocatalytic removal of organic pollutants from water-A review, J. Water

Process Engineering 40 (2021) 101930. https://doi.org/10.1016/j.jwpe.2021.101930.

[22] S. Chavoshan, M. Khodadadi, N. Nasseh, Photocatalytic degradation of penicillin G from simulated wastewater using the UV/ZnO process: isotherm and kinetic study, J. Environ. Heal. Sci. Eng. 18 (2020) 107–117. https://doi.org/10.1007/s40201-020004427.

[23] P.A. Luque, O. Nava, C.A. Soto-robles, M.J. Chinchillas-Chinchillas, Improved photocatalytic efficiency of $SnO_2$ nanoparticles through green synthesis, Opt.- Int. J. Light Electron Opt. 206 (2020) 164299. https://doi.org/10.1016/j.ijleo.2020.164299.

[24] J. Liu, Q. Zhang, X. Tian, Y. Hong, Y. Nie, N. Su, G. Jin, Z. Zhai, C. Fu, Highly efficient photocatalytic degradation of oil pollutants by oxygen-deficient $SnO_2$ quantum dots for water remediation, Chem. Eng. J. 404 (2021) 127146. https://doi.org/10.1016/j.cej.2020.127146.

[25] K. Siwi, Ś. Dariusz, P. Rychtowski, D. Moszy, A. Zgo, The performance of multicomponent oxide systems based on $TiO_2$, $ZrO_2$ and $SiO_2$ in the photocatalytic degradation of Rhodamine B: Mechanism and kinetic studies, Colloids Surfaces A. 586 (2020) 124272. https://doi.org/10.1016/j.colsurfa.2019.124272.

[26] M. Fakhrul, R. Samsudin, S. Su, B.H. Hameed, Epigrammatic progress and perspective on the photocatalytic properties of $BiVO_4$-based photocatalyst in photocatalytic water treatment technology: A review, Journal of Molecular Liquids 268 (2018) 438–459. https://doi.org/10.1016/j.molliq.2018.07.051.

[27] S. Liu, H. Tang, H. Zhou, G. Dai, W. Wang, Photocatalytic performance of sandwich-like $BiVO_4$ sheets by microwave-assisted synthesis, Appl. Surf. Sci. 391 (2017) 542–547. https://doi.org/10.1016/j.apsusc.2016.06.184.

[28] X. Zhang, R. Li, M. Jia, S. Wang, Y. Huang, C. Chen, Degradation of ciprofloxacin in aqueous bismuth oxybromide (BiOBr) suspensions under visible light irradiation: A direct hole oxidation pathway, Chem. Eng. J. 274 (2015) 290–297. https://doi.org/10.1016/j.cej.2015.03.077.

[29] Z. Wang, H. Wang, X. Wu, T. Chang, Oxygen vacancies and p-n heterojunction modified BiOBr for enhancing donor density and separation efficiency under visible-light irradiation, J. Alloys Compd. 834 (2020) 155025. https://doi.org/10.1016/j.jallcom.2020.155025.

[30] Y. Wu, X. Du, Y. Kou, Y. Wang, F. Teng, Mesoporous $SiO_2$ nanostructure: Light-induced adsorption enhancement and its application in photocatalytic degradation of organic dye, Ceram. Int. 45 (2019) 24594–24600.

https://doi.org/10.1016/j.ceramint.2019.08.188.

[31] A. Fakhri, V. Kumar, H. Rabizadeh, S. Agarwal, N. Sadeghi, S. Tahami, Preparation and characterization of $WS_2$ decorated and immobilized on chitosan and polycaprolactone as biodegradable polymers nanofibers: Photocatalysis study and antibiotic-conjugated for antibacterial evaluation, Int. J. Biol. Macromol. 120 (2018) 1789–1793. https://doi.org/10.1016/j.ijbiomac.2018.09.207.

[32] J. Xiao, Y. Xie, J. Rabeah, A. Bru, H. Cao, Visible-Light Photocatalytic Ozonation Using Graphitic $C_3N_4$ Catalysts: A Hydroxyl Radical Manufacturer for Wastewater Treatment, Acc. Chem. Res. 53 (2020) 1024–1033. https://doi.org/10.1021/acs.accounts.9b00624.

[33] Q. Huang, C. Wang, D. Hao, W. Wei, L. Wang, Ultralight biodegradable 3D g-$C_3N_4$ aerogel for advanced oxidation water treatment driven by oxygen delivery channels and triphase interfaces, J. Clean. Prod. 288 (2021) 125091. https://doi.org/10.1016/j.jclepro.2020.125091.

[34] M. Selvaraj, A. Hai, F. Banat, M. Abu, Application and prospects of carbon nanostructured materials in water treatment: A review, J. Water Process Eng. 33 (2020) 100996. https://doi.org/10.1016/j.jwpe.2019.100996.

[35] U. Abd, L. Yong, C. Yin, E. Mahmoudi, A review of carbon quantum dots and their applications in wastewater treatment, Adv. Colloid Interface Sci. 278 (2020) 102124. https://doi.org/10.1016/j.cis.2020.102124.

[36] C. Karthikeyan, P. Arunachalam, K. Ramachandran, A.M. Al-mayouf, S. Karuppuchamy, Recent advances in semiconductor metal oxides with enhanced methods for solar photocatalytic applications, J. Alloys Compd. 828 (2020) 154281. https://doi.org/10.1016/j.jallcom.2020.154281.

[37] R. Katal, S. Masudy-Panah, M. Tanhaei, M. Tanhaeic, M.H.D.A. Farahani, H. Jiangyong, A review on the synthesis of the various types of anatase $TiO_2$ facets and their applications for photocatalysis, Chem. Eng. J. 384 (2020) 123384. https://doi.org/10.1016/j.cej.2019.123384.

[38] J. Chen, F. Qiu, W. Xu, S. Cao, H. Zhu, General Recent progress in enhancing photocatalytic efficiency of $TiO_2$ -based materials, Appl. Catal. A Gen. 495 (2015) 131–140. https://doi.org/10.1016/j.apcata.2015.02.013.

[39] C. Wang, X. Wang, W. Liu, The synthesis strategies and photocatalytic performances of $TiO_2$/MOFs composites: A state-of-the-art review, Chem. Eng. J. 391 (2020) 123601. https://doi.org/10.1016/j.cej.2019.123601.

[40] L.G. Devi, R. Kavitha, A review on nonmetal ion-doped titania for the photocatalytic degradation of organic pollutants under UV/solar light: Role of photogenerated charge carrier dynamics in enhancing the activity, Appl. Catal. B Environ. 140–141 (2013) 559–587. https://doi.org/10.1016/j.apcatb.2013.04.035.

[41] V. Aravindan, Y.S. Lee, R. Yazami, S. Madhavi, $TiO_2$ polymorphs in "rocking-chair" Li-ion batteries, Mater. Today. 18 (2015) 345–351. https://doi.org/10.1016/j.mattod.2015.02.015.

[42] Z. Liu, Y.G. Andreev, A. Robert Armstrong, S. Brutti, Y. Ren, P.G. Bruce, Nanostructured $TiO_2$ (B): the effect of size and shape on anode properties for Li-ion batteries, Prog. Nat. Sci. Mater. Int. 23 (2013) 235–244. https://doi.org/10.1016/j.pnsc.2013.05.001.

[43] B. Prasai, B. Cai, M.K. Underwood, J.P. Lewis, D.A. Drabold, Properties of amorphous and crystalline titanium dioxide from first principles, J. Mater. Sci. 47 (2012) 7515–7521. https://doi.org/10.1007/s10853-012-6439-6.

[44] F.C. Mocanu, V.L. Deringer, S.R. Elliott, Similarity Between Amorphous and Crystalline Phases: The Case of $TiO_2$, J. Phys. Chem. Lett. 9 (2018) 2985–2990. https://doi.org/10.1021/acs.jpclett.8b01067.

[45] S. Sun, P. Song, J. Cui, S. Liang, Amorphous $TiO_2$ nanostructures: Synthesis, fundamental properties, and photocatalytic applications, Catal. Sci. Technol. 9 (2019) 4198–4215. https://doi.org/10.1039/c9cy01020c.

[46] H.H. Pham, L. Wang, Oxygen vacancy and hole conduction in amorphous $TiO_2$, Phys.Chem.Chem.Phys. 2 (2015) 541–550. https://doi.org/10.1039/c4cp04209c.

[47] M. Landmann, E. Rauls, W.G. Schmidt, The electronic structure and optical response of rutile, anatase and brookite $TiO_2$, J. Phys. Condens. Matter. 24 (2012) 195503. https://doi.org/10.1088/0953-8984/24/19/195503.

[48] V. Etacheri, C. Di, J. Schneider, D. Bahnemann, S.C. Pillai, Visible-light activation of $TiO_2$ photocatalysts : Advances in theory and experiments, J. Photochem. Photobiol. C Photochem. Rev. 25 (2015) 1–29, https://doi.org/10.1016/j.jphotochemrev.2015.08.003.

[49] M.E. Manríquez, M.T. Valdez, A.S. Pliego, L. V. Castro, E. Ortiz-Islas, Oxidation of styrene oxide via chemical and photochemical methods using $TiO_2$-$CeO_2$-$V_2O_5$ catalysts, J. Photochem. Photobiol. A Chem. 395 (2020) 112505. https://doi.org/10.1016/j.jphotochem.2020.112505.

[50] J. Wen, X. Li, W. Liu, Y. Fang, J. Xie, Y. Xu, Photocatalysis fundamentals and surface modification of $TiO_2$ nanomaterials, Chinese J. Catal. 36 (2015) 2049–2070.

https://doi.org/10.1016/S1872-2067(15)60999-8.

[51] R. Qian, H. Zong, J. Schneider, G. Zhou, T. Zhao, Y. Li, Charge carrier trapping, recombination and transfer during $TiO_2$ photocatalysis: An overview, Catal. Today. 335 (2019) 78–90. https://doi.org/10.1016/j.cattod.2018.10.053.

[52] Y. Nam, L. Li, J.Y. Lee, O. V Prezhdo, Strong Influence of Oxygen Vacancy Location on Charge Carrier Losses in Reduced $TiO_2$ Nanoparticles, J. Phys. Chem. 10 (2019) 2676–2683. https://doi.org/10.1021/acs.jpclett.9b00987.

[53] M.K. Nowotny, T. Bak, J. Nowotny, Electrical Properties and Defect Chemistry of $TiO_2$ Single Crystal. I . Electrical Conductivity, J. Phys. Chem. B. 110 (2006) 16270–16282.

[54] B. Dong, T. Liu, C. Li, F. Zhang, Species, engineering and characterizations of defects in $TiO_2$-based photocatalyst, Chinese Chem. Lett. 29 (2018) 671–680. https://doi.org/10.1016/j.cclet.2017.12.002.

[55] Y. Nosaka, A.Y. Nosaka, Generation and Detection of Reactive Oxygen Species in Photocatalysis, Chem. Rev. 117 (2017) 11302–11336. https://doi.org/10.1021/acs.chemrev.7b00161.

[56] J. Hoigné, Wat. Sci. Tech. 35 4 (1997) 1–8.

[57] S. Kohtani, A. Kawashima, H. Miyabe, Reactivity of Trapped and Accumulated Electrons in, Catalysts. 7 (2017) 1–16. https://doi.org/10.3390/catal7100303.

[58] A. Fujishima, X. Zhang, D.A. Tryk, $TiO_2$ photocatalysis and related surface phenomena, Surf. Sci. Rep. 63 (2008) 515–582. https://doi.org/10.1016/j.surfrep.2008.10.001.

[59] X. Hu, C. Li, J. Song, S. Zheng, Z. Sun, Multidimensional assembly of oxygen vacancy-rich amorphous $TiO_2$-BiOBr-sepiolite composite for rapid elimination of formaldehyde and oxytetracycline under visible light, J. Colloid Interface Sci. 574 (2020) 61–73. https://doi.org/10.1016/j.jcis.2020.04.035.

[60] T. Jia, J. Zhang, J. Wu, D. Wang, Q. Liu, Y. Qi, B. Hu, P. He, W. Pan, X. Qi, Synthesis amorphous $TiO_2$ with oxygen vacancy as carriers transport channels for enhancing photocatalytic activity, Mater. Lett. 265 (2020) 127465. https://doi.org/10.1016/j.matlet.2020.127465.

[61] M.A. Vargas, J.E. Rodríguez-páez, Amorphous $TiO_2$ nanoparticles: Synthesis and antibacterial capacity, J. Non. Cryst. Solids. 459 (2017) 192–205. https://doi.org/10.1016/j.jnoncrysol.2017.01.018.

[62] K.K. Ghuman, C. V Singh, Self-Trapped Charge Carriers in Defected Amorphous $TiO_2$, J. Phys. Chem. C. 120 (2016) 27910–27916. https://doi.org/10.1021/acs.jpcc.6b07326.

[63] Q. Wang, J. Zhao, Y. Cong, Y. Zhang, Photo-sensitized Degradation of Dye Pollutants

on Amorphous $TiO_2$ under Visible Light Irradiation, Chinese J. Catal. 32 (2011) 1076–1082. DOI: 10.3724/SP.J.1088.2011.10336

[64] D. Zywitzki, H. Jing, H. Tuysuz, C.K. Chan, High surface area, amorphous titania with reactive $Ti^{3+}$ through a photo-assisted synthesis method for photocatalytic $H_2$ generation, J. Mater. Chem. A. 5 (2017) 10957–10967. https://doi.org/10.1039/c7ta01614j.

[65] C. Yi, Q. Liao, W. Deng, Y. Huang, J. Mao, B. Zhang, G. Wu, Science of the Total Environment The preparation of amorphous $TiO_2$ doped with cationic S and its application to the degradation of DCFs under visible light irradiation, Sci. Total Environ. 684 (2019) 527–536. https://doi.org/10.1016/j.scitotenv.2019.05.338.

[66] P. Shao, J. Tian, Z. Zhao, W. Shi, S. Gao, F. Cui, Amorphous $TiO_2$ doped with carbon for visible light photodegradation of rhodamine B and 4-chlorophenol, Appl. Surf. Sci. 324 (2015) 35–43. https://doi.org/10.1016/j.apsusc.2014.10.108.

[67] A. Luna-Flores, J.L. Sosa-Sanchez, M.A. Morales-Sánches, R. Agustín-Serrano, J.A. Luna-López, Amorphous $TiO_2$ Photocatalyst Obtained by Microwave-Assisted Synthesis for the Degradation of Rhodamine B, Materials (Basel). 2 (2017) 1447. https://doi.org/10.3390/ma10121447.

[68] Z. Sun, X. Li, J. Liu, Y. Li, B. Zhu, A. Zhu, A promising visible-light photocatalyst: $H_2$ plasma-activated, J. Catal. 375 (2019) 380–388. https://doi.org/10.1016/j.jcat.2019.05.027.

[69] H. Liang, Q. Meng, X. Wang, H. Zhang, J. Wang, Nanoplasmonically Engineered Interfaces on Amorphous $TiO_2$ for Highly Efficient Photocatalysis in Hydrogen Evolution, ACS Appl. Mater. Interfaces. 10 (2018) 14145–14152. https://doi.org/10.1021/acsami.8b00677.

[70] J. Lyu, Z. Zhou, Y. Wang, J. Li, Q. Li, Y. Zhang, X. Ma, J. Guan, X. Wei, Platinum-enhanced amorphous $TiO_2$-filled mesoporous $TiO_2$ crystals for the photocatalytic mineralization of tetracycline hydrochloride, J. Hazard. Mater. 373 (2019) 278–284. https://doi.org/10.1016/j.jhazmat.2019.03.096.

[71] Q. Wang, M. Chen, N. Zhu, X. Shi, H. Jin, Y. Zhang, Y. Cong, Preparation of AgI sensitized amorphous $TiO_2$ as novel high-performance photocatalyst for environmental applications, J. Colloid Interface Sci. 448 (2015) 407–416. https://doi.org/10.1016/j.jcis.2015.01.085.

[72] A.K.P.D. Savio, J. Fletcher, K. Smith, R. Iyer, J.M. Bao, F.C.R. Hernández, Environmentally effective photocatalyst CoO-$TiO_2$ synthesized by thermal precipitation of Co in amorphous $TiO_2$, Appl. Catal. B Environ. 182 (2016) 449–455.

https://doi.org/10.1016/j.apcatb.2015.09.047.

[73] L. Yue, R. Cheng, W. Ding, J. Shao, J. Li, J. Lyu, Composited micropores constructed by amorphous $TiO_2$ and graphene for degrading volatile organic compounds, Appl. Surf. Sci. 471 (2019) 1–7. https://doi.org/10.1016/j.apsusc.2018.11.232.

[74] L. Wu, X. Wang, W. Wang, J. Li, X. Li, Fabrication of amorphous $TiO_2$ shell layer on $Ag_2CO_3$ surface with enhanced photocatalytic activity and photostability, J. Alloys Compd. 806 (2019) 603–610. https://doi.org/10.1016/j.jallcom.2019.07.200.

[75] H. Deng, X. Wang, L. Wang, Z. Li, P. Liang, J. Ou, K. Liu, L. Yuan, Z. Jiang, L. Zheng, Z. Chai, W. Shi, Enhanced photocatalytic reduction of aqueous Re (VII) in ambient air by amorphous $TiO_2$/g-$C_3N_4$ photocatalysts: Implications for Tc (VII) elimination, Chem. Eng. J. 401 (2020) 125977. https://doi.org/10.1016/j.cej.2020.125977.

[76] Y. Xu, J. Song, F. Chen, X. Wang, H. Yu, J. Yu, Amorphous Ti(IV)-modified $Bi_2WO_6$ with enhanced photocatalytic performance, RSC Adv. 6 (2016) 65902–65910. https://doi.org/10.1039/c6ra10616a.

[77] X.X. Wei, H. Cui, S. Guo, L. Zhao, W. Li, Hybrid BiOBr-$TiO_2$ nanocomposites with high visible-light photocatalytic activity for water treatment, J. Hazard. Mater. 263 (2013) 650–658. https://doi.org/10.1016/j.jhazmat.2013.10.027.

[78] X. Wang, W. Yang, F. Li, J. Zhao, R. Liu, S. Liu, B. Li, Construction of amorphous $TiO_2$/BiOBr heterojunctions via facets coupling for enhanced photocatalytic activity, 292 (2015) 126–136. https://doi.org/10.1016/j.jhazmat.2015.03.030.

[79] W. Deng, F. Pan, B. Batchelor, B. Jung, P. Zhang, A. Abdel-Wahab, H. Zhou, Y. Li, Mesoporous $TiO_2$-BiOBr microspheres with tailorable adsorption capacities for photodegradation of organic water pollutants: Probing adsorption-photocatalysis synergy by combining experiments and kinetic modeling, Environ. Sci. Water Res. Technol. 5 (2019) 769–781. https://doi.org/10.1039/c8ew00922h.

[80] Y. Li, Z. Wang, B. Huang, Y. Dai, X. Zhang, X. Qin, Synthesis of BiOBr-PVP hybrids with enhanced adsorption-photocatalytic properties, Appl. Surf. Sci. 347 (2015) 258–264. https://doi.org/10.1016/j.apsusc.2015.04.105.

[81] C. Xue, J. Xia, T. Wang, S. Zhao, G. Yang, B. Yang, Y. Dai, G. Yang, A facile and efficient solvothermal fabrication of three-dimensionally hierarchical BiOBr microspheres with exceptional photocatalytic activity, Mater. Lett. 133 (2014) 274–277. https://doi.org/10.1016/j.matlet.2014.07.016.

[82] S.S. Imam, R. Adnan, N.H.M. Kaus, The photocatalytic potential of BiOBr for wastewater treatment: A mini-review, J. Environ. Chem. Eng. 9 (2021) 105404.

https://doi.org/10.1016/j.jece.2021.105404.

[83] A.M. Ganose, M. Cuff, K.T. Butler, A. Walsh, D.O. Scanlon, Interplay of Orbital and Relativistic Effects in Bismuth Oxyhalides: BiOF, BiOCl, BiOBr, and BiOI, Chem. Mater. 28 (2016) 1980–1984. https://doi.org/10.1021/acs.chemmater.6b00349.

[84] M.X. Song, M. Du, Q. Liu, F. Xing, C. Huang, X. Qiu, Enhancement of photocatalytic activities in hierarchical BiOBr microflowers induced by oxygen vacancies, Catal. Today. 335 (2019) 193–199. https://doi.org/10.1016/j.cattod.2018.11.006.

[85] Q. Chi, G. Zhu, D. Jia, W. Ye, Y. Wang, J. Wang, T. Tao, F. Xu, G. Jia, W. Li, P. Gao, Built-in electric field for photocatalytic overall water splitting through a $TiO_2$/BiOBr P-N heterojunction, Nanoscale. 13 (2021) 4496–4504. https://doi.org/10.1039/d0nr08928a.

[86] J.M. Moreno-Maroto, J. Alonso-Azcárate, What is clay? A new definition of "clay" based on plasticity and its impact on the most widespread soil classification systems, Appl. Clay Sci. 161 (2018) 57–63. https://doi.org/10.1016/j.clay.2018.04.011.

[87] X. Lingling, G. Wei, W. Tao, Y. Nanru, Study on fired bricks with replacing clay by fly ash in high volume ratio, Constr. Build. Mater. 19 (2005) 243–247. https://doi.org/10.1016/j.conbuildmat.2004.05.017.

[88] H.H. Murray, Overview-clay mineral applications, Appl. Clay Sci. 5 (1991) 379–395. https://doi.org/10.1016/0169-1317(91)90014-Z.

[89] I.E. Odom, Smectite clay minerals: properties and uses., Philos. Trans. R. Soc. London. 409 (1984) 391–409. https://doi.org/10.1098/rsta.1984.0036.

[90] F. Uddin, Clays, nanoclays, and montmorillonite minerals, Metall. Mater. Trans. A Phys. Metall. Mater. Sci. 39 (2008) 2804–2814. https://doi.org/10.1007/s11661-008-9603-5.

[91] S. Marcos, Bentonites-Clays for Molecular Engineering, Elements. 5 (2009) 89–92. https://doi.org/10.2113/gselements.5.2.89.

[92] R.M. Hazen, D.A. Sverjensky, D. Azzolini, D.L. Bish, S.C. Elmore, L. Hinnov, R.E. Milliken, Clay mineral evolution, Am. Mineral. 98 (2013) 2007–2029. http://dx.doi.org/10.2138/am.2013.4425

[93] M. Valášková, Clays , clay minerals and cordierite ceramics-A review, Ceram.-Silikáty. 59 (2015) 331–340.

[94] T. V Alekseeva, A.O. Alekseev, Mineralogy and micromorphology Rectorite as a Syngenetic Component of a Soddy-Podzolic Soil, Eurasian Soil Sci. 53 (2020) 1287–1294. https://doi.org/10.1134/S1064229320100038.

[95] F. Guo, S. Aryana, Y. Han, Y. Jiao, A review of the synthesis and applications of polymer-nanoclay composites, Appl. Sci. 8 (2018) 1–29. https://doi.org/10.3390/app8091696.

[96] S.W. Bailey, Structures of layer silicates, in: G.W. Brindley, G. Brown (Eds.), Crystal Structures of Clay Minerals and Their X-ray identification. Mineralogical Society, London, 1980, pp. 1–124.

[97] Z. Liu, A. Wang, H. Ma, D. Li, L. Xing, Visible-light-driven photocatalytic activity of kaolinite : Sensitized by in situ growth of Cu-$TiO_2$, Env. Prog Sustain. Energy. (2020) 1–10. https://doi.org/10.1002/ep.13479.

[98] L. Zeng, H. Sun, T. Peng, X. Lv, Comparison of the Phase Transition and Degradation of Methylene Blue of $TiO_2$, $TiO_2$/Montmorillonite Mixture and $TiO_2$/Montmorillonite Composite, Front. Chem. 7 (2019) 1–10. https://doi.org/10.3389/fchem.2019.00538.

[99] L. Barbosa, Vietro, L. Marcale, E.J. Nassar, P.S. Calefi, M.A. Vicente, R. Trujillano, V. Rives, A. Gil, S.A. Korili, K.J. Ciuffi, E.H. De Faria, Kaolinite-titanium oxide nanocomposites prepared via sol-gel as heterogeneous photocatalysts for dyes degradation, Catal. Today. 246 (2015) 133–142. https://doi.org/10.1016/j.cattod.2014.09.019.

[100] L.D. Mora, L.F. Bonfim, L. V. Barbosa, T.H. da Silva, E.J. Nassar, K.J. Ciuffi, B. González, M.A. Vicente, R. Trujillano, V. Rives, M.E. Pérez-Bernal, S. Korili, A. Gil, E.H. de Faria, White and red Brazilian Sao Simao's kaolinite-$TiO_2$ nanocomposites as catalysts for toluene photodegradation from aqueous solutions, Materials (Basel). 12 (2019) 3943. https://doi.org/10.3390/MA12233943.

[101] M. Huo, H. Guo, Y. Jiang, H. Ju, B. Xue, A facile method of preparing sandwich layered $TiO_2$ in between montmorillonite sheets and its enhanced UV-light photocatalytic activity, Journal Photochem. Photobiol. A Chem. 358 (2018) 121–129. https://doi.org/10.1016/j.jphotochem.2018.02.012.

[102] Suhartana, A. Ayu Janitra, C. Azmiyawati, A. Darmawan, Synthesis of $TiO_2$ pillared clay and its application to the decolourization of crystal violet dyes, IOP Conf. Ser. Mater. Sci. Eng. 509 (2019). https://doi.org/10.1088/1757-899X/509/1/012140.

[103] H. Liang, Z. Wang, L. Liao, L. Chen, Z. Li, J. Feng, High-performance photocatalysts: Montmorillonite supported-nano $TiO_2$ composites, Optik (Stuttg). 136 (2017) 44–51. https://doi.org/10.1016/j.ijleo.2017.02.018.

[104] C. Li, N. Zhu, S. Yang, X. He, S. Zheng, Z. Sun, D.D. Dionysiou, A review of clay-based photocatalysts: Role of phyllosilicate mineral in interfacial assembly,

microstructure control and performance regulation, Chemosphere. 273 (2021) 129723. https://doi.org/10.1016/j.chemosphere.2021.129723.

[105] H. Bel, M.E. Galvez, P. Da, M. Ben, $TiO_2$/clay as a heterogeneous catalyst in photocatalytic/photochemical oxidation of anionic reactive blue 19, Arab. J. Chem. 12 (2019) 1454–1462. https://doi.org/10.1016/j.arabjc.2014.11.006.

[106] N.V.S. Praneeth, S. Paria, Clay-semiconductor nanocomposites for photocatalytic applications, in clay minerals: properties, in: T.K. Sen (Ed.), Occurrence and Uses, Nova Science Publishers, New York, 2017.

[107] B. Damardji, H. Khalaf, L. Duclaux, B. David, Preparation of $TiO_2$-pillared montmorillonite as photocatalyst Part I. Microwave calcination, characterization, and adsorption of a textile azo dye, Appl. Clay Sci. 44 (2009) 201–205. https://doi.org/10.1016/j.clay.2008.12.010.

[108] I. Labib, H. Boutoumi, H. Khalaf, Synergistic Effect of Microwave Calcination and Sonophotocatalytic Activity of $TiO_2$-Montmorillonite on The Degradation of Direct Yellow 106 and Disperse Violet 1, Bull. Chem. React. Eng. Catal. 15 (2020) 304–318. https://doi.org/10.9767/bcrec.15.2.6999.304-318.

[109] S. Sun, Y. Jiang, L. Yu, F. Li, Z. Yang, T. Hou, D. Hu, M. Xia, Enhanced photocatalytic activity of microwave treated $TiO_2$ pillared montmorillonite, Mater. Chem. Phys. 98 (2006) 377–381. https://doi.org/10.1016/j.matchemphys.2005.09.047.

[110] J. Ma, Y. Jia, Y. Jing, J. Sun, Y. Yao, Synthesis and photocatalytic activity of $TiO_2$-hectorite composites, Appl. Clay Sci. 46 (2009) 114–116. https://doi.org/10.1016/j.clay.2009.07.011.

[111] F. Zhou, C. Yan, T. Liang, Q. Sun, H. Wang, Photocatalytic degradation of Orange G using sepiolite-$TiO_2$ nanocomposites: Optimization of physicochemical parameters and kinetics studies, Chem. Eng. Sci. 183 (2018) 231–239. https://doi.org/10.1016/j.ces.2018.03.016.

[112] F. Zhou, C. Yan, H. Wang, S. Zhou, S. Komarneni, Sepiolite-$TiO_2$ nanocomposites for photocatalysis: Synthesis by microwave hydrothermal treatment versus calcination, Appl. Clay Sci. 146 (2017) 246–253. https://doi.org/10.1016/j.clay.2017.06.010.

[113] J. Liu, M. Dong, S. Zuo, Y. Yu, Solvothermal preparation of $TiO_2$/montmorillonite and photocatalytic activity, Appl. Clay Sci. 43 (2009) 156–159. https://doi.org/10.1016/j.clay.2008.07.016.

[114] A. Nikolopoulou, D. Papoulis, S. Komarneni, P. Tsolis-katagas, D. Panagiotaras, H.G. Kacandes, P. Zhang, S. Yin, T. Sato, Solvothermal preparation of $TiO_2$/saponite

nanocomposites and photocatalytic activity, Appl. Clay Sci. 46 (2009) 363–368. https://doi.org/10.1016/j.clay.2009.09.007.

[115] R. Djellabi, M.F. Ghorab, G. Cerrato, S. Morandi, S. Gatto, V. Oldani, A. Di Michele, C.L. Bianchi, Photoactive $TiO_2$-montmorillonite composite for degradation of organic dyes in water, J. Photochem. Photobiol. A Chem. 295 (2015) 57–63. https://doi.org/10.1016/j.jphotochem.2014.08.017.

[116] L. Laysandra, M. Winda, M. Kartika, F. Edi, Adsorption and photocatalytic performance of bentonite-titanium dioxide composites for methylene blue and rhodamine B decoloration, Heliyon. 3 (2017). https://doi.org/10.1016/j.heliyon.2017.e00488.

[117] S. Miao, Z. Liu, B. Han, J. Zhang, X. Yu, J. Du, Z. Sun, Synthesis and characterization of $TiO_2$-montmorillonite nanocomposites and their application for removal of methylene blue, J. Mater. Chem. 16 (2006) 579–584. https://doi.org/10.1039/b511426h.

[118] C. Belver, J. Bedia, J.J. Rodriguez, Titania-clay heterostructures with solar photocatalytic applications, Appl. Catal. B Environ. 176–177 (2015) 278–287. https://doi.org/10.1016/j.apcatb.2015.04.004.

[119] K. Mogyorósi, I. Dékány, J.H. Fendler, Preparation and characterization of clay mineral intercalated titanium dioxide nanoparticles, Langmuir. 19 (2003) 2938–2946. https://doi.org/10.1021/la025969a.

[120] R. Kun, K. Mogyorósi, I. Dékány, Synthesis and structural and photocatalytic properties of $TiO_2$/montmorillonite nanocomposites, Appl. Clay Sci. 32 (2006) 99–110. https://doi.org/10.1016/j.clay.2005.09.007.

[121] J.G. Carriazo, M. Moreno-Forero, R.A. Molina, S. Moreno, Incorporation of titanium and titanium-iron species inside a smectite-type mineral for photocatalysis, Appl. Clay Sci. 50 (2010) 401–408. https://doi.org/10.1016/j.clay.2010.09.007.

[122] J. Li, W. Wang, A study of photodegradation of sulforhodamine B on Au–$TiO_2$/bentonite under UV and visible light irradiation, Solid State Sci. 11 (2009) 2037–2043. https://doi.org/10.1016/j.solidstatesciences.2009.09.012.

[123] Y. Yang, R. Liu, G. Zhang, L. Gao, W. Zhang, Preparation and photocatalytic properties of visible-light-driven Ag-AgCl-$TiO_2$/palygorskite composite, J. Alloys Compd. 657 (2016) 801–808. https://doi.org/10.1016/j.jallcom.2015.10.078.

[124] S. Liu, D. Zhu, J. Zhu, Q. Yang, H. Wu, A. Agcl, Preparation of Ag@AgCl-doped $TiO_2$/sepiolite and its photocatalytic mechanism under visible light, J. Environ. Sci. 60 (2017) 43–52. https://doi.org/10.1016/j.jes.2016.12.026.

[125] Y. Yang, G. Zhang, W. Xu, Facile synthesis and photocatalytic properties of Ag-AgCl-

$TiO_2$/rectorite composite, J. Colloid Interface Sci. 376 (2012) 217–223. https://doi.org/10.1016/j.jcis.2012.03.003.

[126] D. Zhang, Photocatalytic degradation of organic compounds by Au-$TiO_2$/sepiolite composites as the highly efficient catalysts, Russ. J. Phys. Chem. A. 88 (2014) 2252–2259. https://doi.org/10.1134/S003602441412005X.

[127] Y. Shi, Z. Yang, B. Wang, H. An, Z. Chen, H. Cui, Adsorption and photocatalytic degradation of tetracycline hydrochloride using a palygorskite-supported $Cu_2O$-$TiO_2$ composite, Appl. Clay Sci. 119 (2016) 311–320. https://doi.org/10.1016/j.clay.2015.10.033.

[128] W. Chen, H. Xiao, H. Xu, T. Ding, Y. Gu, Photodegradation of methylene blue by $TiO_2$-$Fe_3O_4$-bentonite magnetic nanocomposite, Int. J. Photoenergy. 2015 (2015) 7. https://doi.org/10.1155/2015/591428.

[129] X. Cao, C. Liu, Y. Hu, W. Yang, J. Chen, Synthesis of N/Fe comodified $TiO_2$ Loaded on Bentonite for Enhanced Photocatalytic Activity under UV-Vis Light, J. Nanomater. 2016 (2016) 11. https://doi.org/10.1155/2016/8182190.

[130] Z. Huang, P. Wu, B. Gong, X. Zhang, Z. Liao, P.C. Chiang, X. Hu, L. Cui, Immobilization of visible light-sensitive (N,Cu) co-doped $TiO_2$ onto rectorite for photocatalytic degradation of p-chlorophenol in aqueous solution, Appl. Clay Sci. 142 (2017) 128–135. https://doi.org/10.1016/j.clay.2016.10.010.

[131] F. Zhou, H. Wang, S. Zhou, Y. Liu, C. Yan, Fabrication of europium-nitrogen co-doped $TiO_2$/Sepiolite nanocomposites and its improved photocatalytic activity in real wastewater treatment, Appl. Clay Sci. 197 (2020) 105791. https://doi.org/10.1016/j.clay.2020.105791.

[132] P. Yao, S. Zhong, Z. Shen, $TiO_2$/Halloysite Composites Codoped with Carbon and Nitrogen from Melamine and Their Enhanced Solar-Light-Driven Photocatalytic Performance, Int. J. Photoenergy. 2015 (2015), Article ID 605690, http://dx.doi.org/10.1155/2015/605690

[133] G. Zhang, X. Ding, Y. Hu, B. Huang, X. Zhang, X. Qin, J. Zhou, J. Xie, Photocatalytic degradation of 4BS dye by N,S-codoped $TiO_2$ pillared montmorillonite photocatalysts under visible-light irradiation, J. Phys. Chem. C. 112 (2008) 17994–17997. https://doi.org/10.1021/jp803939z.

[134] J. Hsing, Y. Kameshima, S. Nishimoto, M. Miyake, Preparation of carbon-modified N–$TiO_2$/montmorillonite composite with high photocatalytic activity under visible light radiation, J. Ceram. Soc. Japan. 126 (2018) 230–235. https://doi:10.3390/catal9080680.

[135] C. Belver, M. Hinojosa, J.B. Id, M.A. Alvarez, V. Rodr, J.J. Rodriguez, Montmorillonite as Solar Photocatalysts, Materials (2017) 10 960. https://doi.org/10.3390/ma10080960.

[136] S. Kaufhold, R. Dohrmann, K. Ufer, F.M. Meyer, Comparison of methods for the quantification of montmorillonite in bentonites, Appl. Clay Sci. 22 (2002) 145–151. https://doi.org/10.1016/S0169-1317(02)00131-X.

[137] J. Baloyi, T. Ntho, J. Moma, Synthesis of highly active and stable Al/Zr pillared clay as catalyst for catalytic wet oxidation of phenol, J. Porous Mater. 26 (2019) 583–597. https://doi.org/10.1007/s10934-018-0667-3.

[138] T.J. Pinnavaia, Intercalated clay catalysts, Science 220 (4595) (1983) 365–371.

[139] G. Besson, A. Mifsud, C. Tchoubar, J. Mering, Order and disorder relations in the distribution of the substitutions in smectites, illites and vermiculites, Clays and Clay Miner. 22 (1974) 379–384.

[140] H. Yi, F. Jia, Y. Zhao, W. Wang, S. Song, H. Li, C. Liu, Surface wettability of montmorillonite (0 0 1) surface as affected by surface charge and exchangeable cations: A molecular dynamic study, Appl. Surf. Sci. 459 (2018) 148–154. https://doi.org/10.1016/j.apsusc.2018.07.216.

[141] T.T. Zhu, H.C. Zhou, B.F. Kabwe, Q.Q. Wu, S.C. Li, J.R. Zhang, Exfoliation of montmorillonite and related properties of clay/polymer nanocomposites, Appl. Clay Sci. 169 (2019) 48–66. https://doi.org/10.1016/j.clay.2018.12.006.

[142] V.V. Krupskaya, S.V. Zakusin, E.A. Tyupina, O.V. Dorzhieva, A.P. Zhukhlistov, P.E. Belousov, M.N. Timofeeva, Experimental Study of Montmorillonite Structure and Transformation of Its Properties under Treatment with Inorganic Acid Solutions, Minerals. 7 (2017) 1–15. https://doi.org/10.3390/min7040049.

[143] D. Ali, G.M. Hosein, Photocatalytic Degradation of Kermanshah Refinery Wastewater, World Appl. Sci. J. 19 (2012) 874–879. https://doi.org/10.5829/idosi.wasj.2012.19.06.1644.

[144] A. Mishra, M. Sharma, A. Mehta, S. Basu, Microwave treated bentonite clay-based $TiO_2$ composites: An efficient photocatalyst for rapid degradation of methylene blue, J. Nanosci. Nanotechnol. 17 (2017) 1149–1155. https://doi.org/10.1166/jnn.2017.12674.

[145] C.B. Molina, E. Sanz-Santos, A. Boukhemkhem, B. Jorge, C. Belver, J.J. Rodriguez, Removal of emerging pollutants in aqueous phase by heterogeneous Fenton and photo-Fenton with $Fe_2O_3$-$TiO_2$-clay heterostructures, Environ. Sci. Pollut. Res. 27 (2020) 38434–38445. https://doi.org/doi.org/10.1007/s11356-020-09236-8.

[146] X. Cao, S. Luo, C. Liu, J. Chen, Synthesis of Bentonite-Supported $Fe_2O_3$-Doped $TiO_2$

superstructures for highly promoted photocatalytic activity and recyclability, Adv. Powder Technol. 28 (2017) 993–999. https://doi.org/10.1016/j.apt.2017.01.003.

[147] Y. Cao, G. Zhou, R. Zhou, C. Wang, B. Chi, Y. Wang, C. Hua, J. Qiu, Y. Jin, S. Wu, Green synthesis of reusable multifunctional γ-Fe2O3/bentonite modified by doped $TiO_2$ hollow spherical nanocomposite for removal of BPA, Sci. Total Environ. 708 (2020) 134669. https://doi.org/10.1016/j.scitotenv.2019.134669.

[148] S. Ahmad, A. Yasin, Photocatalytic degradation of deltamethrin by using Cu/$TiO_2$/bentonite composite, Arab. J. Chem. 13 (2020) 8481–8488. https://doi.org/10.1016/j.arabjc.2020.07.019.

[149] D. Bang, T. Dieu, C. Nguyen, T. Phuong, H. Thuan, Preparation, characterization, and evaluation of catalytic activity of titania modified with silver and bentonite, J. Ind. Eng. Chem. 18 (2012) 1764–1767. https://doi.org/10.1016/j.jiec.2012.04.004.

[150] A. Mishra, A. Mehta, S. Kainth, S. Basu, Effect of different plasmonic metals on photocatalytic degradation of volatile organic compounds (VOCs) by bentonite/M-$TiO_2$ nanocomposites under UV/visible light, Appl. Clay Sci. 153 (2018) 144–153. https://doi.org/10.1016/j.clay.2017.11.040.

[151] A. Mishra, A. Mehta, S. Kainth, S. Basu, Effect of g-$C_3N_4$ loading on $TiO_2$/Bentonite nanocomposites for efficient heterogeneous photocatalytic degradation of industrial dye under visible light, J. Alloys Compd. 764 (2018) 406–415. https://doi.org/10.1016/j.jallcom.2018.06.089.

[152] A. Mishra, A. Mehta, S. Kainth, S. Basu, A comparative study on the effect of different precursors for synthesis and efficient photocatalytic activity of g-$C_3N_4$/$TiO_2$/bentonite nanocomposites, J. Mater. Sci. 53 (2018) 13126–13142. https://doi.org/10.1007/s10853-018-2565-0.

[153] Y. Liu, L. Wang, N. Xue, P. Wang, M. Pei, W. Guo, Ultra-Highly Efficient Removal of Methylene Blue, Materials (Basel). 13 (2020) 1–16. https://doi:10.3390/ma13040824.

[154] L. Surya, Sheilatina, P.V. Praja, N.S. Sepia, Preparation and characterization of titania/bentonite composite application on the degradation of naphthol blue-black dye, Res. J. Chem. Environ. 22 (2018) 48–53.

[155] R. Djellabi, M.F. Ghorab, A. Smara, C.L. Biancha, G. Cerrato, X. Zhao, B. Yang, Titania – Montmorillonite for the Photocatalytic Removal of Contaminants from Water: Adsorb & Shuttle Process, Green Mater. Wastewater Treat. (2020) 291–319. https://doi.org/10.1007/978-3-030-17724-9.

[156] A. Mishra, A. Mehta, S. Basu, Clay supported $TiO_2$ nanoparticles for photocatalytic

degradation of environmental pollutants: A review, Journal of Environmental Chemical Engineering 6 (2018) 6088–6107. https://doi.org/10.1016/j.jece.2018.09.029.

[157] A. El Gaidoumi, A. Arrahli, A. Loqman, F. Baragh, B. El Bali, A. Kherbeche, Efficient Sol-gel Nanocomposite $TiO_2$-clay in Photodegradation of Phenol: Comparison to Labe-made and Commercial Photocatalysts, Silicon. (2021). https://doi.org/10.1007/s12633-021-01275-1.

[158] A. El Gaidoumi, A. Loqman, M. Zouheir, K. Tanji, O. Mertah, A. Dra, B. El Bali, A. Kherbeche, Sol-gel fluorinated $TiO_2$–clay nanocomposite: study of fluoro-titanium interaction on the photodegradation of phenol, Res. Chem. Intermed. (2021). https://doi.org/10.1007/s11164-021-04573-w.

[159] S. V. Churakov, Ab initio study of sorption on pyrophyllite: Structure and acidity of the edge sites, J. Phys. Chem. B. 110 (2006) 4135–4146. https://doi.org/10.1021/jp053874m.

[160] S. Silvestri, E.L. Foletto, Preparation and characterization of $Fe_2O_3$/$TiO_2$/clay plates and their use as photocatalysts, Ceram. Int. 43 (2017) 14057–14062. https://doi.org/10.1016/j.ceramint.2017.07.140.

[161] S. Chkirida, N. Zari, R. Achour, H. Hassoune, A. Lachehab, R. Bouhfid, Highly synergic adsorption/photocatalytic efficiency of Alginate/Bentonite impregnated $TiO_2$ beads for wastewater treatment, J. Photochem. Photobiol. A Chem. 412 (2021) 113215. https://doi.org/10.1016/j.jphotochem.2021.113215.

[162] E. Stathatos, D. Papoulis, C.A. Aggelopoulos, D. Panagiotaras, A. Nikolopoulou, $TiO_2$/palygorskite composite nanocrystalline films prepared by surfactant templating route: Synergistic effect to the photocatalytic degradation of an azo-dye in water, J. Hazard. Mater. 211–212 (2012) 68–76. https://doi.org/10.1016/j.jhazmat.2011.11.055.

[163] A. Rapsomanikis, D. Papoulis, D. Panagiotaras, E. Kaplani, E. Stathatos, Nanocrystalline $TiO_2$ and halloysite clay mineral composite films prepared by sol-gel method: Synergistic effect and the case of silver modification to the photocatalytic degradation of basic blue- 41 azo dye in water, Glob. Nest J. 16 (2014) 485–498. https://doi.org/10.30955/gnj.001323.

[164] N.N. Bahrudin, M.A. Nawi, Mechanistic of photocatalytic decolorization and mineralization of methyl orange dye by immobilized $TiO_2$/chitosan-montmorillonite, J. Water Process Eng. 31 (2019) 100843. https://doi.org/10.1016/j.jwpe.2019.100843.

[165] J. Ma, Y. Jia, Y. Jing, Y. Yao, J. Sun, Synthesis and photocatalytic activity of $TiO_2$-hectorite layer-by-layer thin films, Appl. Clay Sci. 47 (2010) 433–437.

https://doi.org/10.1016/j.clay.2009.12.020.

[166] G. Zeng, Y. He, Z. Yu, Y. Zhan, L. Ma, L. Zhang, Preparation and characterization of a novel PVDF ultrafiltration membrane by blending with $TiO_2$-HNTs nanocomposites, Appl. Surf. Sci. 371 (2016) 624–632. https://doi.org/10.1016/j.apsusc.2016.02.211.

[167] G. Mishra, M. Mukhopadhyay, $TiO_2$ decorated functionalized halloysite nanotubes ($TiO_2$@HNTs) and photocatalytic PVC membranes synthesis, characterization, and its application in water treatment, Sci. Rep. 9 (2019) 1–17. https://doi.org/10.1038/s41598-019-40775-4.

[168] M. Salimi, V. Pirouzfar, Preparation and characterization of a novel MMMs by comprising of PSF–HNT/$TiO_2$ nanotubes to reduce organic sediments, Polym. Bull. 75 (2018) 2285–2299. https://doi.org/10.1007/s00289-017-2145-5.

[169] C. Li, L. Yan, Y. Li, D. Zhang, M. Bao, L. Dong, $TiO_2$@palygorskite composite for the efficient remediation of oil spills via a dispersion-photodegradation synergy, Front. Environ. Sci. Eng. 15 (2021) 72.

[170] J. Wu, Y. He, L. Zhou, X. Yin, L. Zhang, J. Chen, Z. Li, Y. Bai, $TiO_2$@HNTs Robustly Decorated PVDF Membrane Prepared by a Bioinspired Accurate-Deposition Strategy for Complex Corrosive Wastewater Treatment, ACS Appl. Mater. Interfaces. 13 (2021) 11320–11331. https://doi.org/10.1021/acsami.1c00697.

[171] A. Sraw, T. Kaur, Y. Pandey, A. Sobti, R.K. Wanchoo, A.P. Toor, Fixed bed recirculation type photocatalytic reactor with $TiO_2$ immobilized clay beads for the degradation of pesticide polluted water, J. Environ. Chem. Eng. 6 (2018) 7035–7043. https://doi.org/10.1016/j.jece.2018.10.062.

[172] A. Moslehyani, A.F. Ismail, M.H.D. Othman, T. Matsuura, Hydrocarbon degradation and separation of bilge water via a novel $TiO_2$-HNTs/PVDF-based photocatalytic membrane reactor (PMR), RSC Adv. 5 (2015) 14147–14155. https://doi.org/10.1039/c4ra14172e.

[173] L.C.R. Machado, C.B. Torchia, R.M. Lago, Floating photocatalysts based on $TiO_2$ supported on high surface area exfoliated vermiculite for water decontamination, Catal. Commun. 7 (2006) 538–541. https://doi.org/10.1016/j.catcom.2005.10.020.

[174] S. Yoda, Y. Sakurai, A. Endo, T. Miyata, K. Otake, $TiO_2$–montmorillonite composites via supercritical intercalation, Chem. commun. 1 (2002) 1526–1527.

[175] R. Liu, Z. Ji, J. Wang, J. Zhang, Solvothermal fabrication of $TiO_2$/sepiolite composite gel with exposed {0 0 1} and {1 0 1} facets and its enhanced photocatalytic activity, Appl. Surf. Sci. 441 (2018) 29–39. https://doi.org/10.1016/j.apsusc.2018.01.309.

[176] S. Yoda, Y. Sakurai, A. Endo, T. Miyata, Synthesis of titania-pillared montmorillonite via intercalation of titanium alkoxide dissolved in supercritical carbon dioxide, J. Mater. Chem. 14 (2004) 2763–2767.

[177] E. Dvininov, E. Popovici, R. Pode, L. Cocheci, P. Barvinschi, V. Nica, Synthesis and characterization of $TiO_2$-pillared Romanian clay and their application for azoic dyes photodegradation, J. Hazard. Mater. 167 (2009) 1050–1056. https://doi.org/10.1016/j.jhazmat.2009.01.105.

[178] L. Yuan, D. Huang, W. Guo, Q. Yang, J. Yu, $TiO_2$/montmorillonite nanocomposite for removal of organic pollutant, Appl. Clay Sci. 53 (2011) 272–278. https://doi.org/10.1016/j.clay.2011.03.013.

[179] D. Chen, H. Zhu, X. Wang, A facile method to synthesize the photocatalytic $TiO_2$/montmorillonite nanocomposites with enhanced photoactivity, Appl. Surf. Sci. 319 (2014) 158–166. https://doi.org/10.1016/j.apsusc.2014.05.085.

[180] T. Zhang, Y. Luo, B. Jia, Y. Li, L. Yuan, J. Yu, Immobilization of self-assembled pre-dispersed nano-TiO2 onto montmorillonite and its photocatalytic activity, J. Environ. Sci. (China). 32 (2015) 108–117. https://doi.org/10.1016/j.jes.2015.01.010.

[181] K. Bahranowski, A. Gaweł, A. Klimek, A. Michalik-Zym, B.D. Napruszewska, M. Nattich-Rak, M. Rogowska, E.M. Serwicka, Influence of purification method of Na-montmorillonite on textural properties of clay mineral composites with $TiO_2$ nanoparticles, Appl. Clay Sci. 140 (2017) 75–80. https://doi.org/10.1016/j.clay.2017.01.032.

[182] D. Chen, Q. Zhu, F. Zhou, X. Deng, F. Li, Synthesis and photocatalytic performances of the $TiO_2$ pillared montmorillonite, J. Hazard. Mater. 235–236 (2012) 186–193. https://doi.org/10.1016/j.jhazmat.2012.07.038.

[183] C. Wang, J. Yu, J. Xing, H. Liu, Structure and properties of polymer modified $TiO_2$ pillared montmorillonite, Front. Chem. China. 3 (2008) 309–313. https://doi.org/10.1007/s11458-008-0051-y.

[184] H. Zhao, F. Qiu, J. Yan, J. Wang, X. Li, D. Yang, Preparation of economical and environmentally friendly graphene/palygorskite/$TiO_2$ composites and its application for the removal of methylene blue, Appl. Clay Sci. 121–122 (2016) 137–145. https://doi.org/10.1016/j.clay.2015.12.009.

[185] L. Wang, X. Wang, S. Cui, X. Fan, B. Zu, C. Wang, $TiO_2$ supported on silica nanolayers derived from vermiculite for efficient photocatalysis, Catal. Today. 216 (2013) 95–103. https://doi.org/10.1016/j.cattod.2013.06.026.

[186] L. Djouadi, H. Khalaf, H. Boukhatem, H. Boutoumi, A. Kezzime, J.A. Santaballa, M. Canle, Degradation of aqueous ketoprofen by heterogeneous photocatalysis using $Bi_2S_3/TiO_2$–Montmorillonite nanocomposites under simulated solar irradiation, Appl. Clay Sci. 166 (2018) 27–37. https://doi.org/10.1016/j.clay.2018.09.008.

[187] C. Ooka, S. Akita, Y. Ohashi, T. Horiuchi, K. Suzuki, S.I. Komai, H. Yoshida, T. Hattori, Crystallization of hydrothermally treated $TiO_2$ pillars in pillared montmorillonite for improvement of the photocatalytic activity, J. Mater. Chem. 9 (1999) 2943–2952.

[188] M.F. Butman, N.L. Ovchinnikov, N.S. Karasev, N.E. Kochkina, A. V. Agafonov, A. V. Vinogradov, Photocatalytic and adsorption properties of $TiO_2$-pillared montmorillonite obtained by hydrothermally activated intercalation of titanium polyhydroxo complexes, Beilstein J. Nanotechnol. 9 (2018) 364–378. https://doi.org/10.3762/bjnano.9.36.

[189] N. Jagtap, V. Ramaswamy, Oxidation of aniline over titania pillared montmorillonite clays, Appl. Clay Sci. 33 (2006) 89–98. https://doi.org/10.1016/j.clay.2006.04.001.

[190] C. Li, Z. Sun, X. Dong, S. Zheng, D.D. Dionysiou, Acetic acid-functionalized $TiO_2$/kaolinite composite photocatalysts with enhanced photocatalytic performance through regulating interfacial charge transfer, J. Catal. 367 (2018) 126–138. https://doi.org/10.1016/j.jcat.2018.09.001.

[191] A.-M. Al-Munawwarah, I. Fatimah, P.R. Shukla, F. Kooli, B. Yogyakarta, Combined photocatalytic and Fenton oxidation of methyl orange dye using iron exchanged titanium pillared montmorillonite, J. Appl. Sci. 9 (2009) 3715–3722. https://doi.org/10.3923/jas.2009.3715.3722.

[192] I. Fatimah, I. Sumarlan, T. Alawiyah, Fe(III)/$TiO_2$-Montmorillonite Photocatalyst in Photo-Fenton-Like Degradation of Methylene Blue, Int. J. Chem. Eng. (2015), Article ID 485463, https://doi.org/10.1155/2015/485463.

[193] Q. Wang, Y. Cui, R. Huang, L. Zhong, P. Yan, S. Zhang, A heterogeneous Fenton reaction system of N-doped $TiO_2$ anchored on sepiolite activates peroxymonosulfate under visible light irradiation, Chem. Eng. J. 383 (2020) 123142. https://doi.org/10.1016/j.cej.2019.123142.

# Chapter 3: Synthesis and characterization of A-$TiO_2$-BiOBr-Bt heterostructures and analytical methods used in testing their photocatalytic activity

## 3.0. Introduction

This is the third chapter of the dissertation which describes the materials used in the synthesis and application of the heterostructures in the photocatalysis of phenol, the solvothermal method used in the fabrication of A-$TiO_2$-BiOBr-Bt heterostructures, and the characterization techniques used to investigate the properties of the heterostructures. It further discusses the photocatalysis of phenol on the heterostructures under visible light irradiation and the HPLC method used to determine the initial and residual concentration of phenol.

## 3.1. Materials

Raw Bt with a Cation Exchange Capacity (CEC) of 78 meq/100 g of clay was purchased from ECCA Holdings (Pty) Ltd, Cape Town, South Africa. $Bi(NO_3)_3 \cdot 5H_2O$, KBr, tetrabutyl titanate (TBOT) (97%), methanol (HPLC grade), ethylene glycol (EG), ethanol (EtOH), phenol, $HNO_3$ (37%), NaOH, $AgNO_3$, ammonium oxalate (AO), Isopropanol (IPA), and benzoquinone (BQ) were all purchased from Sigma Aldrich. All the reagents were used without further purification or modification. All water-based solutions were prepared using millipore water with a resistivity of 18 MΩcm.

## 3.2. Synthesis

The heterostructures were fabricated using a solvothermal process previously reported by Hu et al. [1]. In each of the heterostructures, the mass ratio of photoactive materials (A-$TiO_2$ and BiOBr) to Bt was kept at 1:1. Typically, a specific amount of $Bi(NO_3)_3 \cdot 5H_2O$ was dissolved into a mixture of 20 mL EG and 30 mL EtOH in a three-necked round bottom flask at room temperature by ultrasonication. Thereafter, 2.0 g of bentonite was added into the mixture to form a slurry (slurry A) which was stirred for 20 min using a magnetic stirrer. A corresponding specific amount of KBr was dissolved into 20 mL of EG in a 100 mL beaker to form a clear solution (solution B) such that the number of moles of $Br^-$ in solution B was slightly more than

those of $Bi^{3+}$ in slurry A. Solution B was added dropwise into slurry A to form a homogeneous slurry (slurry C) which was further stirred for 30 min.

TBOT was added dropwise into slurry C and the mixture was magnetically stirred for 1 h. The mixture was then transferred into a Teflon-lined autoclave and heated to 160 °C at 1 °C/min. The reaction was allowed to continue for 18 h, thereafter left to cool naturally, and then transferred into a 100 mL beaker. The collected products were centrifuged, washed with EtOH and millipore water, and then dried at 80 °C for 24 h. The $TiO_2$:BiOBr:Bt mass ratio was fixed at 3:1:4, 1:1:2, and 1:3:4 in the ternary composites. After drying, the A-$TiO_2$-BiOBr-Bt powders were ground using mortar and pestle and labeled as $Ti_xBi_yBt_z$ where x, y, and z are the mass proportions for A-$TiO_2$, BiOBr, and Bt in each composite. A simple representation of the synthesis scheme of the ternary composites is shown in **Figure 3.1**. The amounts of TBOT, $Bi(NO_3)_3 \cdot 5H_2O$, and KBr used in fabricating the ternary composites are shown in **Table 3.1**.

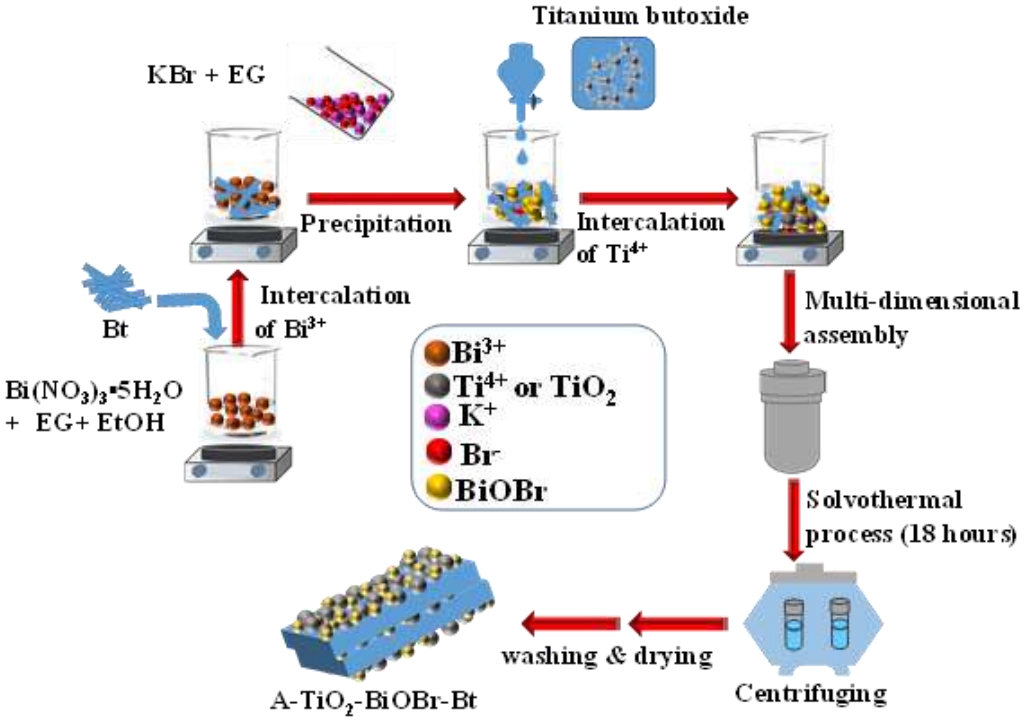



**Figure 3.1.** Synthesis scheme for A-$TiO_2$-BiOBr-Bt heterostructures.

**Table 3.1. Amounts of TBOT, $Bi(NO_3)_3 \cdot 5H_2O$, and KBr that were used in the fabrication of the ternary composites.**

| Sample | Mass (g) | | |
|---|---|---|---|
| | **TBOT** | $Bi(NO_3)_3 \cdot 5H_2O$ | **KBr** |
| $Ti_3Bi_1Bt_4$ | 6.39 | 0.80 | 0.23 |

| | | | |
|---|---|---|---|
| $Ti_1Bi_1Bt_2$ | 4.26 | 1.59 | 0.47 |
| $Ti_1Bi_3Bt_4$ | 2.14 | 2.38 | 0.70 |

## 3.3. Characterization

Powder X-Ray Diffraction (PXRD) analyses for the materials were carried out using a Bruker D2 Phaser fitted with a LynxEye detector which uses Cu K-α irradiation (λ=1.54 Å) operating at 30 kV/30 mA over a $5\ ^\circ \leq 2\theta \leq 90\ ^\circ$ range.

SEM analyses were performed using a ZEISS SIGMA 03–39 FESEM. The FESEM microscope was equipped with an Energy Dispersive X-ray detector to perform elemental analysis. Before taking the micrographs, the powders were sputtered on a carbon tape which was mounted on an aluminum pin stub and then coated with a single layer of carbon and a single layer of gold-palladium. For TEM analysis, each material was dispersed in toluene and then loaded onto lacey carbon copper grids through drop-casting and allowed to dry. The samples were then analyzed on a Tecnai Spirit T12 microscope at 120 kV.

XPS analyses were performed on Physical Electronics Quantum 2000, using a monochromatic Al Kα source operating at 1486.7 eV. Textural information was probed through $N_2$ adsorption-desorption at a constant temperature of -195 °C and lowest pressure using a Micromeritics Tristar 3000 (RS232) surface area and porosity analyzer after purging the samples under $N_2$ for 12 h. UV-Vis Spectroscopy measurements were collected using a UV-Vis spectrophotometer UV-2600i from Shimadzu. Photoluminescence (PL) measurements were acquired using a HORIBA Scientific QM-8075-22-C spectrophotometer in the 370-650 nm range and the materials were excited at 340 nm.

The surface charge properties of the Bt and the different photocatalysts were investigated by determining their point of zero charge ($pH_{PZC}$) using the pH drift test previously reported by Gatabi et al. [2]. The initial and final pH of the solutions were recorded using a freshly calibrated Tinsmark pH meter (Benchtop pH/mV/ORP Meter IS/139E IS-139E Conductivity Touchscreen #rs). The pH drift experiments were done in triplicates and the average was presented.

The thermal stability of the materials was analyzed using the Perkin Elmer TGA 6000 thermogravimetric analyzer. Approximately 10 mg of sample was first purged under $N_2$ at 150 °C at a 20 mL/min flow rate. After purging, the materials were heated under high purity $N_2$ at a 10 °C/min rate from 35 °C to 900 °C and the $N_2$ flow rate was fixed at 10 mL/min.

## 3.4. Photodegradation experiments

Phenol was used as a model pollutant in evaluating the photocatalytic performance of the heterostructures. The photocatalytic tests were carried out in a 1000 mL photochemical reactor supplied by Lelesil Innovative systems whose design is shown in **Figure 3.2** equipped with a 250 W Vis lamp. The reaction time was 80 min and the volume of phenol solution in the reactor was fixed at 100 mL for all the photocatalytic experiments. The initial pH of the phenol solutions was adjusted accordingly using 0.1 M $HNO_3$ and 0.1 M NaOH solutions. The temperature of the reaction medium was kept at 25 °C through circulating water from the chiller into the immersion chamber and back to the chiller. In a typical photocatalysis experiment, a specific amount of photocatalyst was suspended into the phenol solution with a specific initial concentration and the mixture was magnetically stirred in the dark for 60 min to achieve adsorption/desorption equilibrium between the photocatalysts and phenol molecules [3]. After that, the phenol-catalyst mixture was irradiated using a 250 W Vis lamp fitted in the immersion chamber. A syringe fitted with a 0.45 µm disposable syringe filter was used to withdraw 1.5 mL aliquots at 10 min intervals for 80 min. All the photocatalytic experiments were done in triplicates and the average phenol concentration for each specific catalytic run was reported accordingly.

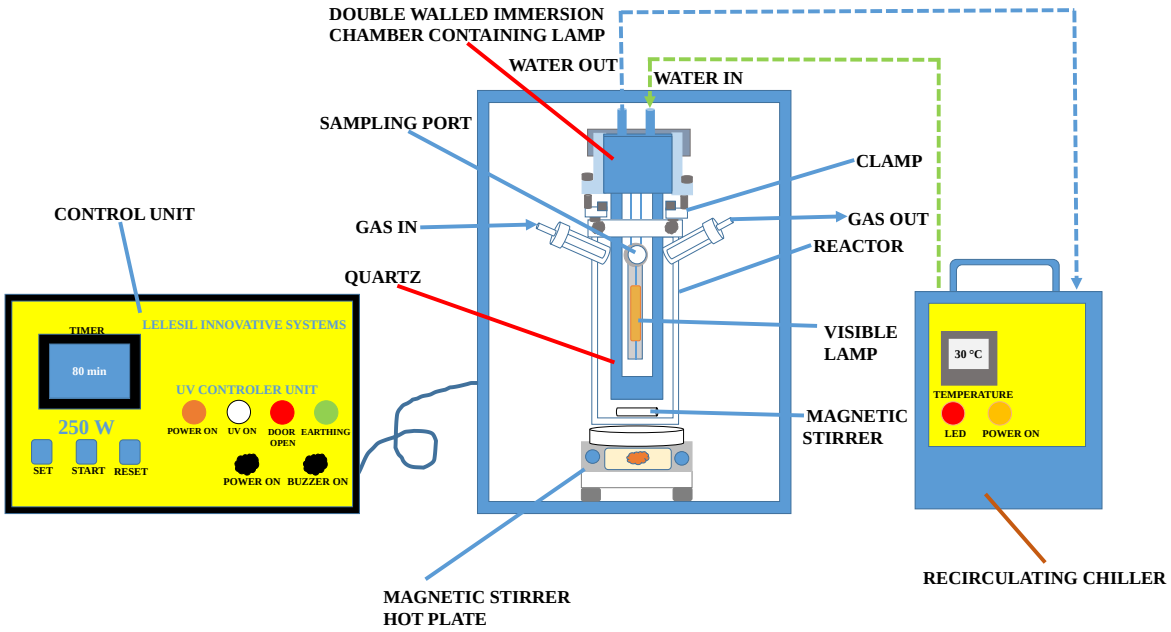



**Figure 3.2.** Design of the Lelesil photochemical reactor system used.

After selecting the most photoactive photocatalyst, several operational conditions such as initial solution pH, photocatalyst dosage, and initial concentration were optimized for

effective phenol photocatalysis. The tested conditions during optimization studies are presented in **Table 3.2.**

**Table 3.2. Operational conditions optimized for effective phenol photocatalysis.**

| Operational condition | Quantities |
|---|---|
| Initial solution pH | pH 4, 6, 7, 8, and 10 |
| Photocatalyst dosage | 50, 100, 150, and 200 mg |
| Initial phenol concentration | 10, 20, 30, 50, and 100 ppm |

## 3.5. Analytical methods

The concentration of residual phenol was monitored at room temperature using a BISCHOFF HPLC instrument equipped with a UV detector and the absorbance wavelength was set at 254 nm. An Agilent Eclipse XDB C18 column (150 mm x 4.6 mm, 3.5 µm) was used and the injection volume was fixed at 20 µL. An isocratic eluent consisting of a methanol/water (60:40, v/v) mixture was used as a mobile phase. The elution process was performed within 4 min, and the flow rate was set at 1.0 mL/min. The phenol concentration was determined from a calibration curve resolved from external phenol standards and typical calibration standards are shown in **Figure S1**.

The efficiency $\mathrm{E}(\%)$ of the photodegradation process was calculated using **equation 3.1**;

$$\mathrm{E}(\%) = (1 - \frac{C}{C_0}) \times 100 \qquad 3.1$$

where $C$ is the concentration at time t, $C_0$ is the initial concentration at t=0.

## References

[1] X. Hu, C. Li, J. Song, S. Zheng, Z. Sun, Multidimensional assembly of oxygen vacancy-rich amorphous $TiO_2$-BiOBr-sepiolite composite for rapid elimination of formaldehyde and oxytetracycline under visible light, J. Colloid Interface Sci. 574 (2020) 61–73. https://doi.org/10.1016/j.jcis.2020.04.035.

[2] M. Pashai Gatabi, H. Milani Moghaddam, M. Ghorbani, Point of zero charge of maghemite decorated multiwalled carbon nanotubes fabricated by chemical precipitation method, J. Mol. Liq. 216 (2016) 117–125. https://doi.org/10.1016/j.molliq.2015.12.087.

[3] C. Belver, J. Bedia, M.A. Álvarez-Montero, J.J. Rodriguez, Solar photocatalytic purification of water with Ce-doped $TiO_2$/clay heterostructures, Catal. Today. 266 (2016) 36–45. https://doi.org/10.1016/j.cattod.2015.09.025.

# Chapter 4: Characterization results

## 4.0. Introduction

This fourth chapter presents and discusses the characterization results of the materials used in this study. The performance of the materials in photocatalytic applications is a function of their specific physical, chemical, textural and optoelectronic properties. It is for this reason that careful characterization of the materials is principal to establish the relationship between their properties and their photocatalytic activity. The characterization techniques used to investigate the properties of the materials used in this study included PXRD, SEM, TEM, XPS, $N_2$ adsorption-desorption, UV-Vis spectroscopy, PL spectroscopy, pH drift method, and TGA.

PXRD, SEM, EDS, and TEM analyses were used to probe information about the crystallographic, morphological features, and chemical composition of the materials. The three analyses were done orderly starting from the simple starting materials, then binary composites, and finally ternary composites. Changes of specific features in the results of the starting materials (A-$TiO_2$, BiOBr, and Bt) after fabricating composites were studied. PXRD probed the crystal structure of the materials and special interest was on observing the impurities in Bt, bonding between A-$TiO_2$ and BiOBr, change in crystallinity after fabricating composites, and determining the basal spacing of the Bt-based composites using Bragg's law [1]. SEM images were collected to probe the visible surface morphological features of the different materials. EDS analyses were performed to identify the different elements within the starting materials, binary and ternary heterostructures. Elemental mapping images were collected to investigate the distribution of elements within $Ti_1Bi_1$ and $Ti_1Bi_1Bt_2$ heterostructures. This was done to provide evidence of the even distribution of BiOBr within the preponderant A-$TiO_2$ formula units and to also study the even distribution of A-$TiO_2$-BiOBr catalytic material within the Bt support. TEM analyses were done to collect images that show the intrinsic structure of the materials. Special interest was on displaying images of the starting materials and the different components of the binary and ternary composites and observing possible fringe lines on the Bt-based materials.

To study the surface composition and chemical states of $Ti_1Bi_1Bt_2$ which is the photocatalyst of interest, XPS analyses were performed and the relative XPS spectra of $Ti_1Bi_1Bt_2$ were compared to those of A-$TiO_2$, BiOBr, $Ti_1Bi_1$, and $Ti_1Bi_1Bt_2$-400. The peak positions of the binding energies in the spectra of A-$TiO_2$ and BiOBr are indicative of the chemical states of the ions present in them. Changes in the indicative peak positions of A-$TiO_2$ and BiOBr when

coupled together or/and with Bt to form the binary and ternary composites gave useful information about the chemical bonds that form.

The specific surface area was calculated using the Brunauer Emmett Teller (BET) method, the total pore volume was calculated at a relative $N_2$ pressure of $P/P_0 \sim 0.99$, and the pore size distribution was calculated using the Barrett–Joyner–Halenda (BJH) method based on the desorption branch of the isotherms. In studying the type of pore distribution curves, adsorption isotherms, and type hysteresis loops, useful information about the porosity of the materials was extracted. In the pore distribution curves pores below 2 nm are micropores, those between 2-50 nm are mesopores and those above 50 nm are macropores respectively [2].

To study the optoelectronic properties of the materials UV-Vis and PL spectroscopy was used. From UV-Vis analyses, the bandgap energies of the materials were determined using the Tauc plot method. PL analysis provided the means to qualitatively compare the electron-hole recombination rates between the different materials by comparing the intensities of their emission spectra. High intensity in the emission spectra is associated with a high electron-hole recombination rate.

Apart from other considerations like mobility, the electrostatic interaction between Bt and the different adsorbing photocatalysts and phenol is dependent on the nature of charges between them. The nature of charges on the photocatalysts under different pH values is determined by identifying the point of zero charge ($pH_{PZC}$). The $pH_{PZC}$ is the pH-dependent interfacial condition where the surface charge density of a powder or solid is null [3]. Generally, pollutants with a charge opposite to the adsorbing powder or solid are likely to be adsorbed at a higher rate to the solid due in part to the electrostatic attraction between the pollutants and the solid [4].

TGA and DTG analyses were used to determine the thermal stability of the materials. The TGA curves gave information about residual weight during thermal treatment of the materials while DTG curves gave endothermic ascribed to specific thermal degradation steps.

## 4.1. PXRD

The crystal structure of the photocatalysts was investigated using PXRD and the diffractograms are shown in **Figure 4.1**. Bt constitutes quartz as the dominant montmorillonite (Mt) impurity. In the diffraction patterns of A-$TiO_2$, there are no obvious distinct peaks, proving its amorphous

nature [5]. BiOBr is perfectly crystalline and its diffraction pattern is consistent with that of pure tetragonal BiOBr (JCPDS 09-0393) [6–8].

Among the binary clay composites, $Ti_1Bt_1$ shows only Bt peaks with suppressed intensity due to the amorphous nature of A-$TiO_2$. $Bi_1Bt_1$ has peaks ascribed to both Bt and BiOBr and the BiOBr peaks maintain high intensity. In both cases the Bt (001) peak at $2\theta = 7.40$ ° shifts to lower $2\theta$ values attributed to the intercalation of A-$TiO_2$ and BiOBr into the interlayer spacing of Bt.

Coupling A-$TiO_2$ and BiOBr give a binary heterostructure with low crystallinity shown by the broadening of some indicative BiOBr diffraction peaks such as (101), (012), (110), and (212) peaks. Moreover, BiOBr indicative peaks such as (001), (002), (112), (104), (211), and (214) become very weak or disappear because A-$TiO_2$ impedes the growth of these facets resulting in smaller BiOBr crystallites or the facet coupling between BiOBr and $TiO_2$ occurs along with these facets [6,9]. Specifically, the disappearance of the BiOBr (001) and (002) peaks with the addition of A-$TiO_2$ is ascribed to the coupling of A-$TiO_2$ on the (001) faces of BiOBr [10]. The (002) plane is not real but constitutes the second-order super positional indexes of the (001) plane [10]. Some of the $2\theta$ peak positions such as (101), (110), (200) shifted slightly due to the existence of Ti-doped BiOBr [9]. The Ti atom is about 61 pm which is significantly smaller than the Bi atom which is about 103 pm and the replacement of lattice Bi shifts the BiOBr PXRD planes [11].

In the A-$TiO_2$-BiOBr-Bt ternary heterostructures, there are peaks ascribed to both $Ti_1Bi_1$ and Bt. However, the PXRD patterns of $Ti_3Bi_1Bt_4$ and $Ti_1Bi_1Bt_2$ show well-defined shifts in the Bt (001) peak from $2\theta$=7.40 ° to lower $2\theta$ values manifesting more disruption of the Bt layered structure [12,13]. Conversely, when the $Ti_1Bi_1Bt_2$ is calcined at 400 °C, sharp peaks emerge as a result of the increase in the crystallinity of the $Ti_1Bi_1Bt_2$-400 heterostructures and this was also observed by Hu et al. [6] when fabricating A-$TiO_2$-BiOBr-Sepiolite heterostructures. Additionally, the calcination process results in the shift of the Bt (001) peak to $2\theta$ values below 5 ° as seen in **Figure 4.1** due to increased delamination.

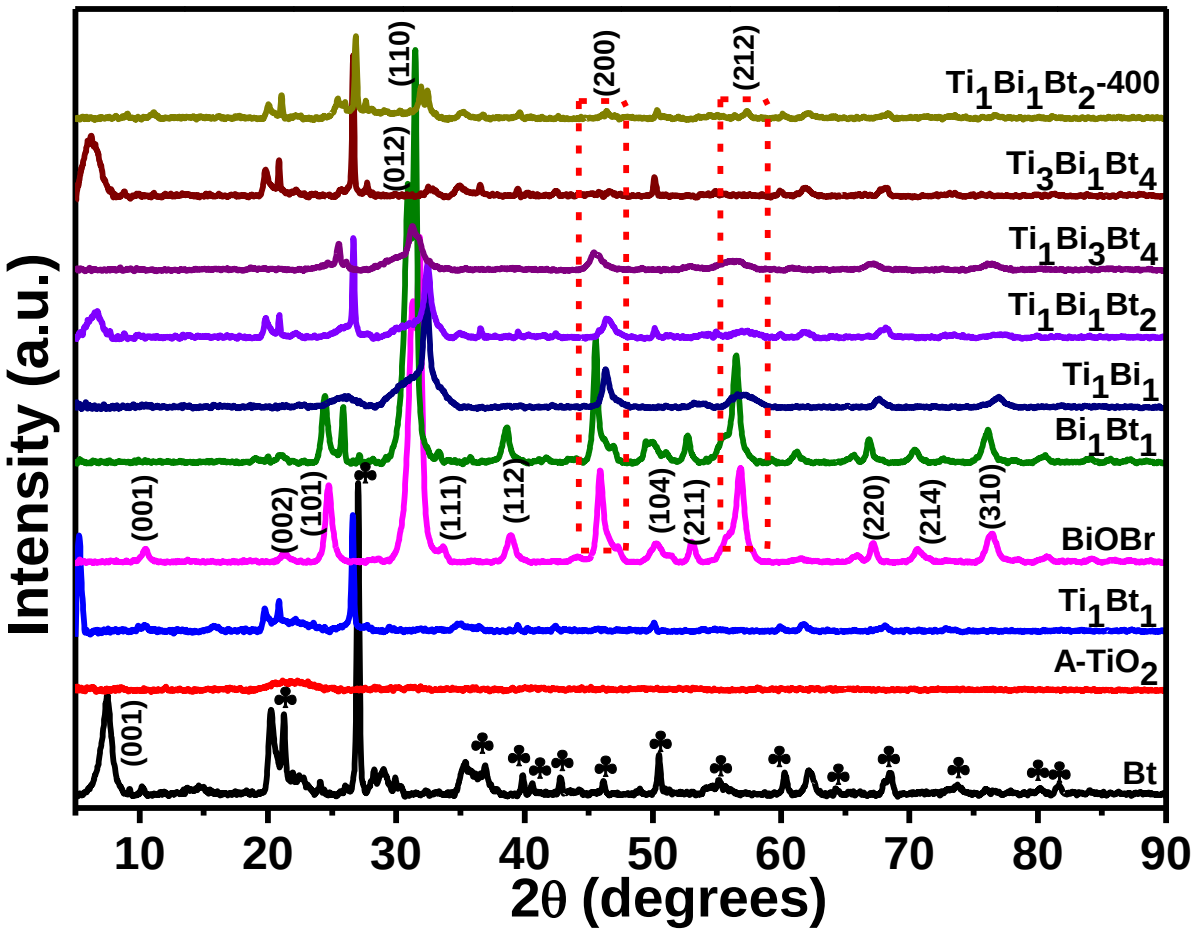



**Figure 4.1.** PXRD diffraction patterns of Bt and the different photocatalysts. The (♣) designates the quartz peaks in the Bt diffraction pattern.

Bt constitutes 75-95% Mt [14] with smaller percentages of quartz, cristobalite, feldspar, pyrite, carbonates, chlorite, kaolinite, mica, illite [15], calcite, and muscovite [16]. It constitutes layered aluminosilicate sheets where each sheet is made up of 2 tetrahedral silica layers sandwiching an octahedral alumina layer as shown in **Figure 2.13**.

The XRD profile in **Figure 2.13** shows layers of Bt separated by interlayer spaces with exchangeable cations (green balls) to balance the charge deficiencies of the surface of each aluminosilicate sheet. The combined thickness of an aluminosilicate sheet and its associated interlayer space constitute the $d_{001}$ basal spacing. To calculate the basal spacing of the Bt-based materials, Bragg's law shown in **equation 4.1** was used with the principal parameter (θ) being half the value of the Bt (001) indicative peak [1].

$$\boldsymbol{d_{001} = \frac{n\lambda}{2sin\theta}} \qquad \textbf{4.1}$$

The (001) peak of the Bt used in this study is at 2θ=7.40 °, and therefore its $d_{001}$ basal spacing is 11.9 Å. After functionalization using A-$TiO_2$ and BiOBr, a shift of the Bt (001) peak to lower 2θ values is an indicator of an increase in the basal spacing caused by the intercalation of the semiconductors in its interlamellar spacing. Functionalizing Bt with BiOBr or its mixture with A-$TiO_2$ where the BiOBr is the predominant component, the basal spacing increases significantly. This is evidenced by the shift of the Bt (001) peak to 2θ values below 5 ° in the PXRD patterns of $Bi_1Bt_1$ and $Ti_1Bi_3Bt_4$. The shift of the (001) peak to 2θ values below 5 ° suggests that the in situ growth of BiOBr is mainly in the interlayer spacing of Bt delaminating the Bt layered structure. Conversely, when Bt is functionalized with A-$TiO_2$ or its mixture with BiOBr where A-$TiO_2$ is the predominant component or equal to BiOBr, the basal spacing increases slightly such that there is a slight shift of the Bt (001) diffraction peak to lower 2θ values. This is evident in the PXRD patterns of $Ti_1Bt_1$ (5.39 °), $Ti_3Bi_1Bt_4$ (6.19 °), and $Ti_1Bi_1Bt_2$ (6.25 °). This suggests that A-$TiO_2$ preferentially forms on the surface Bt in the materials thereby causing a small increase in the basal and interlayer spacing of the resulting heterostructures. The basal spacing of $Ti_1Bt_1$, $Ti_1Bi_1Bt_2$, and $Ti_3Bi_1Bt_4$ are 16.4, 14.1, and 14.2 Å respectively, which is a small increase from that of Bt (11.9 Å).

## 4.2. SEM analyses

According to **Figure 4.2a**, Bt consists of layered, irregular platelets morphology. A-$TiO_2$ (**Figure 4.2b**) constitutes small, irregular particles that get aggregated to form large lumpy agglomerates, a structure also reported by Hu et al. [6] and Vargas et al. [17]. BiOBr (**Figure 4.2c**) consists of perfect crystals with two morphologies: spherical hierarchical microspheres formed through the growth of small plate-like sheets, and smooth microspheres made from the radial growth of fine hair-like fibers, and both morphologies were also reported by Yuan et al. [18]. With $Ti_1Bi_1$, distinct round BiOBr platelets and microspheres are coupled to the lumpy A-$TiO_2$ aggregates like round raisins in a pudding (**Figure 4.2d**), and this kind of coupling was also observed by Wei et al. [5].

For the binary Bt-based composites, there is clear contrast on the placement of A-$TiO_2$ and BiOBr particles on Bt during immobilization. A-$TiO_2$ preferentially forms its irregular agglomerates on the surface of the Bt (**Figure 4.2e**) and to some extent the immobilization of A-$TiO_2$ onto Bt averts their growth into large lumps. Evidence of the preferential surface immobilization of A-$TiO_2$ was also confirmed by low basal spacing from the PXRD analysis

in **Figure 4.1**. In contrast, BiOBr is preferentially embedded in its platelet form into the interlayer spacing of Bt such that some BiOBr platelets protrude to the Bt surface (**Figure 4.2f**).

In the ternary multidimensional heterostructures, BiOBr microspheres and A-$TiO_2$ aggregates are seen on the surfaces of Bt, especially in $Ti_1Bi_3Bt_4$, $Ti_1Bi_1Bt_2$, and $Ti_1Bi_1Bt_2$-400. The existence of BiOBr microparticles on the surfaces of $Ti_1Bi_3Bt_4$, $Ti_1Bi_1Bt_2$, and $Ti_1Bi_1Bt_2$-400 (**Figure 4.2g, h,** and **j**) is due to the existence of appreciable formula units of BiOBr per unit mass in the composites. In the case of $Ti_3Bi_1Bt_4$, there are no BiOBr particles visible on the surface (**Figure 4.2i**) because they are likely embedded in the interlayer spacing of Bt and some are completely covered in the preponderant A-$TiO_2$ agglomerates with a higher number of formula units compared to BiOBr per mass unit of the composite.

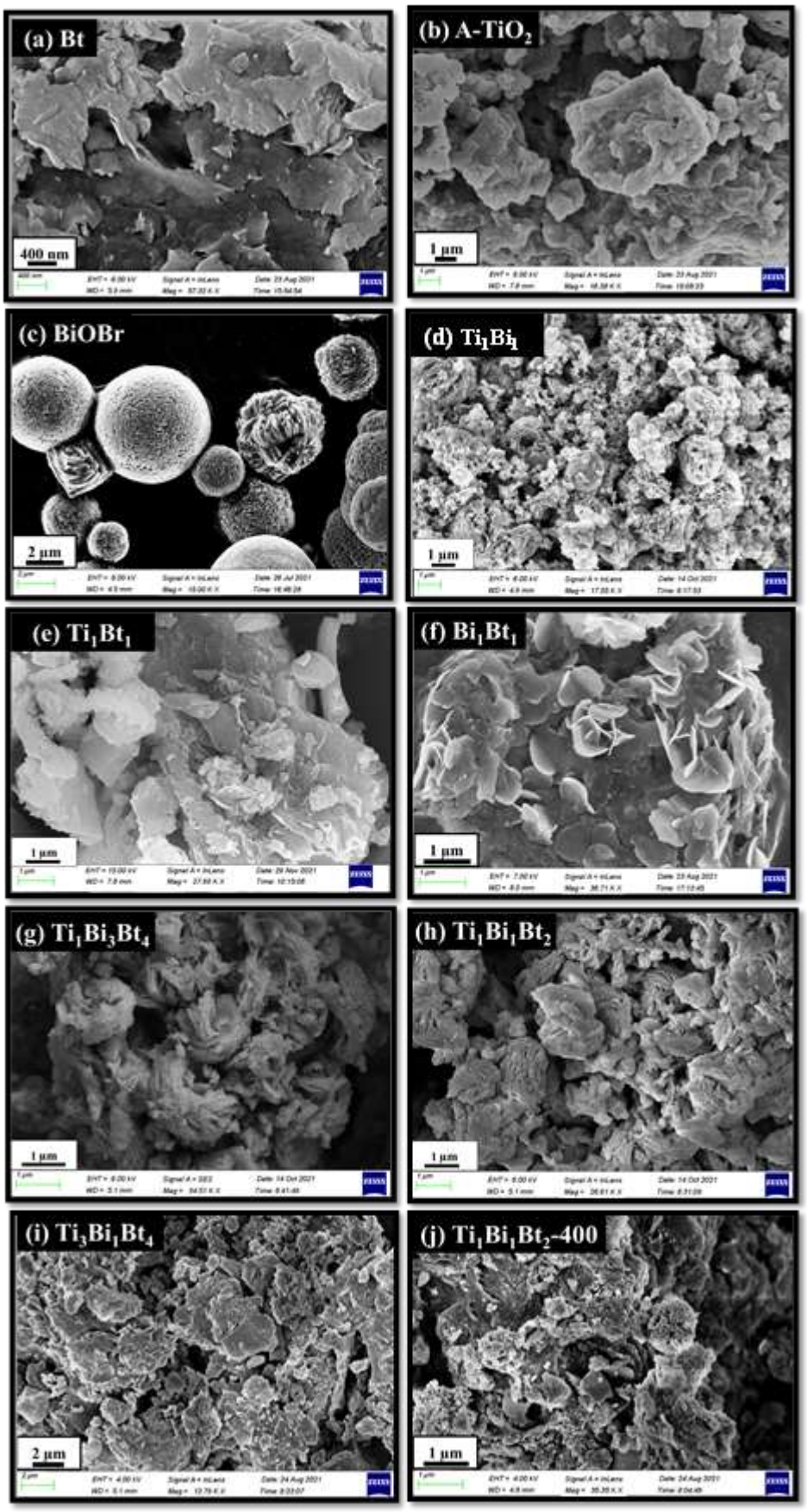



**Figure 4.2.** The SEM images of Bt and the different photocatalysts (a)-(j).

The elemental compositions of all the materials were approximated through EDS analysis and the atomic percentages of all the elements in each material are presented in **Table 4.1.** Bt contains Si, Al, O, Fe, and the exchangeable cations consisting of $Na^+$, $K^{+,}$ and $Mg^{2+}$. The analysis of the EDS results indicates that some A-$TiO_2$ and BiOBr particles are intercalated into Bt through a cation exchange process as confirmed by the existence of all the exchangeable cations ($Na^+$ and $K^+$) below the detection limits (DL) in all the Bt-based photocatalysts. The intercalation is also confirmed by the PXRD analysis based on an increase in the basal spacing of Bt. In $Ti_1Bt_1$, there is an observed presence of appreciable amounts of Ti and all the Bt elements except for Fe and the displaced $Na^+$ and $K^+$. The intercalation of BiOBr in $Bi_1Bt_1$ is confirmed by the existence of Bi, Br, and all the Bt elements except Fe, $Na^+$, and $K^+$.

In ternary heterostructures, EDS analysis identified the presence of appreciable amounts of Ti, O, Bi, Br, and all the Bt elements except for $Na^+$, $K^{+,}$ and $Fe^{3+}$ which are outside the DL as shown in **Table 4.1**. The existence of $Na^+$ and $K^+$ below the DL in all the Bt composites suggests that some A-$TiO_2$ and BiOBr replace these elements in the interlayer spacing of Bt through a cation exchange process.

**Table 4.1. Chemical analysis showing the approximate atomic % of the different elements in Bt and the different photocatalysts obtained from EDS analysis.**

| **Material** | **Atomic (%) of all the elements in each material** | | | | | | | | | |
|---|---|---|---|---|---|---|---|---|---|---|
| | **Na** | **K** | **Mg** | **Fe** | **Al** | **Si** | **Ti** | **Bi** | **O** | **Br** |
| Bt | 1.56 | 0.34 | 2.15 | 1.10 | 6.88 | 18.84 | - | - | 55.75 | - |
| A-$TiO_2$ | - | - | - | - | - | - | 24.27 | - | 75.73 | - |
| BiOBr | - | - | - | - | - | - | - | 20.19 | 61.55 | 18.25 |
| $Ti_1Bi_1$ | - | - | - | - | - | - | 14.44 | 6.56 | 73.38 | 5.62 |
| $Ti_1Bt_1$ | - | - | 0.32 | - | 0.63 | 3.47 | 19.49 | - | 76.06 | - |
| $Bi_1Bt_1$ | - | - | 1.41 | - | 2.22 | 13.14 | - | 13.16 | 58.79 | 11.27 |
| $Ti_1Bi_3Bt_4$ | - | - | 1.31 | 0.69 | 6.08 | 6.10 | 4.70 | 4.52 | 74.88 | 1.72 |
| $Ti_1Bi_1Bt_2$ | - | - | 0.60 | - | 2.57 | 14.34 | 6.86 | 2.80 | 71.56 | 1.92 |
| $Ti_3Bi_1Bt_4$ | - | - | 0.43 | - | 1.45 | 9.68 | 10.81 | 1.15 | 74.84 | 1.63 |
| $Ti_1Bi_1Bt_2$-400 °C | - | - | 1.15 | - | 3.51 | 9.80 | 8.09 | 3.27 | 73.26 | 0.92 |

To investigate the distribution of BiOBr and A-$TiO_2$ in $Ti_1Bi_1$, EDS elemental mapping images were collected and presented in **Figure 4.3.** From the mapping images, it can be seen that Ti, Bi, O, and Br are evenly distributed due to the uniform composition of the $Ti_1Bi_1$ architecture.

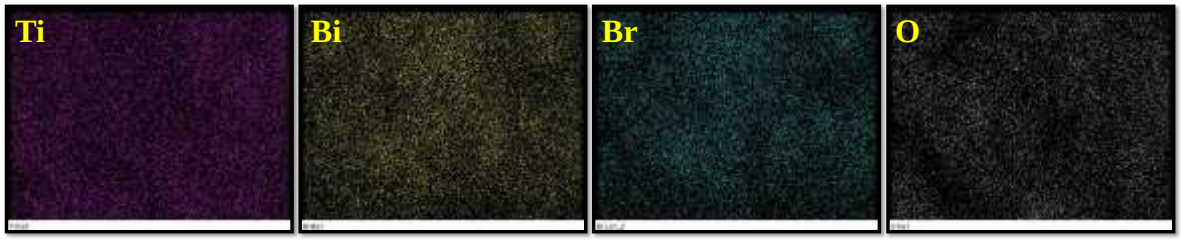



**Figure 4.3.** EDS elemental mapping images of $Ti_1Bi_1$.

The EDS mapping images also confirmed the uniformity in the dispersion of A-$TiO_2$ and BiOBr in $Ti_1Bi_1Bt_2$ (**Figure 4.4**), which is the photocatalyst of interest. The even dispersion of Ti, Bi, and Br in the $Ti_1Bi_1Bt_2$ ternary matrix is further evidence of the existence of A-$TiO_2$ and BiOBr on the surface and also in the interlayer spacing of Bt. If A-$TiO_2$ and BiOBr were not intercalated into the interlayer spacing of Bt, fringe lines in the mapping images indicating the absence of Ti, Bi, and Br could be observed.

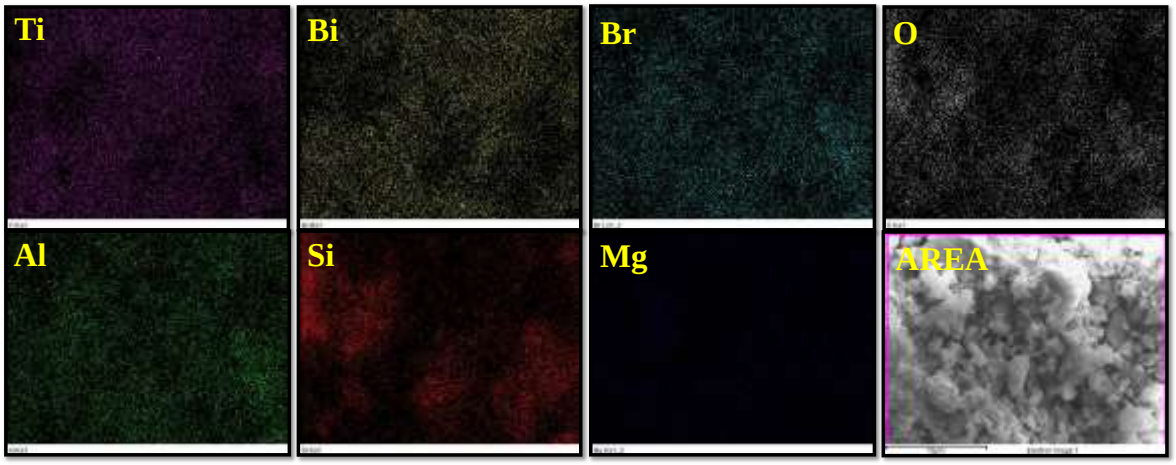



**Figure 4.4.** Elemental mapping images of $Ti_1Bi_1Bt_2$ and the area selected for the analysis.

## 4.3. TEM analysis

TEM was used to probe the directly resolved intrinsic structure of the materials, and the micrographs of Bt and the various photocatalysts are presented in **Figure 4.5**. Bsed on **Figure 4.5a** image, Bt consists of a compact structure attributed to stacked aluminosilicate platelets with low basal spacing. However, there is evidence of delaminated clay platelets in some regions which is a typical form of disorder in clay structures. A-$TiO_2$ (**Figure 4.5b**) exhibits a

lumpy structure akin to the one reported by Zywitzki et al. [19] for A-$TiO_2$ support used to load Pt. The BiOBr in **Figure 4.5c** exists as microspheres which is consistent with SEM analysis, and this structure is widely reported. In $Ti_1Bi_1$ (**Figure 4.5d**), the BiOBr particles are immobilized on A-$TiO_2$ such that the A-$TiO_2$ aggregates bind BiOBr particles.

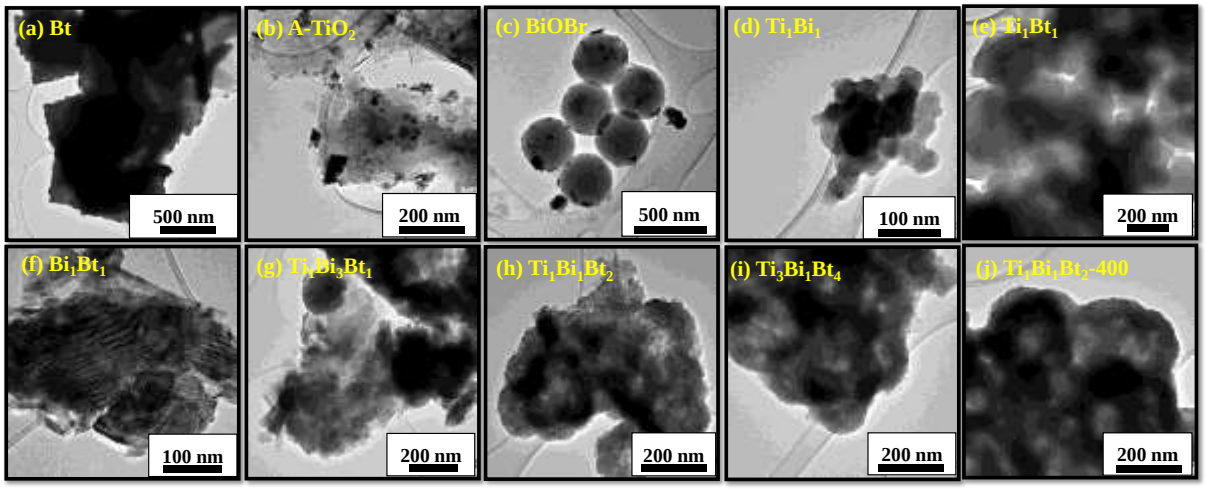



**Figure 4.5.** TEM images of Bt and the different photocatalysts.

The image in **Figure 4.5e** shows evidence of A-$TiO_2$ agglomerates forming a coat on the surface of Bt in $Ti_1Bt_1$. However, the image of $Bi_1Bt_1$ (**Figure 4.5f**) shows fringe lines in Bt suggesting appreciable intercalation of BiOBr into the interlayer spacing of Bt. The preferential growth of A-$TiO_2$ on the Bt surface and BiOBr in the interlayer is in agreement with PXRD and SEM analyses. However, the different componets are widely dispersed within the structural frameworks of ternary A-$TiO_2$-BiOBr-Bt multidimensional heterostructures (**Figure 4.5g-j**).

## 4.4. XPS

The survey XPS spectrum of $Ti_1Bi_1Bt_2$ and $Ti_1Bi_1Bt_2$-400 confirms that their elemental composition constitutes of Mg, Al, Si, Ti, Bi, O, Br, and C on their surfaces as shown in **Figure 4.6a** and **4.6b** which is in agreement with the EDS results in **Table 4.1**. The carbon peak is due to residual carbon from TBOT, ethanol, and ethylene glycol. The presence of adsorbed adventitious carbon from the atmosphere onto the sample is also suspected [5].

In the Br 3d spectra of $Ti_1Bi_1Bt_2$ shown in **Figure 4.6c**, the Br 3d peak in the 66-70 eV range was resolved into two peaks centered at 67.71 eV and 68.72 eV ascribed to Br $3d_{5/2}$ and Br $3d_{3/2}$ respectively confirming the existence of $Br^{-1}$ instead of zero-valent Br [6].

The Bi 4f spectra of BiOBr and $Ti_1Bi_1$ (**Figure 4.6d**) were resolved into two peaks centered at around 158 and 164.0 eV ascribed to Bi $4f_{7/2}$ and Bi $4f_{5/2}$ for each sample proving the presence of bismuth in its $Bi^{3+}$ form instead of its zerovalent form [5,6]. $Ti_1Bi_1Bt_2$ has an additional low-intensity peak at 156.55 eV. However, there are obvious binding energy offsets in the Bi 4f spectra associated with coupling between BiOBr, A-$TiO_2$, and Bt. Coupling BiOBr to A-$TiO_2$ shifts the peaks of BiOBr to high binding energies suggesting a weak interaction between BiOBr and $TiO_2$. However, growing A-$TiO_2$-BiOBr on Bt results in a shift of the Bi 4f peaks back to lower binding energies suggesting increased interaction between A-$TiO_2$ and BiOBr within the interlayer spacing of Bt. The additional peak at 156.55 eV is due to the interaction between Bi and Bt through a Bi-O-Si bond.

The Ti 2p spectra of each of A-$TiO_2$, $Ti_1Bi_1$, and $Ti_1Bi_1Bt_2$ (**Figure 4.6e**) were resolved into two peaks at around 458 and 464 eV. The former Ti 2p peak is ascribed to $Ti^{4+}$ $2p_{3/2}$ and the latter is associated with $Ti^{4+}$ $2p_{1/2}$ [5,10]. Though unexpected, there is no evidence of the existence of $Ti^{3+}$. Of interest is that coupling A-$TiO_2$ to BiOBr shifts the binding energies of Ti 2p to higher values due to the formation of a Ti-O-Bi between A-$TiO_2$ and BiOBr [20]. Furthermore, when A-$TiO_2$-BiOBr is grown on Bt to form $Ti_1Bi_1Bt_2$, the Ti 2p peaks shift to higher binding energy due to the additional Ti-O-Si chemical bond between A-$TiO_2$ and Bt [6]. To investigate the effect of calcination on the chemical states of the $TiO_2$ on $Ti_1Bi_1Bt_2$, a comparison was drawn between Ti 2p spectra of $Ti_1Bi_1Bt_2$ and $Ti_1Bi_1Bt_2$-400. As can be seen in **Figure 4.6f**, calcination shifts the two Ti 2p indicative peaks to higher binding energy values.

The O 1s spectra of A-$TiO_2$, BiOBr, $Ti_1Bi_1$, and $Ti_1Bi_1Bt_2$ were resolved as presented in **Figure 4.6g**. The broad O 1s peak of BiOBr was resolved into two peaks centered at 529.67, 531.69, and 533.21 eV. These peaks correspond to the lattice O in $[Bi_2O_2]^{2+}$ typical to that of BiOBr, surface -OH groups, and adsorbed $H_2O$ respectively. The $[Bi_2O_2]^{2+}$ peak, Bi $4f_{7/2}$, and Bi $4f_{5/2}$ peaks and the Br $3d_{5/2}$ and Br $3d_{3/2}$ in the O 1s, Bi 4f and Br 3d spectra of BiOBr respectively are constructive evidence of the existence of BiOBr. A-$TiO_2$ also has a similar peak that when resolved gives 3 peaks centered at 529.86, 531.13, and 533.28 eV corresponding to lattice O (Ti-O), surface -OH groups, and adsorbed $H_2O$. The O in $Ti_1Bi_1$ exists in three chemical states as shown by the three peaks at 529.92, 531.26, and 533.22 eV in O 1s spectra ascribed to lattice O, surface -OH groups, and adsorbed $H_2O$ molecules respectively as shown in **Figure 4.6g**. The same is observed in $Ti_1Bi_1Bt_2$ as its O 1s XPS spectrum contains 3 peaks centered at 529.89, 531.40, and 533.07 eV also corresponding to lattice O, surface -OH groups, and adsorbed water molecules respectively. Of interest is that the O 1s peak at 529.89 eV ascribed

to lattice O in $Ti_1Bi_1Bt_2$ is at lower binding energy than the lattice O in $Ti_1Bi_1$ (529.92 eV) due to the Ti-O-Si and Bi-O-Si bonds between A-$TiO_2$-BiOBr and Bt.

The Si 2p spectrum in **Figure 4.6h** shows a single peak at 102.5 eV ascribed to the Ti-O-Si bond [6]. There is no evidence of a non-bonded $SiO_2$ peak in Bt at around 103.79 eV [6].

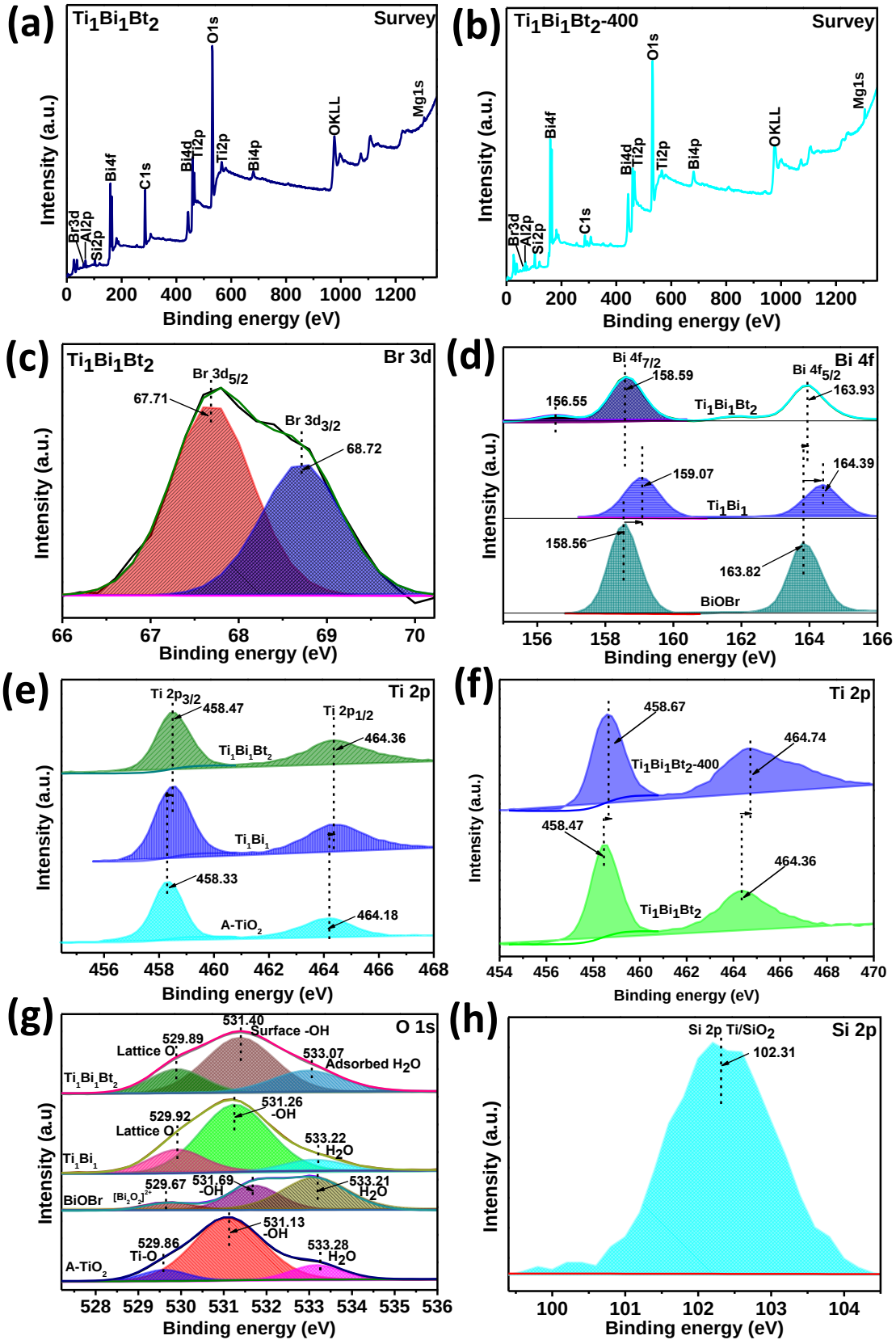



**Figure 4.6.** XPS spectra of $Ti_1Bi_1Bt_2$, $Ti_1Bi_1Bt_2$-400, $Ti_1Bi_1$, BiOBr and A-$TiO_2$: (a) survey of $Ti_1Bi_1Bt_2$, (b) survey of $Ti_1Bi_1Bt_2$-400, (c) Br 3d, (d) Bi 4f, (e)-(f) Ti 2p, (g) O 1s and (h) Si 2p.

## 4.5. $N_2$ adsorption-desorption studies

The specific surface area and pore size distribution of the Bt and the different photocatalysts were investigated through $N_2$ adsorption-desorption experiments. The $N_2$ adsorption-desorption isotherms are presented in **Figure 4.7** and the respective BET surface areas, pore-volume, and pore sizes are presented in **Table 4.2**. Moreover, the pore size distribution curves are shown in **Figure S2.**

Among the materials, BiOBr exhibited a typical IUPAC adsorption isotherm of type III with a tiny hysteresis loop of type H3 [5]. The H3 hysteresis loop proves the existence of a non-rigid aggregation of plate-like BiOBr nanoparticles to form BiOBr microspheres [2] and the low BET surface area of 6.9 $m^2/g$ is consistent with the low surface areas reported in other studies [5,10]. A-$TiO_2$ is the material with the lowest BET surface area of 5.9 $m^2/g$ and also manifests a tiny hysteresis loop in its type III isotherm due to its mesoporous nature. $Ti_1Bi_1$ exhibits an adsorption isotherm of type II with a tiny hysteresis loop which was also reported for macroporous A-$TiO_2$-BiOBr materials by Wei et al.[5].

The Bt and all the Bt-based hybrid architectures display typical IUPAC type IV isotherms with hysteresis loops of type H4. The H4 hysteresis loops suggest the existence of micro-mesoporous structures in these materials [2] as confirmed by pore size distribution curves in (**Figure S2**) and pore sizes ranging from 2-50 nm (**Table 4.2**). **Table 4.2** also shows that the uncalcined ternary heterostructures have high BET surface areas with $Ti_1Bi_1Bt_2$ having the highest. $Bi_1Bt_1$ is the only Bt-based material with a BET surface area lower than that of Bt and this is not uncommon as other studies on BiOBr/clay heterostructures have reported on this observation [6,21]. There is also another trend in **Table 4.2** where the pore size of BiBt-based heterostructures increases with an increase in BiOBr content within the heterostructures in the order $Ti_3Bi_1Bt_4$ (6.3 nm) < $Ti_1Bi_1Bt_2$-400 (7.3 nm) < $Ti_1Bi_1Bt_2$ (8.3 nm) < $Ti_1Bi_3Bt_4$ (9.3 nm) < $Bi_1Bt_1$ (11.2 nm). Furthermore among the uncalcined ternary heterostructures the pore volume increases with increasing BiOBr formula units per unit mass of composite in the order $Ti_3Bi_1Bt_4$ (0.052 $cm^3$) < $Ti_1Bi_1Bt_2$ (0.124 $cm^3$) < $Ti_1Bi_3Bt_4$ (0.141 $cm^3$). This suggests that increasing the BiOBr content in the ternary uncalcined heterostructures increases the pore size and pore volume. These observed trends are attributed to the dispersion of the BiOBr sheets within A-$TiO_2$ and in the Bt interlayer spacing [6].

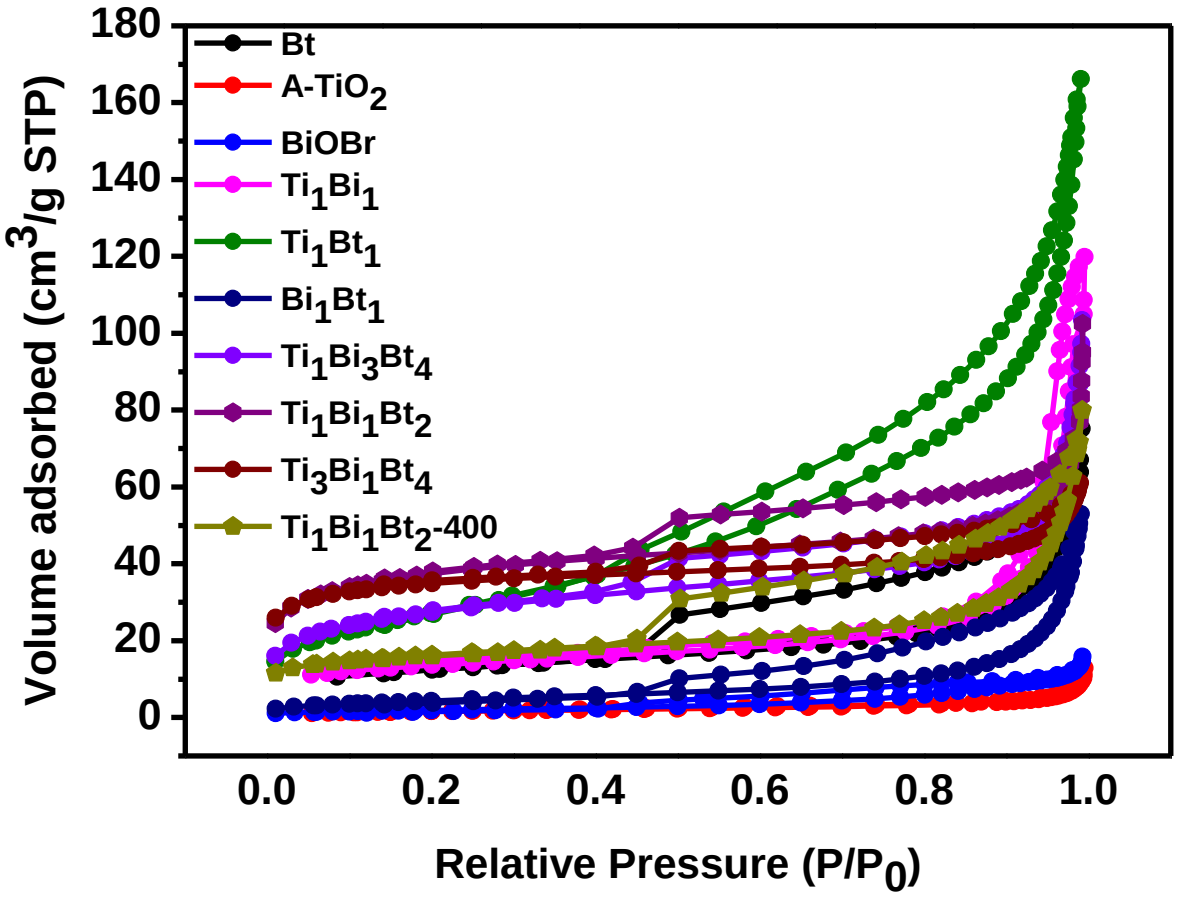



**Figure 4.7.** $N_2$ adsorption-desorption isotherms of raw Bt and the different photocatalysts.

**Table 4.2. BET Surface Area, Pore Volume, and Pore size of Bt and the different photocatalysts**

| Sample | BET surface area ($m^2/g$) | Pore volume ($cm^3/g$) | Pore size (nm) |
|---|---|---|---|
| Bt | 41.0 | 0.118 | 8.3 |
| A-$TiO_2$ | 5.9 | 0.014 | 10.7 |
| BiOBr | 6.9 | 0.091 | 5.9 |
| $Ti_1Bi_1$ | 49.0 | 0.170 | 25.1 |
| $Ti_1Bt_1$ | 98.9 | 0.252 | 9.8 |
| $Bi_1Bt_1$ | 15.9 | 0.082 | 11.2 |
| $Ti_1Bi_1Bt_2$ | 124.8 | 0.124 | 8.3 |
| $Ti_1Bi_3Bt_4$ | 93.6 | 0.141 | 9.3 |
| $Ti_3Bi_1Bt_4$ | 113.8 | 0.052 | 6.3 |
| $Ti_1Bi_1Bt_2$-400 | 54.5 | 0.124 | 7.3 |

## 4.6. UV-Vis analysis

The UV-vis spectra of the different heterostructures were collected to gather information about the photoactivation energy. The absorption spectra of each material are presented in **Figure 4.8a** and the bandgap energies of all the materials were estimated using the Tauc plot method as shown in **Figure 4.8b** and **Table 4.3.**

In the Tauc method the energy-dependent absorption coefficient α is expressed as:

$$(\alpha \cdot h\nu)^{1/\gamma} = B(h\nu - E_g) \qquad \textbf{4.2}$$

where $h$ is the Planck constant, ν is the frequency, $B$ is a constant, and $E_g$ is the bandgap energy [22]. The $\gamma$ factor assumes the value 1/2 or 2 for direct or indirect transition photoactivation energy, respectively [22].

From the absorption spectra, the Bt support material absorbs in the UV region and has the highest bandgap. Among the photocatalytic materials, bare A-$TiO_2$ absorbs in the UV region and has the widest bandgap energy (3.80 eV) which is higher than that of rutile, and this is consistent with previously reported predictions from AIMD simulations [23]. The as-synthesized bare BiOBr absorbs in the visible region and has the lowest bandgap of 2.84 eV which is in the typical 2.64-2.91 eV bandgap range for BiOBr [24,25] and is therefore easily photoactivated under visible light. The immobilization of BiOBr on Bt to form $Bi_1Bt_1$ results in a bandgap of 3.14 eV which is significantly higher than that of BiOBr due to the high bandgap of Bt as a complementary component. On the contrary, immobilization of A-$TiO_2$ on Bt gives a $Ti_1Bt_1$ heterostructure, with a bandgap of 3.55 eV which is lower than either A-$TiO_2$ or Bt. This is because Bt contains traces of Fe (**Table 4.1**) which normally undergoes isomorphous substitution with Si atoms in the tetrahedral sheets of Bt and contact A-$TiO_2$ resulting in reduced bandgap due to sensitization [26].

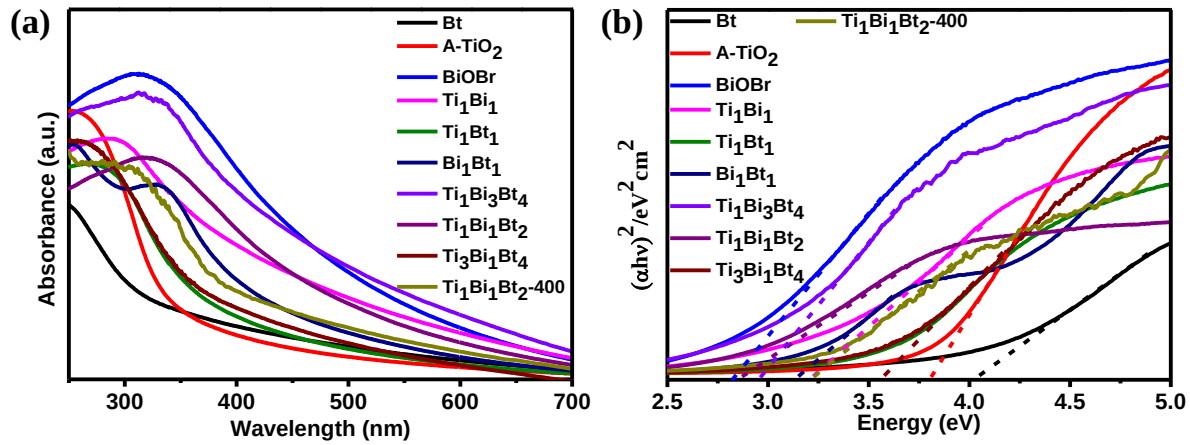



**Figure 4.8.** (a) The UV-Vis spectra and (b) Tauc plots of Bt and the different photocatalysts.

**Table 4.3. Bandgap energies of Bt and the different photocatalysts extracted from the Tauc plots.**

| Photocatalytic material | Bandgap (eV) |
|---|---|
| Bt | 4.04 |
| A-$TiO_2$ | 3.80 |
| BiOBr | 2.84 |
| $Ti_1Bi_1$ | 3.15 |
| $Ti_1Bt_1$ | 3.55 |
| $Bi_1Bt_1$ | 3.14 |
| $Ti_1Bi_3Bt_4$ | 2.96 |
| $Ti_1Bi_1Bt_2$ | 2.86 |
| $Ti_3Bi_1Bt_4$ | 3.55 |
| $Ti_1Bi_1Bt_2$-400 | 3.23 |

According to **Figure 4.8** and **Table 4.3**, coupling A-$TiO_2$ on BiOBr and immobilizing A-$TiO_2$ onto Bt results in binary structures with bandgaps lower than A-$TiO_2$, it is duly expected that the two mechanisms work in synergy in the fabricated ternary structures to lower the bandgap to some extent. Two of the ternary composites viz: $Ti_1Bi_1Bt_2$ and $Ti_1Bi_3Bt_4$ have a lower bandgap compared to that of $Ti_1Bi_1$, $Bi_1Bt_1$, and $Ti_1Bt_1$. The lower bandgap among the two ternary heterostructures is ascribed to the sensitization induced by the ternary heterojunction and significant amount of BiOBr microparticles in these materials which is capable of sensitizing A-$TiO_2$. Moreover, $Ti_1Bi_1Bt_2$ has the highest number of A-$TiO_2$-BiOBr p-n heterojunctions due to the equal masses of BiOBr and A-$TiO_2$ allowing sufficient sensitization mechanisms resulting in the consequential low bandgap. Accordingly, $Ti_3B_1Bt_4$ has the highest bandgap among all the ternary heterostructures owing to the high percentage of high bandgap A-$TiO_2$ semiconductor centers compared to BiOBr centers.

## 4.7. PL analysis

The PL spectra shown in **Figure 4.9** were collected to compare the electron-hole recombination rates in the different materials after photoactivation. BiOBr has the highest recombination rate suggesting a short electron-hole diffusion radius. By extension, few electrons and holes from BiOBr can traverse through its bulk to the surface for the interfacial redox reactions required

to produce sufficient ROS during photoactivation, and this is a typical property of most low bandgap semiconductors [27]. A-$TiO_2$ has the second-highest intensity in the emission spectra which is slightly lower than that of BiOBr. The lower electron-hole recombination rate of A-$TiO_2$ is due to the preponderance of crystallographic disorders which preferentially induce trapping sites as opposed to recombination centers [17,28,29].

Coupling equal masses of A-$TiO_2$ and BiOBr to form $Ti_1Bi_1$ significantly reduces the intensity of the emission spectra due to the electron-hole separation induced by the p-n heterojunction which occurs along the (001) faces of BiOBr [9]. However, after immobilization of either A-$TiO_2$ or BiOBr on Bt, the emission spectra decrease considerably more than in $Ti_1Bi_1$ due to electron transfer along the surfaces of Bt [26]. The aforementioned observation suggests that the electron transfer process along the Bt surfaces from either A-$TiO_2$ or BiOBr centers is the most important electron-hole separation mechanism in the ternary composites compared to the A-$TiO_2$-BiOBr p-n heterojunction.

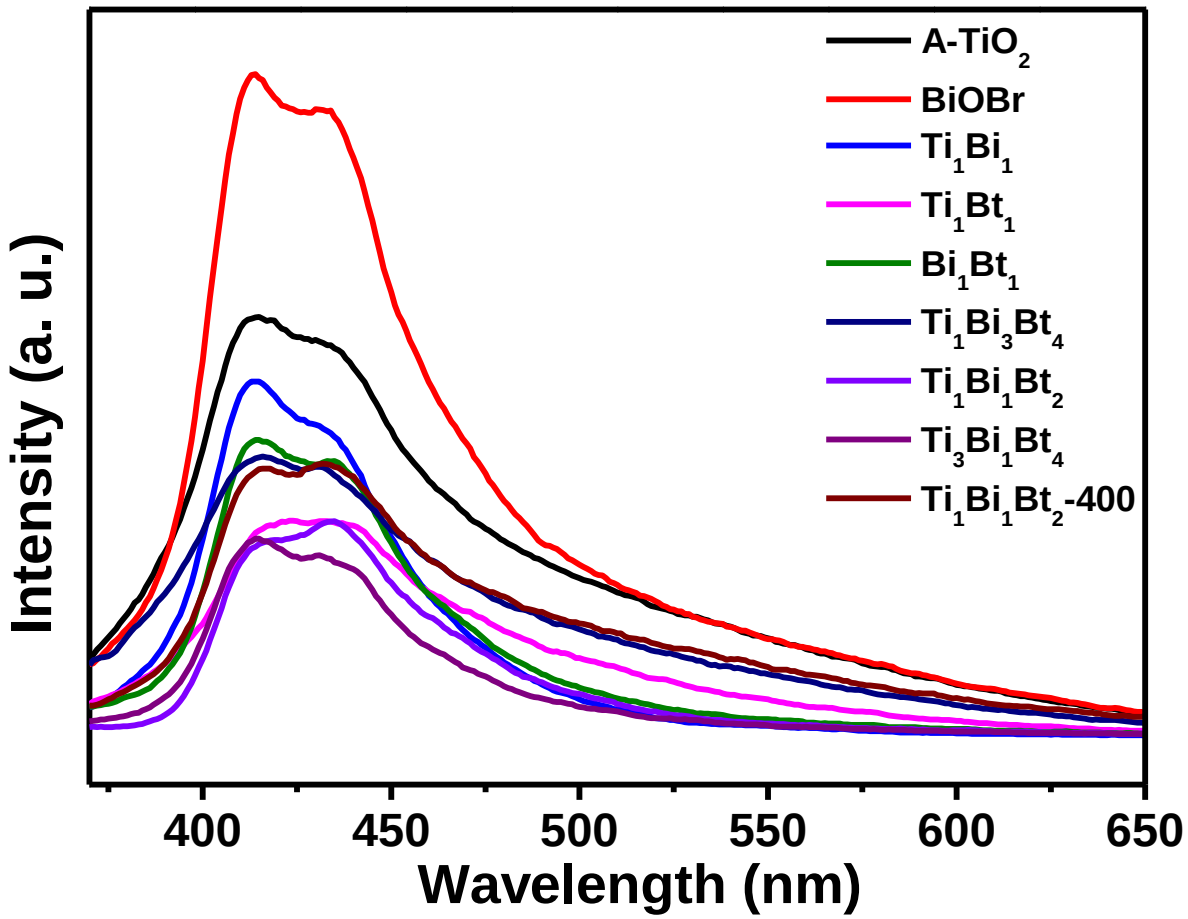



**Figure 4.9.** The PL spectra of Bt and the different photocatalysts.

The in situ growth of the A-$TiO_2$-BiOBr binary structures on Bt also reduces the emission intensity even further. This is due to the low electron-hole recombination rate induced by the synergic effect of both the A-$TiO_2$-BiOBr p-n heterojunction [9] and the effective electron transfer process along the Bt surfaces [26] through the Ti-O-Si and Bi-O-Si bonds. $Ti_3Bi_1Bt_4$ has the lowest electron-hole recombination rate due to the dominance of the A-$TiO_2$ centers which have intrinsic low recombination rates compared to BiOBr centers. $Ti_1Bi_1Bt_2$ has a low electron-hole recombination rate due to the high number of A-$TiO_2$-BiOBr heterojunctions in its structure attributed to the equal masses of A-$TiO_2$ and BiOBr and these heterojunctions are responsible for the delay in electron-hole recombination by providing electron trapping centers [6]. However, the pyrolysis of $Ti_1Bi_1Bt_2$ at 400 °C results in an inherent increase in the PL intensity suggesting an increase in the electron-hole recombination ascribed to the loss of the oxygen vacancies [6].

## 4.8. Point of zero charge ($pH_{PZC}$) determination

The pH-dependent net surface charge of Bt and the different photocatalysts directs the degree of adsorption of aqueous pollutants onto their surfaces under different pH environments. It is for this reason that the $pH_{PZC}$ of each of the materials used in this study was determined using the pH drift test to investigate the nature of their surface charges at various pH values.

If the pH of any solution is above the $pH_{PZC}$ of the powder or solid of interest, the surface functional groups of the material get deprotonated by the hydroxyl groups in the solution resulting in excess $H^+$ ions in the surrounding solution and the surface of the catalyst possesses negative charges and pH of the media shifts to the acidic region [30,31]. However, if the pH of the solution is below the $pH_{PZC}$, the surface functional groups of the powder readily get protonated by the surrounding solution and gain a positive charge [30,31]. So determining the $pH_{PZC}$ is probing the acid-base character of the surfaces of the solids in electrolytic suspensions under varying pH values [3].

**Figure 4.10** shows the $pH_{PZC}$ of the materials used in this study approximated to ±0.01 pH unit using the pH drift method and the values are formally presented in **Table 4.4**. The variation of $pH_{final}$ for different $pH_{initial}$ in all the materials being investigated in this work shows a similar trend. For all the materials, there is a net positive charge on the surfaces of all the materials in the $pH < pH_{PZC}$ region and a net negative charge in the $pH > pH_{PZC}$ region [30].

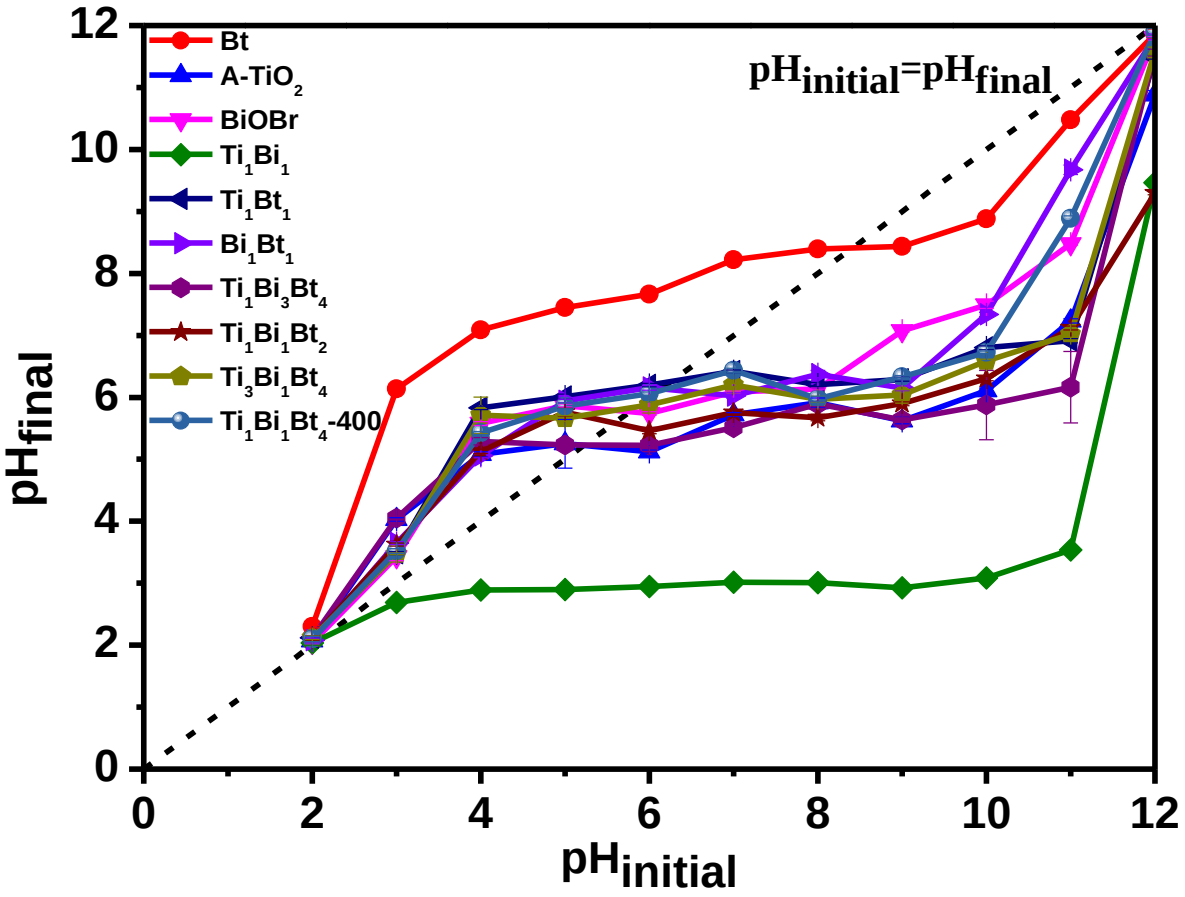



**Figure 4.10.** $pH_{final}$ vs $pH_{initial}$ graph of raw Bt and the different photocatalysts.

**Table 4.4. The $pH_{PZC}$ of Bt and the different photocatalysts**

| **Photocatalytic material** | **$pH_{PZC}$** |
|---|---|
| Bt | 8.39 |
| A-$TiO_2$ | 5.02 |
| BiOBr | 5.76 |
| $Ti_1Bi_1$ | 2.08 |
| $Ti_1Bt_1$ | 6.26 |
| $Bi_1Bt_1$ | 6.13 |
| $Ti_1Bi_1Bt_2$ | 5.61 |
| $Ti_1Bi_3Bt_4$ | 5.03 |
| $Ti_3Bi_1Bt_4$ | 5.85 |
| $Ti_1Bi_1Bt_2$-400 | 6.04 |

Of the materials being investigated, Bt has the highest $pH_{PZC}$ (pH 8.39) suggesting it has positively charged surfaces throughout the acidic pH range. As already stated in the literature

review section, the surface of Mt (Bt) assumes a negative charge due to the isomorphous substitution of octahedral $Al^{3+}$ by $Mg^{2+}$ and the isomorphous substitution of tetrahedral $Si^{4+}$ by $Al^{3+}$ [32]. However, the surface charges on Bt vary widely due to the varying composition of Bt and also due to the varying degrees of isomorphous substitution of the cations in its octahedral and tetrahedral layers. Therefore, the high $pH_{PZC}$ of the Bt used in this study suggests that there is an insignificant isomorphous substitution of $Al^{3+}$ and $Si^{4+}$ in the octahedral and octahedral layers by the aliovalent cations i.e. $Mg^{2+}$ and $Al^{3+}$ respectively compared to most Bt clays studied.

Several papers have presented varying values of the point of zero charges of Bt using different methods such as zeta potential [16], pH drift [33], pH titration [34], and potentiometric titration [35] among others. For example, Baloyi et al. [16] reported that the Bt used in their study had a negative surface in the whole pH scale. Aghazadeh et al. [33] reported 5.3, Emam et al. [35] reported 7.73, and Baik et al. reported 8.2 [36]. The change in pH of NaCl solutions after coming into contact with Bt is due to the protonation/deprotonation reactions of the octahedral aluminol and silanol groups presented in **equations 4.3-4.6** [34,37]. At pH values higher than $pH_{PZC}$ the tetrahedral silanol groups and the octahedral aluminol groups are deprotonated by the $OH^-$ groups and the Bt surface becomes negatively charged while at pH lower than the $pH_{PZC}$ the silanol groups get protonated and the Bt surfaces become positively charged [34,37].

$$Al\text{-}OH + H^+ \rightarrow Al\text{-}OH_2^+ \quad \textbf{4.3}$$

$$Al\text{-}OH + OH^- \rightarrow Al\text{-}O^- + H_2O \quad \textbf{4.4}$$

$$Si\text{-}OH + H^+ \rightarrow Si\text{-}OH_2^+ \quad \textbf{4.5}$$

$$Si\text{-}OH + OH^- \rightarrow Si\text{-}O^- + H_2O \quad \textbf{4.6}$$

BiOBr has a $pH_{PZC}$=5.76, and this is closer to the 4.34 reported by Meng et al. [38], 3.98 reported by Yang et al. [39], and the 5.30 reported by Imam et al. [40]. Surface OH groups are also observed in the O 1s spectrum of BiOBr as shown in **Figure 4.6g** and they have a profound effect on the surface charges on BiOBr because they readily undergo protonation/deprotonation reactions in solution. However, Lyu et al. [41] claimed that the surface hydroxyl groups have no bearing on the adsorption capacity of BiOBr.

The $pH_{PZC}$ of A-$TiO_2$ used in this study is 5.02 and this value is in the 2-8.9 range reported for anatase and rutile [42,43]. Generally, when $TiO_2$ comes to contact with water, the water gets adsorbed and surface OH groups are generated due to the reaction of $O^{2-}$ of $TiO_2$ and the adsorbed water molecules [44–46]. The generated OH groups are of two forms viz: terminal OH groups (Ti-$OH^-_t$) where the OH is bound to a surface $Ti^{4+}$ site, which has five coordinates to the lattice oxide ions, and bridging OH groups (Ti-$OH^-_{br}$-Ti) where each OH group is bound to a $Ti^{4+}$ site, which has four coordinates to the lattice oxide ions [45]. Bridging OH groups are polar due to the coordination of several $TiO_2$ ions and therefore acidic with $pK_a$=2.9 and terminal OH groups exhibit a basic character ($pK_a$=12.7) [47].

Salvador [48] reported that bridging OH groups are the ones that release $H^+$ and become negatively charged at pH values above the $pH_{PZC}$, while terminal OH groups accept an $H^+$ at pH values below the $pH_{PZC}$ and become positively charged in a manner presented in **equation 4.7** and **4.8.**

$$Ti\text{-}OH^-_t + H^+ \rightarrow Ti\text{-}(H_2O)_t \qquad \textbf{4.7}$$

$$Ti\text{-}OH^-_{br}\text{-}Ti + OH^- \rightarrow Ti\text{-}O_{br}\text{-}Ti + H_2O \qquad \textbf{4.8}$$

Since Ti-$OH^-_{br}$-Ti occurs at low pH values below 4.3 [49] due to its low $pK_a$, that would suggest that the population of Ti-$OH^-_{br}$-Ti in the A-$TiO_2$ used in this study is relatively higher than that of Ti-$OH^-_t$ due to the observed low $pH_{PZC}$ of A-$TiO_2$.

There is, however, an interesting prospect on the surface charges of the composite formed by coupling A-$TiO_2$ and BiOBr viz $Ti_1Bi_1$. This composite has a $pH_{PZC}$=2.08 which is far lower than the $pH_{PZC}$ of either BiOBr or A-$TiO_2$. Therefore $Ti_1Bi_1$ is positively charged on a broader pH region from 2.08-14. The low $pH_{PZC}$ compares well with the 3.8 reported for a crystalline 15% BiOBr/$TiO_2$ composite [50].

Fundamentally, the $pH_{PZC}$ value of $TiO_2$-based heterostructures is influenced by the type of surface OH groups of $TiO_2$ that form the chemical bond with other components, in this case, BiOBr. When other component interacts with the acidic bridging OH groups of $TiO_2$, the $pH_{PZC}$ shifts to higher pH values. However, if it interacts with the basic terminal OH group the $pH_{PZC}$ shifts to lower pH values. This was demonstrated by Tran et al. [51] on the interaction of amino acids and $TiO_2$ (**Figure 4.11)**. The interaction of $TiO_2$ acidic bridging OH groups with alanine (Ala) shifted the $pH_{PZC}$ to higher pH values and the interaction of basic $TiO_2$ terminal groups with tryptophan (Trp) shifted the $pH_{PZC}$ to lower pH values.

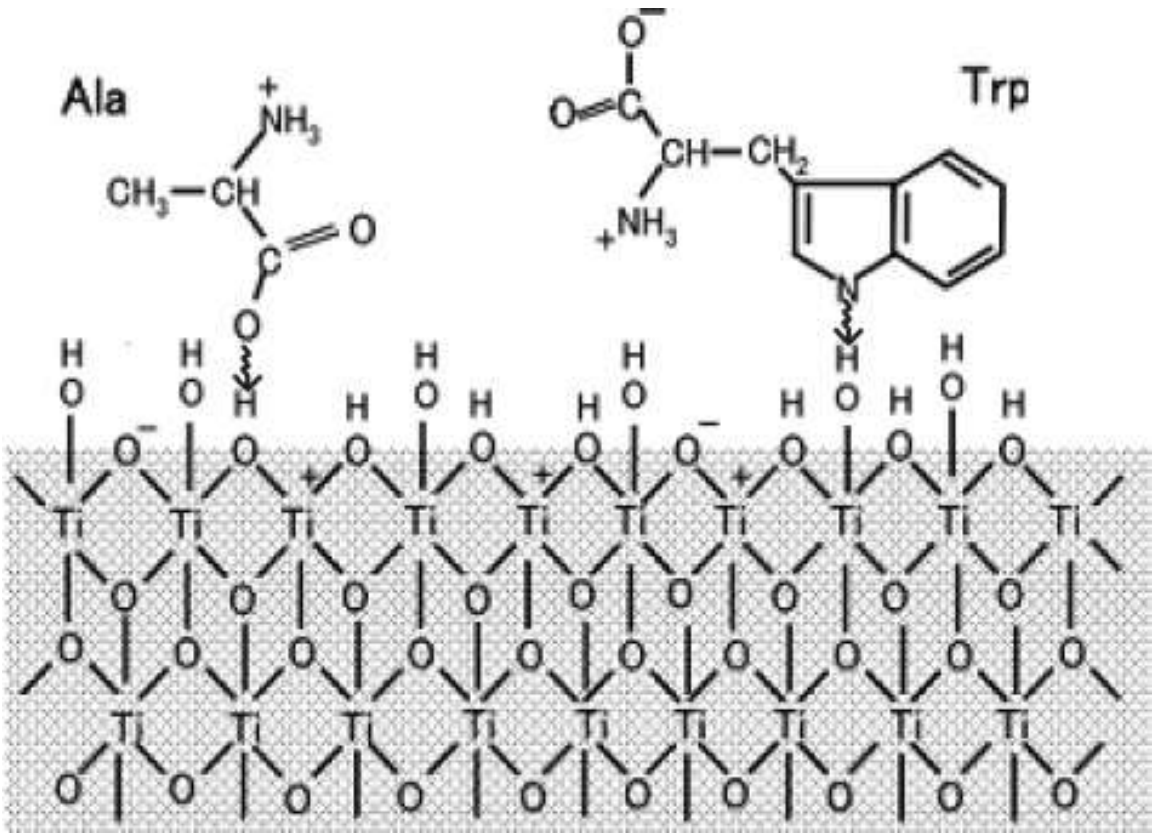



**Figure 4.11.** Interactions of Ala and Trp with the noncalcined $TiO_2$ surface [51].

From the reasoning outlined above, the low $pH_{PZC}$ of $Ti_1Bi_1$ is further evidence of the existence of the Ti-O-Bi bond between BiOBr and A-$TiO_2$. Furthermore, this predicts the formation of the Ti-O-Bi bond through the interaction of basic terminal OH groups in A-$TiO_2$ with BiOBr.

During synthesis A-$TiO_2$ and BiOBr functionalized Bt heterostructures, the addition of $Bi(NO_3)_3 \cdot 5H_2O$ (later functionalized with KBr) and A-$TiO_2$ results in the intercalation of the cations on the Bt surfaces deprotonating of the aluminol and silanol groups during the formation of M-O-Al and M-O-Si bonds (M=Bi or Ti) and generating $H^+$ into the surrounding aqueous environment in a manner akin to that reported by Alexander et al. [52]. However, due to the existence of OH groups in BiOBr and mainly in $TiO_2$, the $pH_{PZC}$ becomes a function of them and those on Bt.

To rationalize the $pH_{PZC}$ values of the binary and ternary clay heterostructures is a bit complicated as all the components have a contribution to the $pH_{PZC}$ value. It is unlike the $Ti_1Bi_1$ case where the two components i.e. A-$TiO_2$ and BiOBr with high $pH_{PZC}$ values give a composite with a low $pH_{PZC}$ value than either A-$TiO_2$ or BiOBr. However in the A-$TiO_2$-Bt-based materials, increasing the amount of BiOBr which is coupled with drop in the A-$TiO_2$ content results in a drop in the $pH_{PZC}$ value in the order $Ti_1Bt_1$ ($pH_{PZ}$=6.26) > $Ti_3Bi_1Bt_4$

($pH_{PZC}$=5.85) > $Ti_1Bi_1Bt_2$ ($pH_{PZC}$=5.61) > $Ti_1Bi_3Bt_4$ ($pH_{PZC}$=5.03). The drop in $pH_{PZC}$ is because BiOBr preferentially bonds to the basic terminal OH groups in the decreasing amount of A-$TiO_2$ formula units.

## 4.9. TGA analysis

The thermal stability of the heterostructures has been studied through thermogravimetric analysis (TGA) and derivative thermogravimetric analysis (DTG) from 35 to 900 °C and the TGA and DTG curves are shown in **Figure 4.12**.

The DTG plots, show that the raw Bt weight loss occurs in two stages i.e. at 35-158 °C, and 300-373 °C. The weight loss at 35-158 °C, is associated with the physically adsorbed water and loosely bound water molecules and the second stage (i.e. 300-373 °C) is attributed to the water molecules coordinated in the clay layers [53]. A-$TiO_2$ undergoes thermal decomposition in two major stages where the first step between 35-158.1 °C is due to the removal of physisorbed water molecules [54]. The second weight loss in the 296-371 °C temperature range is attributed to the removal of residual organics and crystallization of $TiO_2$ to anatase [54]. On BiOBr, there is no major mass loss at low temperatures and this is indicative of its purity and thermal stability [55]. The major loss shown by the major endothermic peak centered at 661 °C is due to the thermal transformation of BiOBr to form $Bi_2O_3$ [56].

The DTG curve of $Ti_1Bi_1$ shows three major thermal degradation regions 35-98 ºC, 112-170 ºC, and 247-443 ºC. Dehydration of adsorbed and coordinated water molecules occurs in the first two steps. In the last step (247-443 ºC) weight loss is due to the removal of residual organics and the crystallization of $TiO_2$ to anatase [54]. The overall thermal degradation of $Ti_1Bt_1$ also occurs in three stages. In the 35-104 °C range the mass loss is ascribed to the loss of physisorbed water molecules. The loss in the 127-243 °C range is due to the removal of coordinated water molecules in clay [53]. The last stage, (i.e. in the 267-368 °C range) is attributed to the removal of organics and crystallization of $TiO_2$ to anatase [54]. $Bi_1Bt_1$ shows good thermal stability at low temperatures and its overall thermal degradation occurs in 3 stages. The weight loss at 35-206 °C, is due to the physisorbed water molecules and residual organics. In the 270-360 °C region there is a loss of coordinated water molecules in Bt [53]. In the 600-700 °C range there is thermal degradation of BiOBr to form $Bi_2O_3$ such that the resulting composite becomes $Bi_2O_3$-Bt [56].

The DTG curves of the uncalcined ternary A-$TiO_2$-BiOBr-Bt nanocomposites show that they undergo thermal degradation in three main steps. The first degradation step in the 35-105 °C

range is due to the loss of physisorbed and loosely bound water molecules. The second is between 118 and 230 °C is due to the loss of residual organic precursors. The third is between 260 and 400 ºC range and is associated with the removal of organics and crystallization of $TiO_2$. However, at around 600 ºC there is a small inconsequential weight loss associated with the transformation of BiOBr to $Bi_2O_3$.

$Ti_1Bi_1Bt_2$-400 exhibits the best thermal stability because the thermal treatment at 400 ºC removes most of the adsorbed and coordinated water molecules as well the surface OH groups in the materials. The significant loss is in the 460-720 ºC range associated with the transformation of BiOBr to $Bi_2O_3$.

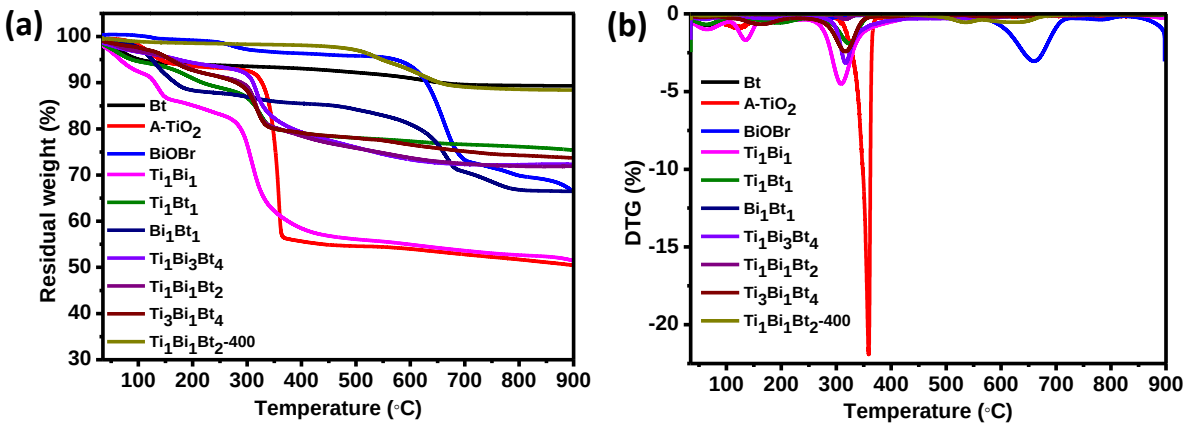



**Figure 4.12.** TGA (a) and DTG (b) curves of Bt and the different materials.

The anticipated use of the synthesized materials is the photocatalytic treatment of water under mild conditions. Therefore, weight loss is of no consequence when the materials are dispersed in water.

## 4.10. Conclusion

The PXRD, SEM, TEM, and BET analysis, provided evidence of the formation of high surface area ternary A-$TiO_2$-BiOBr-Bt heterostructures. From PXRD and $pH_{PZC}$ determination studies, it was demonstrated that the bond between A-$TiO_2$ and BiOBr occurs along the (001) faces of BiOBr and through the terminal OH groups of A-$TiO_2$. Furthermore, it was demonstrated through XPS analyses that the A-$TiO_2$-BiOBr photocatalytic material bonds to Bt through the Ti-O-Si and Bi-O-Si bonds in $Ti_1Bi_1Bt_2$. BET analysis demonstrated that all materials are mesoporous and the ternary heterostructures have high BET surface area with $Ti_1Bi_1Bt_2$ having the highest.

UV-Vis analysis showed that two ternary materials viz: $Ti_1Bi_1Bt_2$ and $Ti_1Bi_3Bt_4$, had low bandgap values compared to all the materials except BiOBr. PL analysis provided evidence that $Ti_1Bt_1$ and all the ternary heterostructures have suppressed electron recombination rates. Furthermore, it was demonstrated that all the materials but $Ti_1Bi_1$ have $pH_{PZC}$ in the 5-8.4 pH range suggesting that they are negatively charged below pH 5. Through TGA analysis, it was shown that all the materials exhibit good thermal stability under ambient conditions as they only undergo dehydration which is a nonexistent process in water treatment.

In conclusion, $Ti_1Bi_1Bt_2$ and $Ti_1Bi_3Bt_4$ have favorable physical, chemical, textural, and optoelectronic characteristics for efficient photocatalytic applications. These properties include high BET surface areas, favorable amounts of BiOBr to induce a low bandgap, and sufficiently low electron-hole pair recombination rates.

## References


[1] K. Cheng, Z. Heidari, A new method for quantifying cation exchange capacity in clay minerals, Appl. Clay Sci. 161 (2018) 444–455. https://doi.org/10.1016/j.clay.2018.05.006.

[2] M. Thommes, K. Kaneko, A. V. Neimark, J.P. Olivier, F. Rodriguez-Reinoso, J. Rouquerol, K.S.W. Sing, Physisorption of gases, with special reference to the evaluation of surface area and pore size distribution (IUPAC Technical Report), Pure Appl. Chem. 87 (2015) 1051–1069. https://doi.org/10.1515/pac-2014-1117.

[3] L.M. Bertus, R.A. Carcel, Prediction of $TiO_2$ and $WO_3$ nanopowders surface charge by the evaluation of point of zero charge (PZC), Environ. Eng. Manag. J. 10 (2011) 1021–1026. https://doi.org/10.30638/eemj.2011.148.

[4] M. Mushtaq, I.M. Tan, L. Ismail, M. Nadeem, M. Sagir, R. Azam, R. Hashmet, Influence of PZC (Point of Zero Charge) on the Static Adsorption of Anionic Surfactants on a Malaysian Sandstone, J. Dispers. Sci. Technol. 35 (2014) 343–349. https://doi.org/10.1080/01932691.2013.785362.

[5] X. Wei, H. Cui, S. Guo, L. Zhao, W. Li, Hybrid BiOBr-$TiO_2$ nanocomposites with high visible-light photocatalytic activity for water treatment, J. Hazard. Mater. 263 (2013) 650–658. https://doi.org/10.1016/j.jhazmat.2013.10.027.

[6] X. Hu, C. Li, J. Song, S. Zheng, Z. Sun, Multidimensional assembly of oxygen vacancy-rich amorphous $TiO_2$-BiOBr-sepiolite composite for rapid elimination of formaldehyde and oxytetracycline under visible light, J. Colloid Interface Sci. 574 (2020) 61–73. https://doi.org/10.1016/j.jcis.2020.04.035.

[7] E. Bárdos, V. Márta, L. Baia, M. Todea, G. Kovács, Hydrothermal crystallization of bismuth oxybromide (BiOBr) in the presence of different shape controlling agents, Appl. Surf. Sci. 518 (2020) 146184. https://doi.org/10.1016/j.apsusc.2020.146184.

[8] R. Li, C. Fan, X. Zhang, Y. Wang, Y. Wang, H. Zhang, Preparation of BiOBr thin films with micro-nano-structure and their photocatalytic applications, Thin Solid Films. 562 (2014) 506–512. https://doi.org/10.1016/j.tsf.2014.04.077.

[9] W. Deng, F. Pan, B. Batchelor, B. Jung, P. Zhang, A. Abdel-Wahab, H. Zhou, Y. Li, Mesoporous $TiO_2$-BiOBr microspheres with tailorable adsorption capacities for photodegradation of organic water pollutants: Probing adsorption-photocatalysis synergy by combining experiments and kinetic modeling, Environ. Sci. Water Res. Technol. 5 (2019) 769–781. https://doi.org/10.1039/c8ew00922h.

[10] X. Wang, W. Yang, F. Li, J. Zhao, R. Liu, S. Liu, B. Li, Construction of amorphous $TiO_2$/BiOBr heterojunctions via facets coupling for enhanced photocatalytic activity, J. Hazard. Mater. 292 (2015) 126–136. https://doi.org/10.1016/j.jhazmat.2015.03.030.

[11] S. Rengaraj, X.Z. Li, P.A. Tanner, Z.F. Pan, G.K.H. Pang, Photocatalytic degradation of methylparathion-An endocrine disruptor by $Bi^{3+}$-doped $TiO_2$, J. Mol. Catal. A. 247 (2006) 36–43. https://doi.org/10.1016/j.molcata.2005.11.030.

[12] C. Belver, J. Bedia, M.A. Álvarez-Montero, J.J. Rodriguez, Solar photocatalytic purification of water with Ce-doped $TiO_2$/clay heterostructures, Catal. Today. 266 (2016) 36–45. https://doi.org/10.1016/j.cattod.2015.09.025.

[13] T.J. Pinnavaia, Intercalated clay catalysts, Science 220 (4595) (1983) 365–371.

[14] V. V Krupskaya, S. V Zakusin, E.A. Tyupina, O.V. Dorzhieva, A.P. Zhukhlistov, P.E. Belousov, M.N. Timofeeva, Experimental Study of Montmorillonite Structure and Transformation of Its Properties under Treatment with Inorganic Acid Solutions, Minerals. 7 (2017) 1–15. https://doi.org/10.3390/min7040049.

[15] S. Kaufhold, R. Dohrmann, K. Ufer, F.M. Meyer, Comparison of methods for the quantification of montmorillonite in bentonites, Appl. Clay Sci. 22 (2002) 145–151. https://doi.org/10.1016/S0169-1317(02)00131-X.

[16] J. Baloyi, T. Ntho, J. Moma, Synthesis of highly active and stable Al/Zr pillared clay as catalyst for catalytic wet oxidation of phenol, J. Porous Mater. 26 (2019) 583–597. https://doi.org/10.1007/s10934-018-0667-3.

[17] M.A. Vargas, J.E. Rodríguez-páez, Amorphous $TiO_2$ nanoparticles: Synthesis and antibacterial capacity, J. Non. Cryst. Solids. 459 (2017) 192–205. https://doi.org/10.1016/j.jnoncrysol.2017.01.018.

[18] Q.L. Yuan, Y. Zhang, H.Y. Yin, Q.L. Nie, W.W. Wu, Rapid, simple and low-cost fabrication of BiOBr ultrathin nanocrystals with enhanced visible-light photocatalytic activity, J. Exp. Nanosci. 11 (2016) 359–369. https://doi.org/10.1080/17458080.2015.1065014.

[19] D. Zywitzki, H. Jing, H. Tuysuz, C.K. Chan, High surface area, amorphous titania with reactive $Ti^{3+}$ through a photo-assisted synthesis method for photocatalytic $H_2$ generation, J. Mater. Chem. A. 5 (2017) 10957–10967. https://doi.org/10.1039/c7ta01614j.

[20] F. Duo, Y. Wang, C. Fan, X. Mao, X. Zhang, Y. Wang, J. Liu, Low-temperature one-step synthesis of rutile $TiO_2$/BiOCl composites with enhanced photocatalytic activity, Mater. Charact. 99 (2015) 8–16. https://doi.org/10.1016/j.matchar.2014.11.002.

[21] J. Zhang, L. Zhang, S. Zhou, H. Chen, Y. Zhao, X. Wang, Exceptional visible-light-

induced photocatalytic activity of attapulgite–BiOBr–$TiO_2$ nanocomposites, Appl. Clay Sci. 90 (2014) 135–140. https://doi.org/10.1016/j.clay.2013.12.037.

[22] P. Makula, M. Pacia, W. Macyk, How To Correctly Determine the Band Gap Energy of Modified Semiconductor Photocatalysts Based on UV−Vis Spectra, J. Phys. Chem. Lett. 9 (2018) 6814–6817. https://doi.org/10.1021/acs.jpclett.8b02892.

[23] H.H. Pham, L. Wang, Oxygen vacancy and hole conduction in amorphous $TiO_2$, Phys.Chem.Chem.Phys. 2 (2015) 541–550. https://doi.org/10.1039/c4cp04209c.

[24] Y. Li, Z. Wang, B. Huang, Y. Dai, X. Zhang, X. Qin, Synthesis of BiOBr-PVP hybrids with enhanced adsorption-photocatalytic properties, Appl. Surf. Sci. 347 (2015) 258–264. https://doi.org/10.1016/j.apsusc.2015.04.105.

[25] C. Xue, J. Xia, T. Wang, S. Zhao, G. Yang, B. Yang, Y. Dai, G. Yang, A facile and efficient solvothermal fabrication of three-dimensionally hierarchical BiOBr microspheres with exceptional photocatalytic activity, Mater. Lett. 133 (2014) 274–277. https://doi.org/10.1016/j.matlet.2014.07.016.

[26] E. Tao, X. Xiao, S. Yang, A new synthesizing method of $TiO_2$ with montmorillonite: Effective photoelectron transfer to degrade Rhodamine B, Sep. Purif. Technol. 258 (2021) 118070. https://doi.org/10.1016/j.seppur.2020.118070.

[27] M.X. Song, M. Du, Q. Liu, F. Xing, C. Huang, X. Qiu, Enhancement of photocatalytic activities in hierarchical BiOBr microflowers induced by oxygen vacancies, Catal. Today. 335 (2019) 193–199. https://doi.org/10.1016/j.cattod.2018.11.006.

[28] B. Prasai, B. Cai, M.K. Underwood, J.P. Lewis, D.A. Drabold, Properties of amorphous and crystalline titanium dioxide from first principles, J. Mater. Sci. 47 (2012) 7515–7521. https://doi.org/10.1007/s10853-012-6439-6.

[29] T. Jia, J. Zhang, J. Wu, D. Wang, Q. Liu, Y. Qi, B. Hu, P. He, W. Pan, X. Qi, Synthesis amorphous $TiO_2$ with oxygen vacancy as carriers transport channels for enhancing photocatalytic activity, Mater. Lett. 265 (2020) 127465. https://doi.org/10.1016/j.matlet.2020.127465.

[30] M. Pashai Gatabi, H. Milani Moghaddam, M. Ghorbani, Point of zero charge of maghemite decorated multiwalled carbon nanotubes fabricated by chemical precipitation method, J. Mol. Liq. 216 (2016) 117–125. https://doi.org/10.1016/j.molliq.2015.12.087.

[31] A. Kausar, K. Naeem, M. Tariq, Z.I.H. Nazli, H.N. Bhatti, F. Jubeen, A. Nazir, M. Iqbal, Preparation and characterization of chitosan/clay composite for direct Rose FRN dye removal from aqueous media: Comparison of linear and non-linear regression methods,

J. Mater. Res. Technol. 8 (2019) 1161–1174. https://doi.org/10.1016/j.jmrt.2018.07.020.

[32] H. Yi, F. Jia, Y. Zhao, W. Wang, S. Song, H. Li, C. Liu, Surface wettability of montmorillonite (0 0 1) surface as affected by surface charge and exchangeable cations: A molecular dynamic study, Appl. Surf. Sci. 459 (2018) 148–154. https://doi.org/10.1016/j.apsusc.2018.07.216.

[33] V. Aghazadeh, S. Barakan, E. Bidari, Determination of surface protonation-deprotonation behavior, surface charge, and total surface site concentration for natural, pillared, and porous nano bentonite heterostructure, J. Mol. Struct. 1204 (2020) 127570. https://doi.org/10.1016/j.molstruc.2019.127570.

[34] E. Kristia, R. Pranowo, J. Sunarso, N. Indraswati, S. Ismadji, Performance of activated carbon and bentonite for adsorption of amoxicillin from wastewater: Mechanisms, isotherms, and kinetics, Water Res. 43 (2009) 2419–2430. https://doi.org/10.1016/j.watres.2009.02.039.

[35] E.A. Emam, Modified Activated Carbon, and Bentonite Used to Adsorb Petroleum Hydrocarbons Emulsified in Aqueous Solution, Am. J. Environ. Prot. 2 (2013) 161–169. https://doi.org/10.11648/j.ajep.20130206.17.

[36] M.H. Baik, S.Y. Lee, Colloidal stability of bentonite clay considering surface charge properties as a function of pH and ionic strength, J. Ind. Eng. Chem. 16 (2010) 837–841. https://doi.org/10.1016/j.jiec.2010.05.002.

[37] W. Du, Y. Yang, L. Hu, B. Chang, G. Cao, M. Nasir, Combined determination analysis of surface properties evolution towards bentonite by pH treatments, Colloids Surfaces A Physicochem. Eng. Asp. 626 (2021) 127067. https://doi.org/10.1016/j.colsurfa.2021.127067.

[38] X. Meng, Z. Li, J. Chen, H. Xie, Z. Zhang, Enhanced visible-light-induced photocatalytic activity of surface-modified BiOBr with Pd nanoparticles, Appl. Surf. Sci. 433 (2018) 76–87. https://doi.org/10.1016/j.apsusc.2017.09.103.

[39] L. Yang, L. Liang, L. Wang, J. Zhu, S. Gao, X. Xia, Accelerated photocatalytic oxidation of carbamazepine by a novel 3D hierarchical protonated g-$C_3N_4$/BiOBr heterojunction: Performance and mechanism, Appl. Surf. Sci. 473 (2019) 527–539. https://doi.org/10.1016/j.apsusc.2018.12.180.

[40] S.S. Imam, R. Adnan, N.H. Mohd Kaus, Immobilization of BiOBr into cellulose acetate matrix as hybrid film photocatalyst for facile and multicycle degradation of ciprofloxacin, J. Alloys Compd. 843 (2020) 155990. https://doi.org/10.1016/j.jallcom.2020.155990.

[41] J. Lyu, Z. Hu, Z. Li, M. Ge, Removal of tetracycline by BiOBr microspheres with oxygen vacancies: Combination of adsorption and photocatalysis, J. Phys. Chem. Solids. 129 (2019) 61–70. https://doi.org/10.1016/j.jpcs.2018.12.041.

[42] P. Górska, A. Zaleska, E. Kowalska, T. Klimczuk, J.W. Sobczak, E. Skwarek, W. Janusz, J. Hupka, $TiO_2$ photoactivity in vis and UV light: The influence of calcination temperature and surface properties, Appl. Catal. B Environ. 84 (2008) 440–447. https://doi.org/10.1016/j.apcatb.2008.04.028.

[43] M. Kosmulski, The significance of the difference in the point of zero charge between rutile and anatase, Adv. Colloid Interface Sci. 99 (2002) 255–264. https://doi.org/10.1016/S0001-8686(02)00080-5.

[44] C.Y. Wu, K.J. Tu, J.P. Deng, Y.S. Lo, C.H. Wu, Markedly enhanced surface hydroxyl groups of TiO2 nanoparticles with Superior water-dispersibility for photocatalysis, Materials (Basel). 10 (2017) 566. https://doi.org/10.3390/ma10050566.

[45] W. Li, D. Li, Y. Lin, P. Wang, W. Chen, X. Fu, Y. Shao, Evidence for the active species involved in the photodegradation process of methyl Orange on $TiO_2$, J. Phys. Chem. C. 116 (2012) 3552–3560. https://doi.org/10.1021/jp209661d.

[46] W. Yu, L. Zhao, F. Chen, H. Zhang, L.H. Guo, Surface Bridge Hydroxyl-Mediated Promotion of Reactive Oxygen Species in Different Particle Size $TiO_2$ Suspensions, J. Phys. Chem. Lett. 10 (2019) 3024–3028. https://doi.org/10.1021/acs.jpclett.9b00863.

[47] M.N. Toshihiro Kasuga, Hayato Kondo, Apatite formation on $TiO_2$ in simulated body fluid Toshihiro, J. Cryst. Growth. 235 (2001) 235–240.

[48] P. Salvador, Mechanisms of water photooxidation at n-$TiO_2$ rutile single crystal oriented electrodes under UV illumination in competition with photocorrosion, Prog. Surf. Sci. 86 (2011) 41–58. https://doi.org/10.1016/j.progsurf.2010.10.002.

[49] P.A. Connor, K.D. Dobson, A.J. Mcquillan, Infrared Spectroscopy of the $TiO_2$/Aqueous Solution Interface, Langmuir 1. 15 (1999) 2402–2408.

[50] J. Rashid, A. Abbas, L.C. Chang, A. Iqbal, I.U. Haq, A. Rehman, S.U. Awan, M. Arshad, M. Rafique, M.A. Barakat, Butterfly cluster like lamellar BiOBr/$TiO_2$ nanocomposite for enhanced sunlight photocatalytic mineralization of aqueous ciprofloxacin, Sci. Total Environ. 665 (2019) 668–677. https://doi.org/10.1016/j.scitotenv.2019.02.145.

[51] T.H. Tran, A.Y. Nosaka, Y. Nosaka, Adsorption and photocatalytic decomposition of amino acids in $TiO_2$ photocatalytic systems, J. Phys. Chem. B. 110 (2006) 25525–25531. https://doi.org/10.1021/jp065255z.

[52] J.A. Alexander, M.A.A. Zaini, A. Surajudeen, E.U. Aliyu, A.U. Omeiza, Surface

modification of low-cost bentonite adsorbents - A review, Part. Sci. Technol. 37 (2019) 538–549. https://doi.org/10.1080/02726351.2018.1438548.

[53] J. Baloyi, T. Ntho, J. Moma, A Novel Synthesis Method of Al/Cr Pillared Clay and its Application in the Catalytic Wet Air Oxidation of Phenol, Catal. Letters. 148 (2018) 3655–3668. https://doi.org/10.1007/s10562-018-2579-x.

[54] S.S. Juliet, S. Ramalingom, C. Ravidhas, A.M.E. Raj, Effect of Calcination Temperature on Titanium Oxide Nanocrystallites in the Anatase Phase Synthesized By Sol-Gel Route, IOSR J. Appl. Phys. 9 (2017) 32–39. https://doi.org/10.9790/4861-0904043239.

[55] K.S. Bhavsar, P.K. Labhane, R.B. Dhake, G.H. Sonawane, Crystal structures, morphological, optical, adsorption, kinetic and photocatalytic degradation studies of activated carbon loaded BiOBr nanoplates prepared by solvothermal method, Inorg. Chem. Commun. 104 (2019) 134–144. https://doi.org/10.1016/j.inoche.2019.04.002.

[56] R. Bibi, Q. Shen, L. Wei, D. Hao, N. Li, J. Zhou, Hybrid BiOBr/UiO-66-$NH_2$ composite with enhanced visible-light driven photocatalytic activity toward RhB dye degradation, RSC Adv. 8 (2018) 2048–2058. https://doi.org/10.1039/c7ra11500h.

# Chapter 5: Photocatalysis of phenol and optimization of operational conditions

## 5.0. Introduction

This fifth chapter of the dissertation presents the orderly investigation of the photocatalytic activity of the materials and the optimization of operational conditions.

The first step of the investigation was to select the most effective photocatalyst by dispersing each material in the phenol solution and then irradiating the resulting mixture. From the analysis of the results, special interest is on the materials' adsorption capacity before irradiation and their photocatalytic activity after t=0. Furthermore, careful analysis of the influence of the properties of the materials on their photocatalytic activity was attempted.

After selecting the most effective photocatalyst i.e. $Ti_1Bi_1Bt_2$, an investigation into the effect of selected operational parameters such as pH, catalyst dosage, and initial concentration on its photocatalytic activity was done. Accordingly, after optimization of the operational conditions, kinetic studies were resolved to explain the phenol photodegradation process.The recyclability and stability studies of the most efficient photocatalyst i.e. $Ti_1Bi_1Bt_2$ were conducted after the first six consecutive photocatalytic cycles.

Scavenging experiments were then done to identify the most dominant ROS influencing the photodegradation process under optimized operational conditions. The scavenging experiments coupled with PL analysis allowed for the rational proposal of possible charge transfer mechanisms on the $Ti_1Bi_1Bt_2$ photocatalyst during phenol photocatalysis.

## 5.1. Selecting a catalyst

The photocatalytic performance of all the heterostructures were tested on the photocatalytic remediation of a phenol solution with a concentration of 20 ppm at pH 4. The photocatalyst dosage was 100 mg, and the adsorption-photodegradation performance of each of the materials is presented in **Figure 5.1**. The contribution of phenol photolysis in this study is insignificant as only 1.6% of phenol is removed in the absence of Bt or any of the photocatalytic materials. Moreover, **Figure 5.1** shows that the dominant mode of phenol removal is photodegradation due to low adsorption on the materials before the lamp is turned on (-60-0 min range).

Among the stand-alone starting materials, BiOBr exhibited better abatement of phenol (65.2%) than either A-$TiO_2$ (57.7%) or Bt (16.6%) despite having the lowest adsorption capacity than all the materials used in this work. The better adsorption capacity of A-$TiO_2$ in comparison to BiOBr is ascribed to its comparatively larger surface area and the preponderance of surface hydroxyl groups and chemically adsorbed water on the surfaces of A-$TiO_2$ [1–3]. The enhanced phenol removal mainly through photodegradation on BiOBr in comparison to A-$TiO_2$ is due to BiOBr's enhanced ability to absorb visible light for the photogeneration of electrons and holes and other ROS attributed to its low bandgap (2.84 eV) favoring its photoactivation. Bt removes phenol predominantly through adsorption as its photocatalytic activity is so low. This is due to the absence of substantial amounts of photocatalytic material in Bt except for the Fe (III) which substituted the surface Si (IV) in the tetrahedral layer of Bt [4].

The binary photocatalysts have shown that there is a better abatement of phenol on $Ti_1Bi_1$ (76.1%) than $Bi_1Bt_1$ (71.3%) and $Ti_1Bt_1$ (62.1%) despite $Ti_1Bt_1$ having better adsorption capacity due to its higher BET surface area. The high removal rate of phenol on $Ti_1Bi_1$ is due to the low bandgap (3.15 eV) and the high number of active sites. This is because it constitutes predominantly of catalytic material and the main mode of phenol removal is through photocatalysis in all the materials. $Bi_1Bt_1$ has better phenol removal than $Ti_1Bt_1$ due to its low bandgap of 3.14 eV compared to 3.55 eV of $Ti_1Bt_1$ allowing it to have better visible light photoactivation.

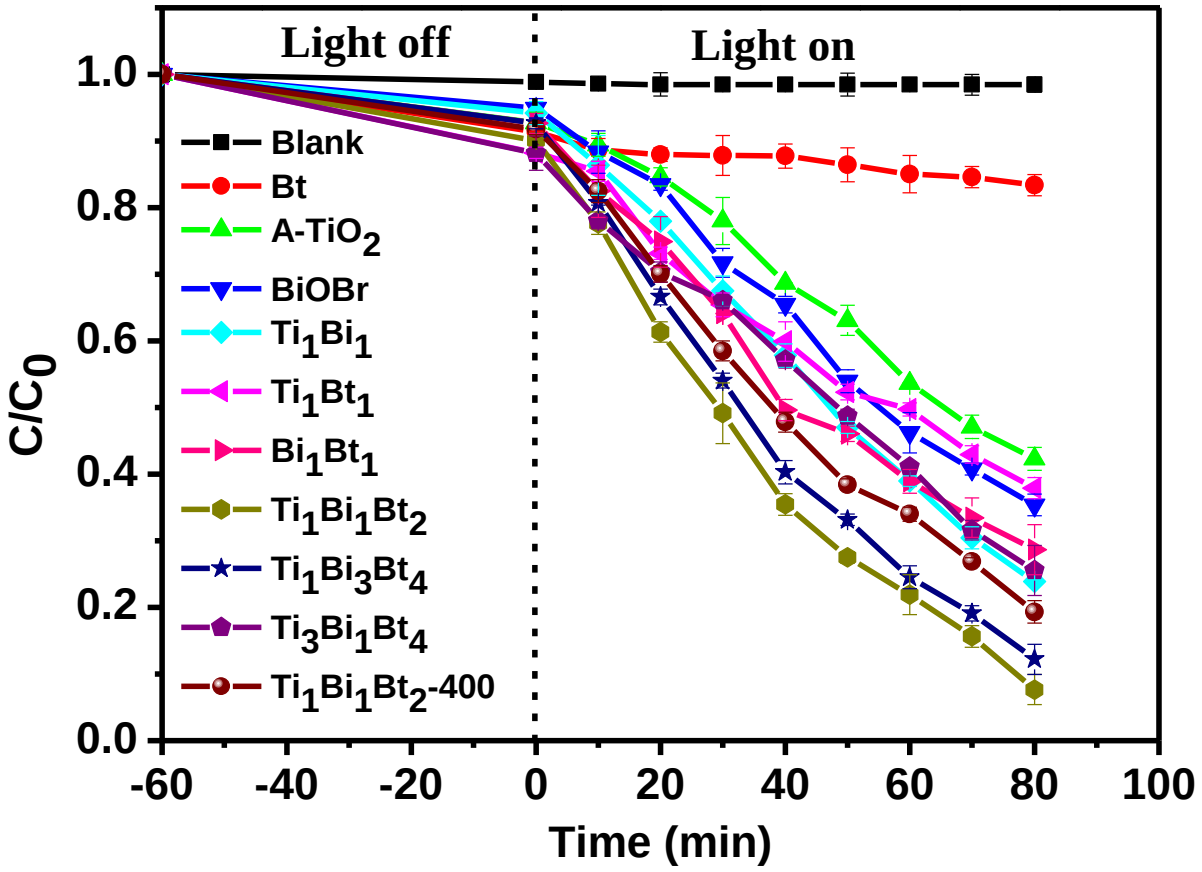



**Figure 5.1.** Removal of phenol under visible light irradiation using Bt and the different photocatalysts.

All the ternary structures except $Ti_3Bi_1Bt_4$ exhibited the highest conversion efficiencies towards phenol after 80 min of visible light irradiation. Among the ternary heterostructures, the phenol conversion was in the order: $Ti_1Bi_1Bt_2$ (91.8%) > $Ti_1Bi_3Bt_4$ (87.3%) > $Ti_1Bi_1Bt_2$-400 (79.1%) > $Ti_3Bi_1Bt_4$ (74.5%). The relatively high phenol conversion in $Ti_1Bi_1Bt_2$ is due to its favorable physicochemical and optoelectronic properties i.e. it has the lowest bandgap, highest surface area, and second-lowest electron-hole recombination rate compared to the other ternary materials. However, after calcination at 400 ºC, the bandgap and the electron-hole recombination rate increase, and the BET surface area drops significantly resulting in a comparative loss in the photocatalytic performance of $Ti_1Bi_1Bt_2$. $Ti_1Bi_1Bt_2$ was chosen for the optimization of some operational parameters in the succeeding sections due to the exceptional photocatalytic efficiency obtained/recorded.

## 5.2. Effect of the initial solution pH on the abatement of phenol

The effect of initial pH on the photocatalytic removal of phenol from a solution with an initial concentration of 20 ppm on 100 mg $Ti_1Bi_1Bt_2$ was investigated. The efficiency of phenol removal decreased in the order 94.0%, 79.7%, 74.8%, 63.9%, and 58.8% when the initial pH was set at 4, 6, 7, 8, and 10 respectively as shown in **Figure 5.2**. The decrease in phenol removal efficiency with increasing pH is consistent with a report by El Gaidoumi [5] on the photodegradation of phenol using $TiO_2$/pyrophyllite composite under UV irradiation.

Phenol is weakly acidic and readily ionizes to set up the equilibrium shown in **equation 5.1** [6]. The pH of the phenol solutions directs its degree of ionization of phenol molecules and this, in turn, impacts the extent of its adsorption and photodegradation. Considering that the $pK_a$ of phenol=9.89, high pH values shift the equilibrium to the right favoring the generation of more phenolate anions ($C_6H_5O^-$ ) [6].

$$C_6H_5OH \rightleftharpoons C_6H_5O^- + H^+ \qquad \textbf{5.1}$$

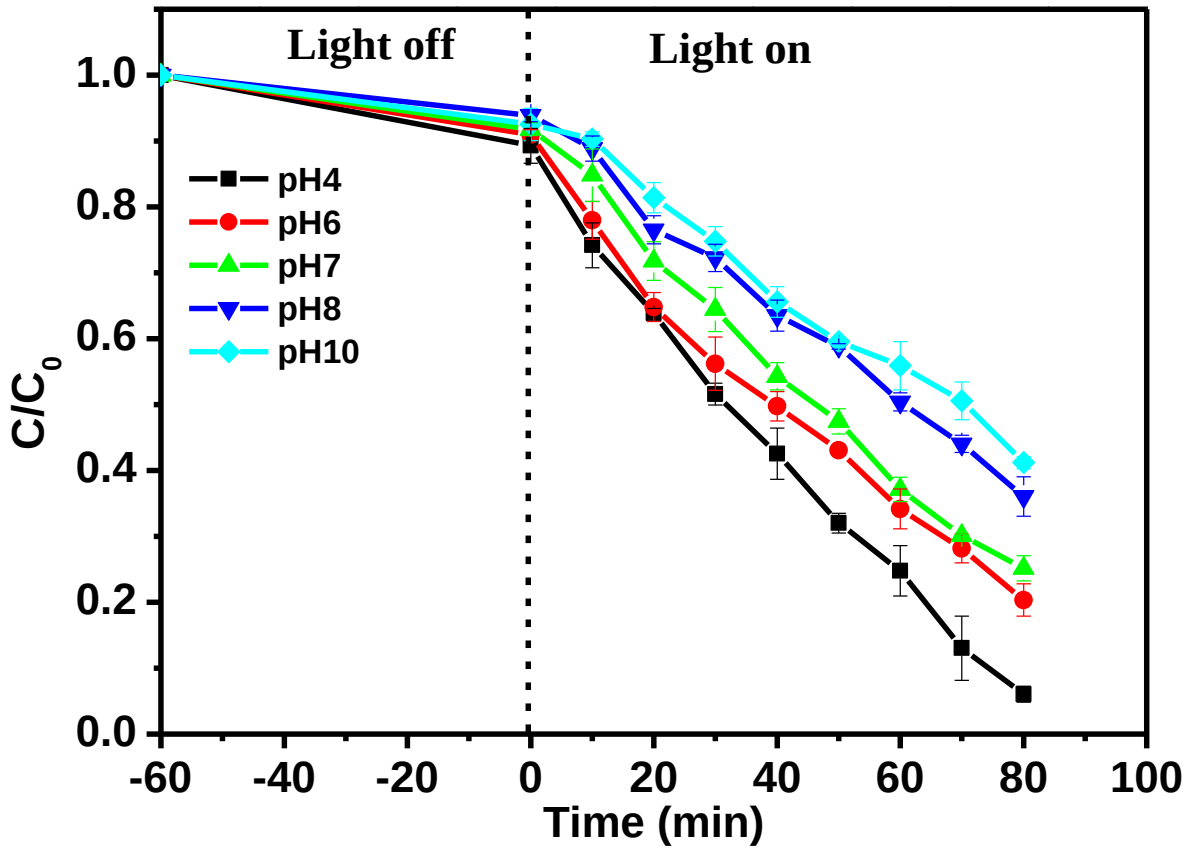



**Figure 5.2**. Removal of phenol on $Ti_1Bi_1Bt_2$ under visible light irradiation in different pH environments.

Phenolate ions are stabilized by resonance stabilization through the delocalization of the electron pair as shown in **Figure 5.3** allowing them to resist degradation due to the high resonance stabilization energy**.** At high pH, the phenol molecules exist in their stable phenolate form and that is why its photocatalytic removal decrease with pH increase.

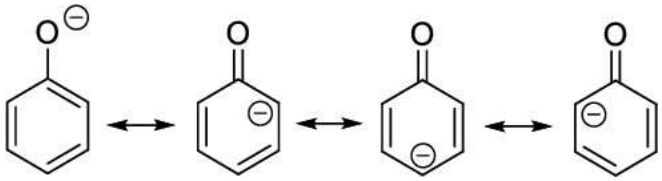


**Figure 5.3.** Resonance stabilization of a phenolate anion through the delocalization of the electron pair [7].

## 5.3. Influence of photocatalyst dosage on the removal of phenol

To investigate the effect of $Ti_1Bi_1Bt_2$ dosage on the phenol removal efficiency, the amount of $Ti_1Bi_1Bt_2$ added to 20 ppm phenol solution at pH 4 was varied from 50 to 200 mg and the results are presented in **Figure 5.4.** The mode of phenol removal on $Ti_1Bi_1Bt_2$ is through an adsorption-photodegradation synergy and therefore the efficiency of phenol removal increases with catalyst dosage. This is because more $Ti_1Bi_1Bt_2$ surfaces become available for the adsorption of phenol solution. Additionally, more active sites of $Ti_1Bi_1Bt_2$ per unit volume of phenol solution become available for the generation of more ROS through interfacial redox reactions on the photocatalyst's surface. As observed, 50 mg and 100 mg $Ti_1Bi_1Bt_2$ dosage resulted in the removal of 62.6% and 92.3% of phenol after 80 min respectively. A dosage of 200 mg resulted in the complete removal of phenol within 60 min of irradiation while a 150 mg dosage resulted in the complete phenol removal within 70 min. The interval for complete phenol removal between 150 mg and 200 mg dosage is 10 min and considering that there is a 50 mg mass difference needed to reduce the reaction time for the complete removal of phenol by 10 min, 150 mg was arbitrarily chosen as the optimum dosage for all further investigations for economic reasons.

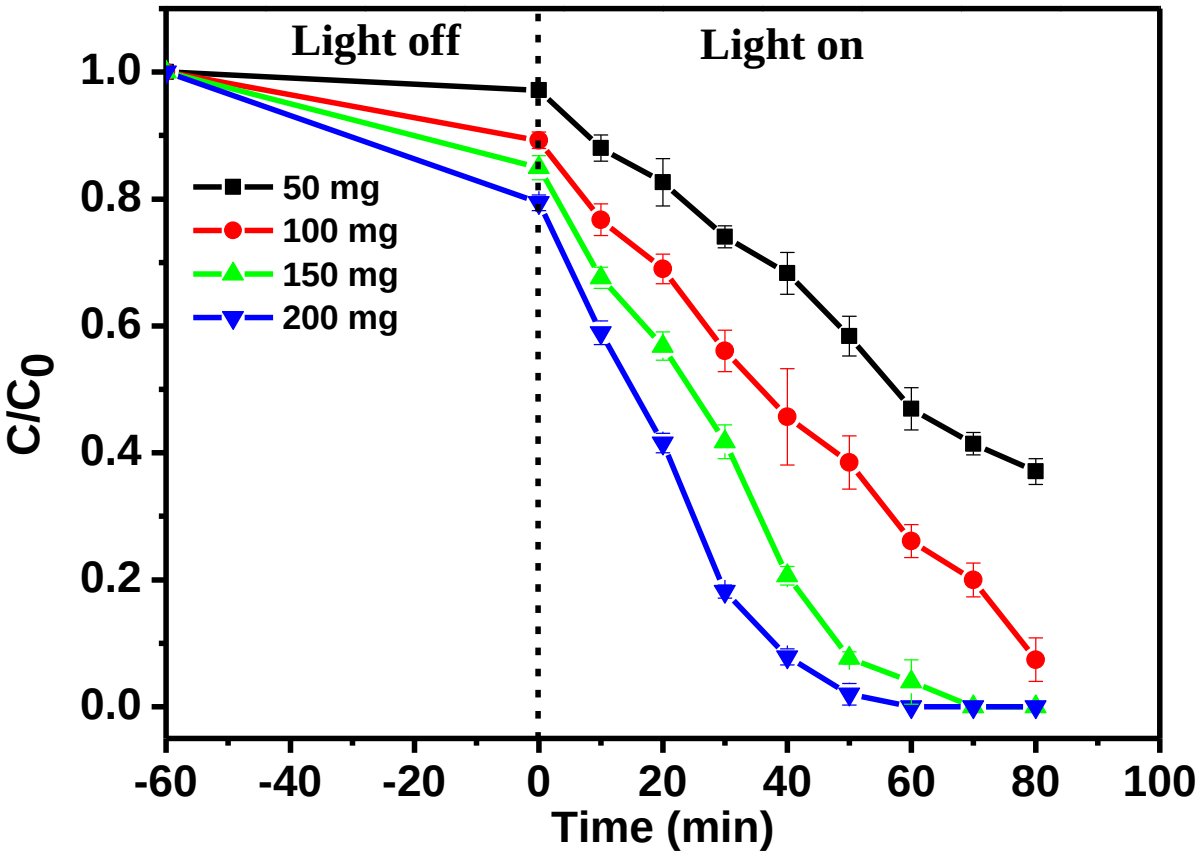



**Figure 5.4.** Influence of $Ti_1Bi_1Bt_2$ dosage on the removal of phenol under visible light irradiation.

## 5.4. The effect of initial concentration on the removal of phenol

The initial concentration of phenol was varied from 10 to 100 ppm under an optimum catalyst dosage of 150 mg at pH 4 and the results are presented in **Figure 5.5.** $Ti_1Bi_1Bt_2$ completely degraded the 10 ppm and 20 ppm of phenol within 60 and 70 min respectively. However, for 30, 50, and 100 ppm the photodegradation efficiency was in the order 90.2, 61.0 and 37.2% respectively after 80 min. This was not surprising as the increase in the concentration of phenol is expected to result in a competition for the limited photocatalytic active surface area of $Ti_1Bi_1Bt_2$. Sometimes fouling may occur such that the photocatalyst is deactivated, but $TiO_2$/clay materials are known to resist fouling through dispersion-photodegradation synergic action on the concentrated solution [8,9]. Since $Ti_1Bi_1Bt_2$ acts in a circulating "adsorb, degrade and release mechanism" of phenol and degradation products, therefore if more molecules become adsorbed, then the rate of degradation and mineralization in the active photocatalytic sites drops due to the drop in the number of active sites available to the phenol molecules. The high number of phenol molecules that get adsorbed on the $Ti_1Bi_1Bt_2$ also reduces the photons

reaching the surface of the photocatalyst surface [10]. The latest available data, indicates that phenol exists in concentrations up to 140 ng/L in river waters [11] and up to 163 µg/L in wastewater treatment plants [12] in South Africa. These concentration dat are so low compared to the 20 ppm used for further investigations.

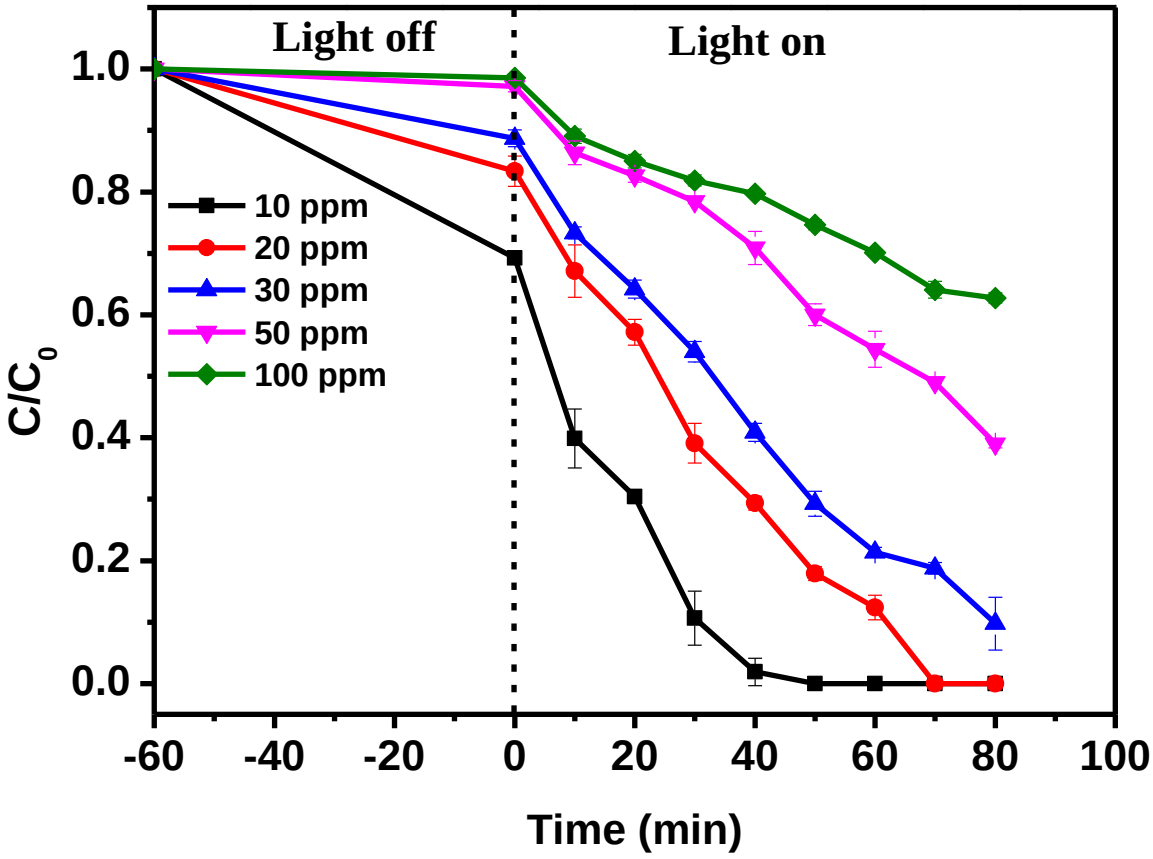



**Figure 5.5.** Influence of initial concentration on the removal of phenol over $Ti_1Bi_1Bt_2$ under visible light irradiation.

## 5.5. Kinetic Studies

A kinetic study was done on the photodegradation of 100 mL of 20 ppm phenol on 150 mg of $Ti_1Bi_1Bt_2$ at pH 4. **Table 5.1** and **Figure 5.6** show the rate constant of the relevant Langmuir−Hinshelwood kinetics. The rate constant was calculated by fitting the experimental data into the pseudo-first-order kinetic **equation 5.2** [13]:

$$ln\left(\frac{C_0}{C}\right) = K_{app}t \qquad \textbf{5.2}$$

where $C_0$ is the initial concentration before irradiation, $C$ is the initial and final concentration, $K_{app}$ is the apparent rate constant, and $t$ is the irradiation time.

As can be seen in **Table 5.1** and **Figure 5.6**, phenol photodegradation on $Ti_1Bi_1Bt_2$ is better approximated by a linear plot explained by pseudo-first-order kinetics where $K_{app}$ = 0.0322 $min^{-1}$ and $R^2$ = 0.972. The observed pseudo-first-order reaction kinetics of phenol degradation in this study is consistent with most $TiO_2$/clay-based photodegradation of organics [14,15].

**Table 5.1. Rate constant ($K_{app}$) for the photodegradation of phenol using $Ti_1Bi_1Bt_2$.**

| **Photocatalyst** | **Apparent rate constant, $K_{app}$ ($min^{-1}$)** | **$R^2$** |
|---|---|---|
| $Ti_1Bi_1Bt_2$ | 0.0322 | 0.972 |

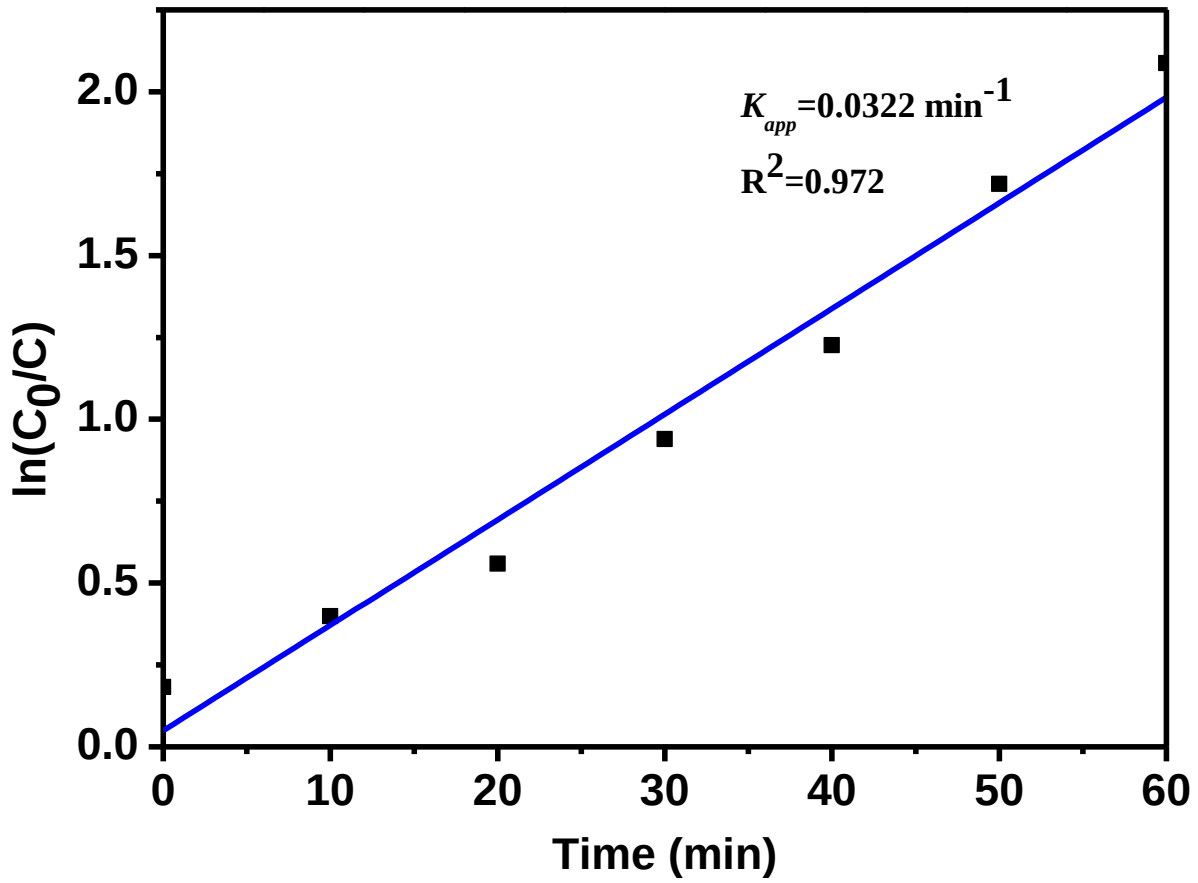



**Figure 5.6.** Pseudo-first-order reaction kinetics of the photodegradation of 20 ppm phenol over 150 mg of $Ti_1Bi_1Bt_2$.

## 5.6. Catalyst reusability studies

**Figure 5.7** and **Table 5.2** show the photocatalytic efficiency of the photodegradation of 100 mL of phenol on 150 mg of $Ti_1Bi_1Bt_2$ at pH 4 after six photocatalytic cycles. As can be seen, $Ti_1Bi_1Bt_2$ still exhibited satisfactory phenol photodegradation efficiency above 83% after 6 photocatalytic cycles demonstrating satisfactory reusability.

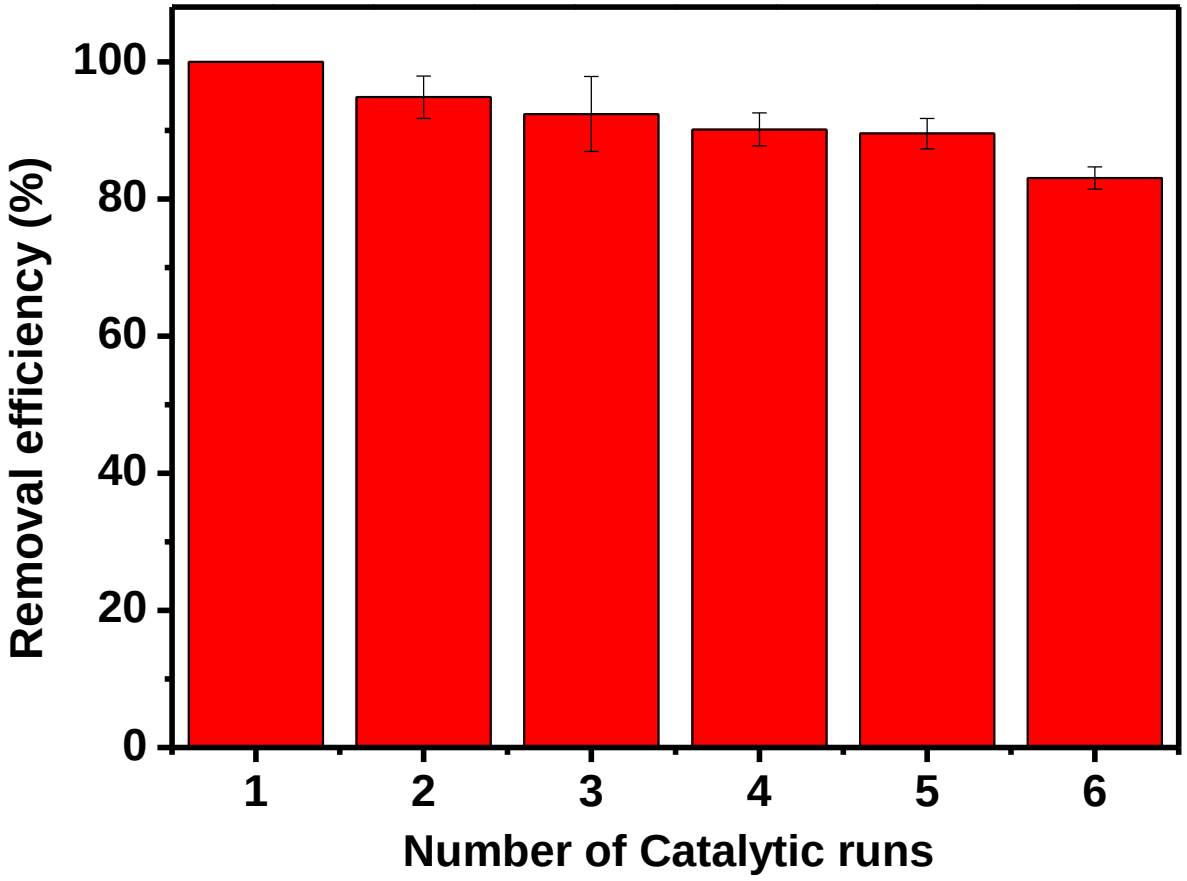



**Figure 5.7.** Reusability performance of $Ti_1Bi_1Bt_2$ during the first six photocatalytic runs towards phenol.

PXRD, SEM images, and $N_2$ adsorption-desorption analyses of fresh and recycled $Ti_1Bi_1Bt_2$ were compared to investigate structural changes induced by the repeated use of the photocatalyst. The properties of the reused $Ti_1Bi_1Bt_2$ are shown in **Figures S3-S6** and **Table S1-S2**. According to PXRD analysis, the continuous reuse of $Ti_1Bi_1Bt_2$ reduced its crystallinity as seen by the suppression of the peak intensities and broadening of peaks from the diffractogram (**Figure S3**). Moreover, $Ti_1Bi_1Bt_2$ still maintained good structural integrity as there was no change in the positions of its crystallographic planes and surface morphology as

shown by the SEM image in **Figure S4**. Furthermore, the photocatalyst maintained its elemental composition (**Figure S5**). However, there was a slight drop in the BET surface area of $Ti_1Bi_1Bt_2$ from 124.8 $m^2/g$ to 106.7 $m^2/g$ (**Table S2** and **Figure 6**) after 6 photocatalytic cycles attributed to possible poisoning or blockage of the active sites.

**Table 5.2. Phenol conversion efficiency on $Ti_1Bi_1Bt_2$ after 6 photocatalytic cycles.**

| Number of runs | Phenol conversion (%) after 80 min | Sample standard Deviation |
|---|---|---|
| 1 | 100 | 0 |
| 2 | 94.9 | 3.10 |
| 3 | 92.4 | 5.46 |
| 4 | 90.2 | 2.40 |
| 5 | 89.5 | 2.23 |
| 6 | 83.1 | 1.63 |

.

## 5.7. Free radical scavenging experiments

The typical mode of basic single-electron semiconductor photocatalysis is through the surface interfacial $e^-/O_2^{\bullet-}$ and the $h^+/OH^\bullet$ redox routes. Depending on the nature of the semiconductor photocatalyst or composite used, either or both of the aforementioned routes exert significance in describing the photocatalytic process. Free radical scavenging experiments were performed to identify the dominant reactive oxidation species (ROS) responsible for the photocatalytic degradation process viz: electron ($e^-$), holes ($h^+$), $OH^\bullet$, and $O_2^{\bullet-}$. Electrons were scavenged using $AgNO_3$ [16,17], holes were captured using ammonium oxalate (AO) [17,18], $OH^\bullet$ were trapped using isopropanol (IPA) [17,19], and $O_2^{\bullet-}$ were scavenged using benzoquinone (BQ) [16,17].

The concentration of BQ [4], AO, and $AgNO_3$ was fixed at 1 mmol/L while that of IPA was fixed at 10 mmol/L [4]. The efficiency of phenol degradation in the presence of the radical scavengers is presented in **Figure 5.8** and **Table 5.3**. A blank (phenol without the scavengers) was also used as a control during the scavenging investigation.

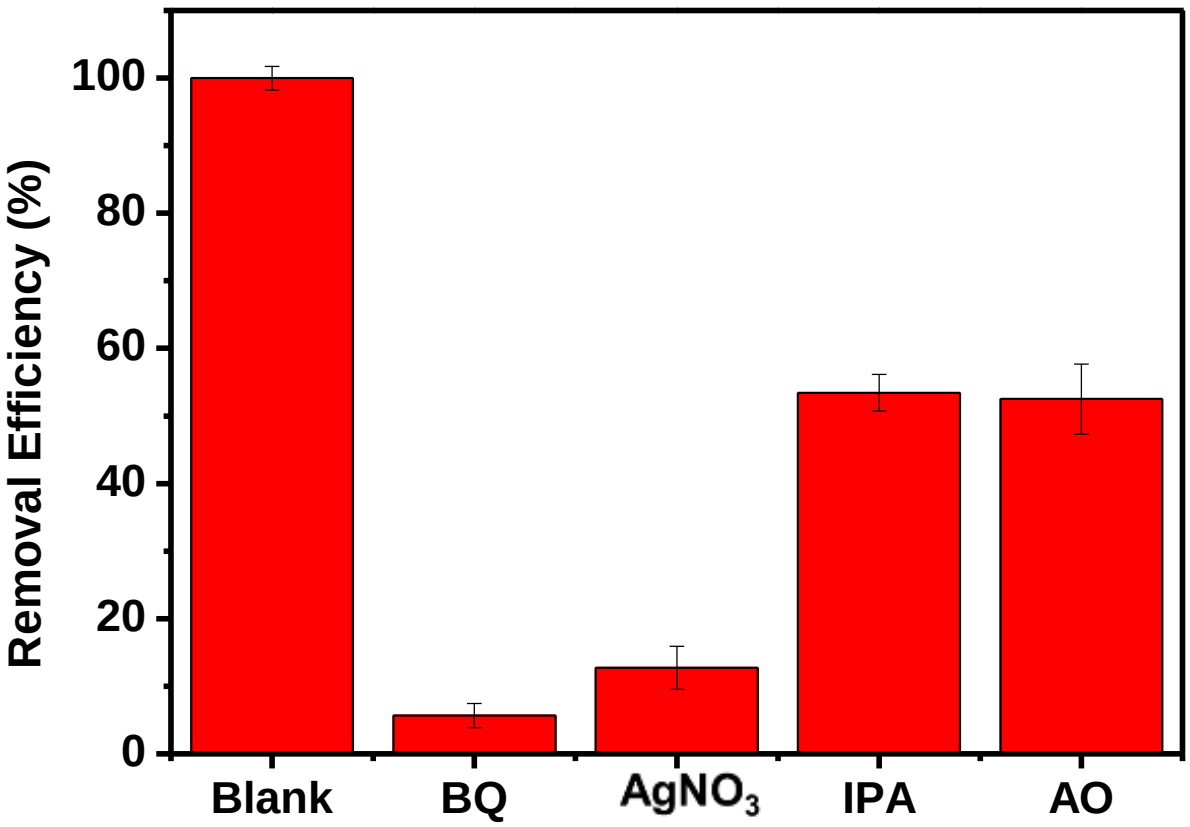



**Figure 5.8.** Photocatalytic removal of phenol on $Ti_1Bi_1Bt_2$ in the presence of scavengers of ROS.

**Table 5.3. Phenol conversion efficiency on $Ti_1Bi_1Bt_2$ in the presence of scavengers for ROS.**

| Scavenger | Phenol conversion (%) after 80 min | Sample Standard Deviation |
|---|---|---|
| Blank | 99.4 | 1.74 |
| Benzoquinone (BQ) | 5.67 | 1.80 |
| $AgNO_3$ | 12.7 | 3.18 |
| Ispropanol (IPA) | 53.4 | 2.69 |
| Ammonium oxalate (AO) | 52.5 | 5.19 |

As can be seen in **Figure 5.8** and **Table 5.3**, the presence of AO to capture holes reduces the phenol photodegradation efficiency to (52.5%) which is about half. This suggests that holes play a significant role in the photocatalysis of phenol on $Ti_1Bi_1Bt_2$. If not captured, holes have a strong tendency to react with adsorbed water molecules and surface hydroxyl groups

generating the $OH^{\bullet}$ which further react with organic molecules [17]. In the presence of small organic molecules such as IPA in the phenol solution, the generated $OH^{\bullet}$ preferentially reacts with IPA molecules instead of the stable aromatic phenol. Since the presence of IPA suppresses the photodegradation of phenol by almost half (53.4%), therefore $OH^{\bullet}$ is also among the most important ROS.

In the photocatalytic process with $AgNO_3$, the $Ag^+$ ions were readily reduced by the photogenerated electrons to form zerovalent Ag as shown in **equation 5.3** thereby leading to a significant decrease in the number of electrons that participated in the photocatalytic process [20]. The significant decrease of the photocatalytic efficiency of $Ti_1Bi_1Bt_2$ to 12.7% upon the removal of electrons suggests they are among the most important ROS.

$$Ag^+ + e- \rightarrow Ag^0 \qquad \textbf{5.3}$$

BQ readily traps superoxide radicals according to **equation 5.4** [21] and it was used to remove the superoxide radicals during the photocatalysis of phenol. As can be seen in **Figure 5.8** and **Table 5.3**, the presence of BQ as a superoxide scavenger inhibits the photocatalytic abatement of phenol to 5.67% suggesting the significance of superoxide radicals in the photocatalytic process.

$$BQ + O_2^{\bullet-} \rightarrow BQ^{\bullet-} + O_2 \qquad \textbf{5.4}$$

Through the scavenging studies above, it can be concluded that the photocatalytic degradation of phenol on $Ti_1Bi_1Bt_2$ is driven by the action of electrons, superoxide radicals, holes, and hydroxyl radicals. However, electrons and superoxide radicals exert the highest significance in the photodegradation process as observed by the low phenol removal efficiency in the presence of $AgNO_3$ and BQ.

## 5.8. Proposed charge transfer mechanism and phenol photodegradation

After careful analysis of the characterization techniques coupled with the scavenging experiments, we have rationalized a plausible photogeneration and transport mechanism (**Figure 5.9**) of the charge carriers to form ROS after the irradiation of $Ti_1Bi_1Bt_2$ to participate in the degradation of phenol through interfacial redox reactions on the surface of the photocatalyst.

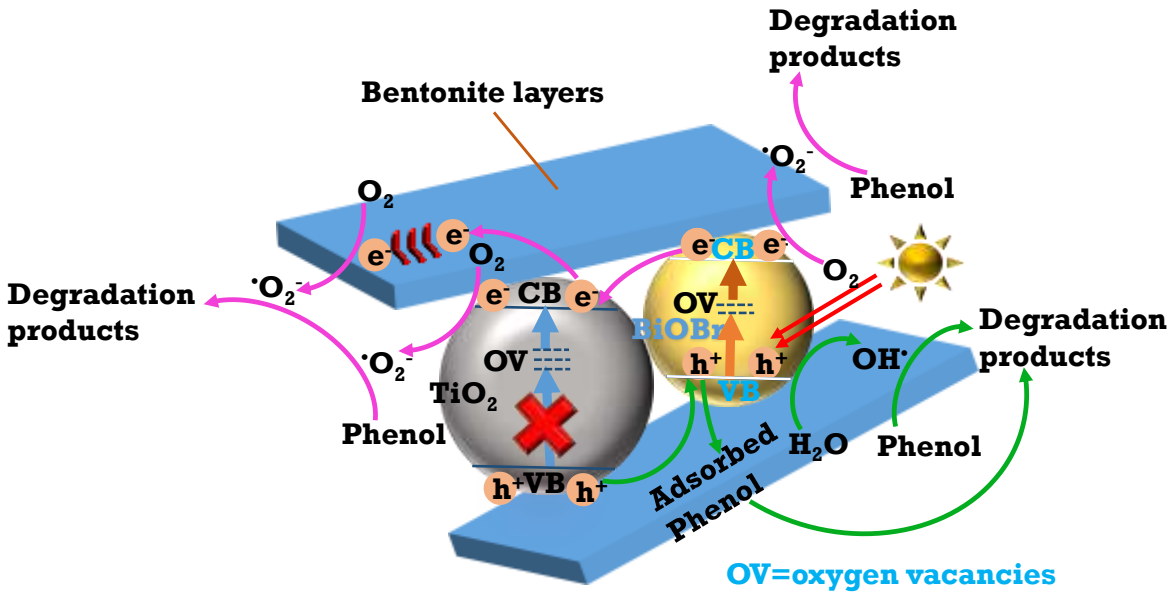



**Figure 5.9.** A proposed conceptual charge transfer mechanism for the degradation of phenol on $Ti_1Bi_1Bt_2$.

## 5.9. Conclusion

$Ti_1Bi_1Bt_2$ exhibited the best photocatalytic activity towards phenol because of its exceptional properties such as high BET surface area, sufficiently low bandgap, and electron-hole recombination rate. The contribution of photolysis in the photocatalytic process is inconsequential. The optimum operational conditions of $Ti_1Bi_1Bt_2$ are pH 4, 150 mg catalyst loading in 100 mL of phenol, and an initial concentration of 20 ppm. Under the optimized operational conditions, 100% is removed within 70 min of visible light irradiation with a pseudo-first-order rate constant of 0.0322 $min^{-1}$. Scavenging experiments demonstrated that superoxide radicals ($O_2^{\bullet-}$), electrons (e−), holes ($h^+$), and hydroxyl radicals ($OH^{\bullet}$) all participated in the phenol photodegradation process. However, electrons and superoxide radicals exerted the highest dominance in the photocatalytic process.

## References


[1] T. Jia, J. Zhang, J. Wu, D. Wang, Q. Liu, Y. Qi, B. Hu, P. He, W. Pan, X. Qi, Synthesis amorphous $TiO_2$ with oxygen vacancy as carriers transport channels for enhancing photocatalytic activity, Mater. Lett. 265 (2020) 127465. https://doi.org/10.1016/j.matlet.2020.127465.

[2] Q. Wang, J. Zhao, Y. Cong, Y. Zhang, Photo-sensitized Degradation of Dye Pollutants on Amorphous $TiO_2$ under Visible Light Irradiation, Chinese J. Catal. 32 (2011) 1076–1082. DOI: 10.3724/SP.J.1088.2011.10336

[3] D. Zywitzki, H. Jing, H. Tuysuz, C.K. Chan, High surface area, amorphous titania with reactive $Ti^{3+}$ through a photo-assisted synthesis method for photocatalytic $H_2$ generation, J. Mater. Chem. A. 5 (2017) 10957–10967. https://doi.org/10.1039/c7ta01614j.

[4] E. Tao, X. Xiao, S. Yang, A new synthesizing method of $TiO_2$ with montmorillonite : Effective photoelectron transfer to degrade Rhodamine B, Sep. Purif. Technol. 258 (2021) 118070. https://doi.org/10.1016/j.seppur.2020.118070.

[5] A. El Gaidoumi, A. Arrahli, A. Loqman, F. Baragh, B. El Bali, A. Kherbeche, Efficient Sol-gel Nanocomposite $TiO_2$-clay in Photodegradation of Phenol: Comparison to Labe-made and Commercial Photocatalysts, Silicon. (2021). https://doi.org/10.1007/s12633-021-01275-1.

[6] J. Sabbineni, Phenol-An effective antibacterial Agent, J. Med. Org. Chem. 3 (2016) 182–191.

[7] R.J. Mayer, M. Breugst, N. Hampel, A.R. Ofial, H. Mayr, Ambident Reactivity of Phenolate Anions Revisited: A Quantitative Approach to Phenolate Reactivities, J. Org. Chem. 84 (2019) 8837–8858. https://doi.org/10.1021/acs.joc.9b01485.

[8] C. Li, L. Yan, Y. Li, D. Zhang, M. Bao, L. Dong, $TiO_2$@ palygorskite composite for the efficient remediation of oil spills via a dispersion-photodegradation synergy, Front. Environ. Sci. Eng. 15 (2021) 72. https://doi.org/10.1007/s11783-020-1365-3

[9] M.C. Dlamini, M.S. Maubane-Nkadimeng, J.A. Moma, The use of $TiO_2$/clay heterostructures in the photocatalytic remediation of water containing organic pollutants: A review, J. Environ. Chem. Eng. 9 (2021) 106546. https://doi.org/10.1016/j.jece.2021.106546.

[10] S.S. Sambaza, A. Maity, K. Pillay, Polyaniline-coated $TiO_2$ nanorods for photocatalytic degradation of bisphenol A in water, ACS Omega. 5 (2020) 29642–29656. https://doi.org/10.1021/acsomega.0c00628.

[11] A. Yahaya, O.O. Okoh, F.O. Agunbiade, A.I. Okoh, Occurrence of phenolic derivatives in Buffalo River of Eastern Cape South Africa: Exposure risk evaluation, Ecotoxicol. Environ. Saf. 171 (2019) 887–893. https://doi.org/10.1016/j.ecoenv.2019.01.037.

[12] O.O. Olujimi, O.S. Fatoki, J.P. Odendaal, A.P. Daso, Chemical monitoring and temporal variation in levels of endocrine-disrupting chemicals (priority phenols and phthalate esters) from selected wastewater treatment plant and freshwater systems in Republic of South Africa, Microchem. J. 101 (2012) 11–23. https://doi.org/10.1016/j.microc.2011.09.011.

[13] N.G. Asenjo, R. Santamaría, C. Blanco, M. Granda, P. Álvarez, R. Menéndez, Correct use of the Langmuir-Hinshelwood equation for proving the absence of a synergy effect in the photocatalytic degradation of phenol on a suspended mixture of titania and activated carbon, Carbon 55 (2013) 62–69. https://doi.org/10.1016/j.carbon.2012.12.010.

[14] W. Chen, H. Xiao, H. Xu, T. Ding, Y. Gu, Photodegradation of methylene blue by $TiO_2$-$Fe_3O_4$-bentonite magnetic nanocomposite, Int. J. Photoenergy. 2015 (2015) 7. https://doi.org/10.1155/2015/591428.

[15] A. Mishra, A. Mehta, S. Basu, Clay supported $TiO_2$ nanoparticles for photocatalytic degradation of environmental pollutants : A review, Journal of Environmental Chemical Engineering 6 (2018) 6088–6107. https://doi.org/10.1016/j.jece.2018.09.029.

[16] C. Li, Z. Sun, W. Zhang, C. Yu, S. Zheng, Environmental Highly efficient g-$C_3N_4$/$TiO_2$/kaolinite composite with novel three-dimensional structure and enhanced visible-light responding ability towards ciprofloxacin and S. aureus, Appl. Catal. B Environ. 220 (2018) 272–282. https://doi.org/10.1016/j.apcatb.2017.08.044.

[17] W. Li, D. Li, Y. Lin, P. Wang, W. Chen, X. Fu, Y. Shao, Evidence for the active species involved in the photodegradation process of methyl Orange on $TiO_2$, J. Phys. Chem. C. 116 (2012) 3552–3560. https://doi.org/10.1021/jp209661d.

[18] M.A. Islam Molla, I. Tateishi, M. Furukawa, H. Katsumata, T. Suzuki, S. Kaneco,

Evaluation of Reaction Mechanism for Photocatalytic Degradation of Dye with Self-Sensitized $TiO_2$ under Visible Light Irradiation, Open J. Inorg. Non-Metallic Mater. 07 (2017) 1–7. https://doi.org/10.4236/ojinm.2017.71001.

[19] K. Lv, Y. Xu, Effects of polyoxometalate and fluoride on adsorption and photocatalytic degradation of organic dye X3B on $TiO_2$: The difference in the production of reactive species, J. Phys. Chem. B. 110 (2006) 6204–6212. https://doi.org/10.1021/jp055228t.

[20] J. Qi, K. Zhao, G. Li, Y. Gao, H. Zhao, R. Yu, Z. Tang, Multi-shelled $CeO_2$ hollow microspheres as superior photocatalysts for water oxidation, Nanoscale. 6 (2014) 4072–4077. https://doi.org/10.1039/c3nr06822f.

[21] R. Palominos, J. Freer, M.A. Mondaca, H.D. Mansilla, Evidence for hole participation during the photocatalytic oxidation of the antibiotic flumequine, J. Photochem. Photobiol. A Chem. 193 (2008) 139–145. https://doi.org/10.1016/j.jphotochem.2007.06.017.

# Chapter 6: General conclusions and recommendations

## 6.0. Introduction

This is the last chapter of the dissertation and it discusses general conclusions and recommendations for future work.

## 6.1. Conclusion

A-$TiO_2$-BiOBr-Bt multidimensional heterostructures with 1:3:4, 1:1:2, and 3:1:4 mass ratios of A-$TiO_2$, BiOBr, and Bt respectively were successfully synthesized using a solvothermal process, characterized and applied in the photodegradation of phenol. The morphological analysis confirmed the formation of mesoporous A-$TiO_2$-BiOBr-Bt heterostructures with high BET surface areas. Among the ternary heterostructures, $Ti_1Bi_1Bt_2$ exhibited the best photocatalytic activity towards phenol under visible light irradiation attributed to its high light-harvesting ability, good charge transfer efficiency, and high BET surface area. Furthermore, $Ti_1Bi_1Bt_2$ exhibited good recyclability and structural stability as it maintained removal efficiency of phenol above 83% after 6 photocatalytic cycles. Based on scavenging experiments, the electrons, superoxide radical, holes, and hydroxyl radicals all participated in the photodegradation of phenol.

Moreover, the as-synthesized $Ti_1Bi_1Bt_2$ composite gave high phenol conversion efficiency and compares well to common $TiO_2$/clay-based composites except for Ag-$TiO_2$/Bt which is highly effective as shown in **Table 6.1**. Despite having lower efficiency than Ag-$TiO_2$/Bt, $Ti_1Bi_1Bt_2$ is relatively cheaper due to the high cost of Ag compared to BiOBr.

**Table 6.1. $TiO_2$/clay-based composites applied in the removal of phenol under visible light**

| **$TiO_2$/clay composite** | **Dosage (mg/mL)** | **Initial phenol concentration** | **Conversion efficiency (%)** | **Rate constant ($min^{-1}$)** | **Reaction time (min)** | **Ref.** |
|---|---|---|---|---|---|---|
| $TiO_2$/Mt | 1 | 10 ppm | - | $8.13\times 10^{-3}$ | 120 | [1] |
| Ce-$TiO_2$/Mt | 0.5 | 25 mg/L | 80 | - | 600 | [2] |

| | | | | | | |
|---|---|---|---|---|---|---|
| Fe-$TiO_2$/Bt | 5 | $5 \times 10^{-4}$ M | *ca.* 90 | - | 240 | [3] |
| Ag-$TiO_2$/Bt | 1.7 | 100 mg/L | 98.84 | - | 90 | [4] |
| A-$TiO_2$-BiOBr-Bt | 1.5 | 20 ppm | 100 | 0.0322 | 70 | This study |

In conclusion, this study presents an insight into the fabrication of cheap, visible-light-driven A-$TiO_2$/clay-based photocatalysts for the treatment of water containing organic pollutants. The as-synthesized "green chemistry" photocatalyst has potential use in coating the inner lining of clay pots and other containers which can be used for the treatment of drinking water from rivers. Therefore, this study has strong relevance in the remediation of water in the South African context where some people still drink untreated river water and phenol concentrations are below 20 ppm but higher than the USEPA recommended concentrations.

## 6.2. Recommendations

While an effort has been made to thoroughly characterize and investigate the photocatalytic activity of the materials there are some areas of this study worth exploring. We recommend that:

- Electron Impedance Spectroscopy (EIS) studies should be conducted to validate the electron-hole recombination rates of the materials as the PL spectra of the A-$TiO_2$-BiOBr-Bt ternary materials are close to differentiate with confidence.
- Electron Paramagnetic Resonance (EPR) should be performed to qualitatively compare the number of oxygen vacancies in the materials and rationalize their effect on their photocatalytic performance.
- HPLC/MS analysis should be used to identify the photodegradation intermediates to propose a mechanism showing how the intermediates are likely generated and how they disappear with time during photodegradation.

## References


[1] Z. Ding, H.Y. Zhu, G.Q. Lu, P.F. Greenfield, Photocatalytic Properties of Titania Pillared Clays by Different Drying Methods, J. Colloid Interface Sci. 209 (1999) 193–199.

[2] C. Belver, J. Bedia, M.A. Álvarez-Montero, J.J. Rodriguez, Solar photocatalytic purification of water with Ce-doped $TiO_2$/clay heterostructures, Catal. Today. 266 (2016) 36–45. https://doi.org/10.1016/j.cattod.2015.09.025.

[3] J.G. Carriazo, M. Moreno-Forero, R.A. Molina, S. Moreno, Incorporation of titanium and titanium-iron species inside a smectite-type mineral for photocatalysis, Appl. Clay Sci. 50 (2010) 401–408. https://doi.org/10.1016/j.clay.2010.09.007.

[4] D. Bang, T. Dieu, C. Nguyen, T. Phuong, H. Thuan, Preparation, characterization, and evaluation of catalytic activity of titania modified with silver and bentonite, J. Ind. Eng. Chem. 18 (2012) 1764–1767. https://doi.org/10.1016/j.jiec.2012.04.004.

[5] A. Yahaya, O.O. Okoh, F.O. Agunbiade, A.I. Okoh, Occurrence of phenolic derivatives in Buffalo River of Eastern Cape South Africa: Exposure risk evaluation, Ecotoxicol. Environ. Saf. 171 (2019) 887–893. https://doi.org/10.1016/j.ecoenv.2019.01.037.

[6] O.O. Olujimi, O.S. Fatoki, J.P. Odendaal, A.P. Daso, Chemical monitoring and temporal variation in levels of endocrine-disrupting chemicals (priority phenols and phthalate esters) from selected wastewater treatment plant and freshwater systems in Republic of South Africa, Microchem. J. 101 (2012) 11–23. https://doi.org/10.1016/j.microc.2011.09.011.

# Appendix A: Supplementary information

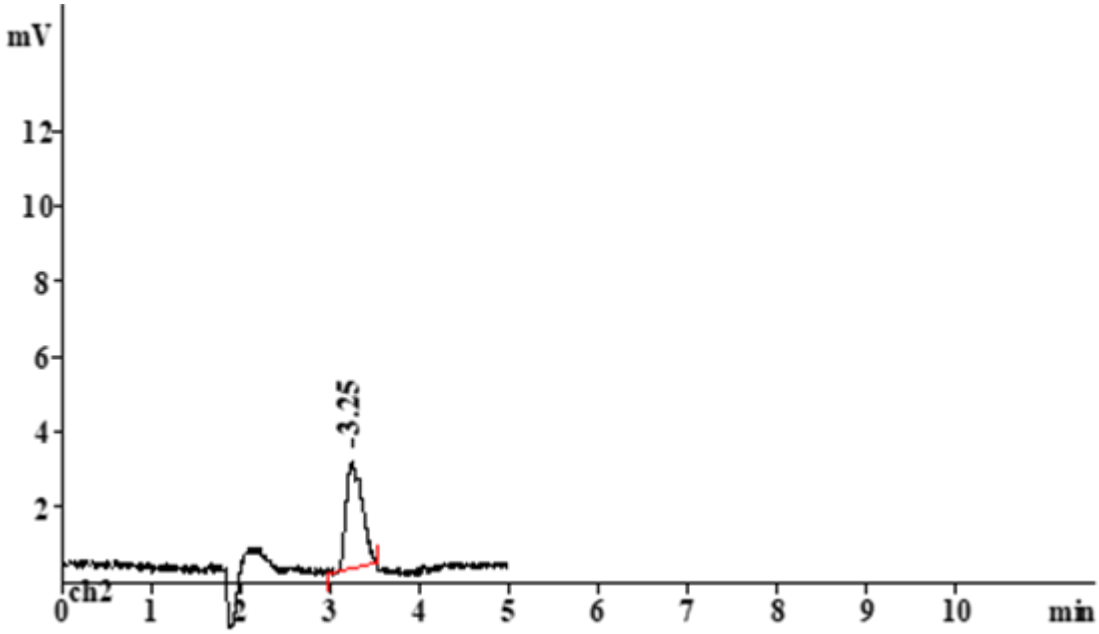



**Figure S1**. A typical chromatogram of an external phenol standard with a 3.25 min retention time, used in calibrating the concentration of phenol during HPLC analyses.

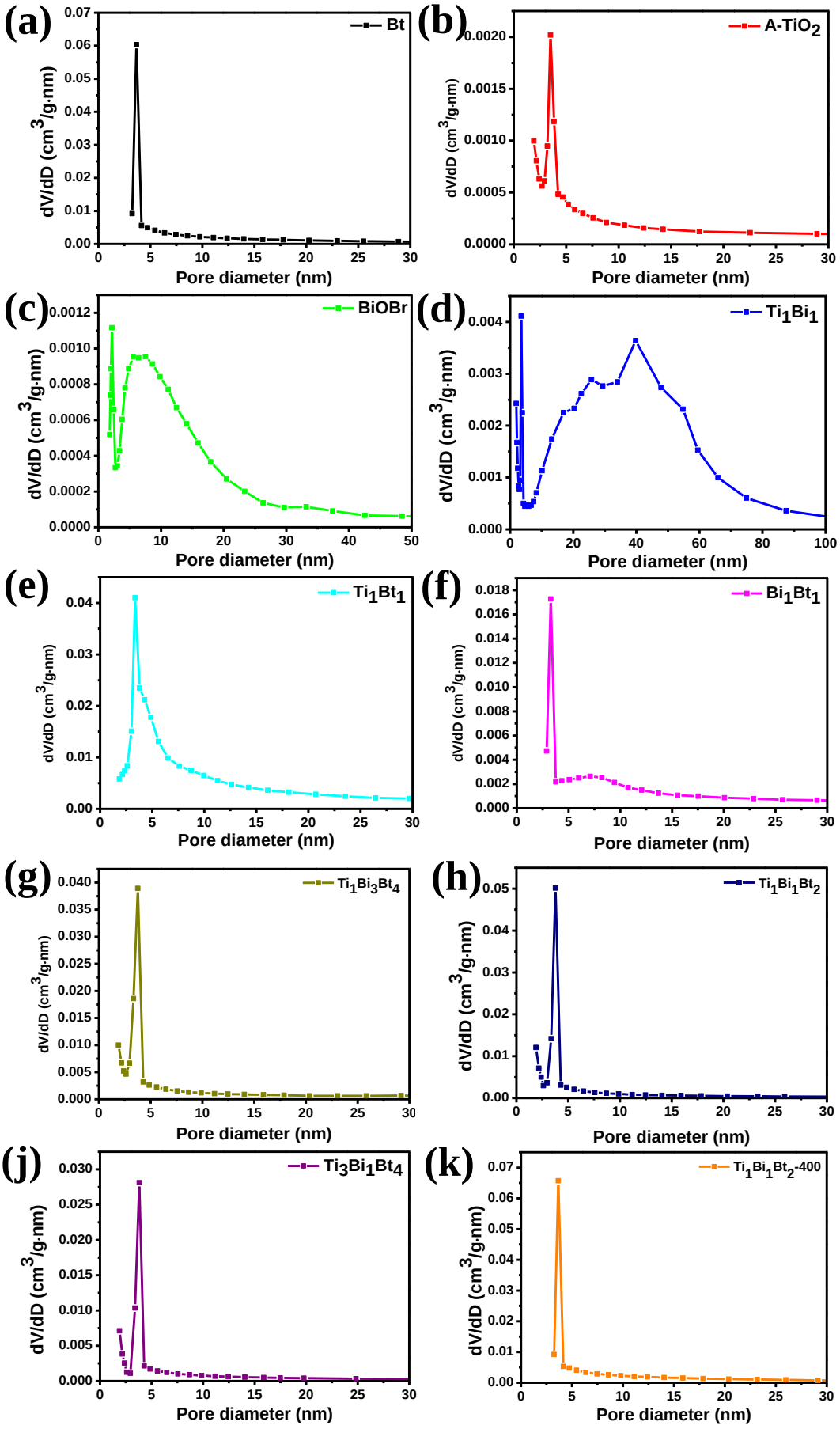



**Figure S2**. Pore size distribution curves of Bt and all the photocatalysts.

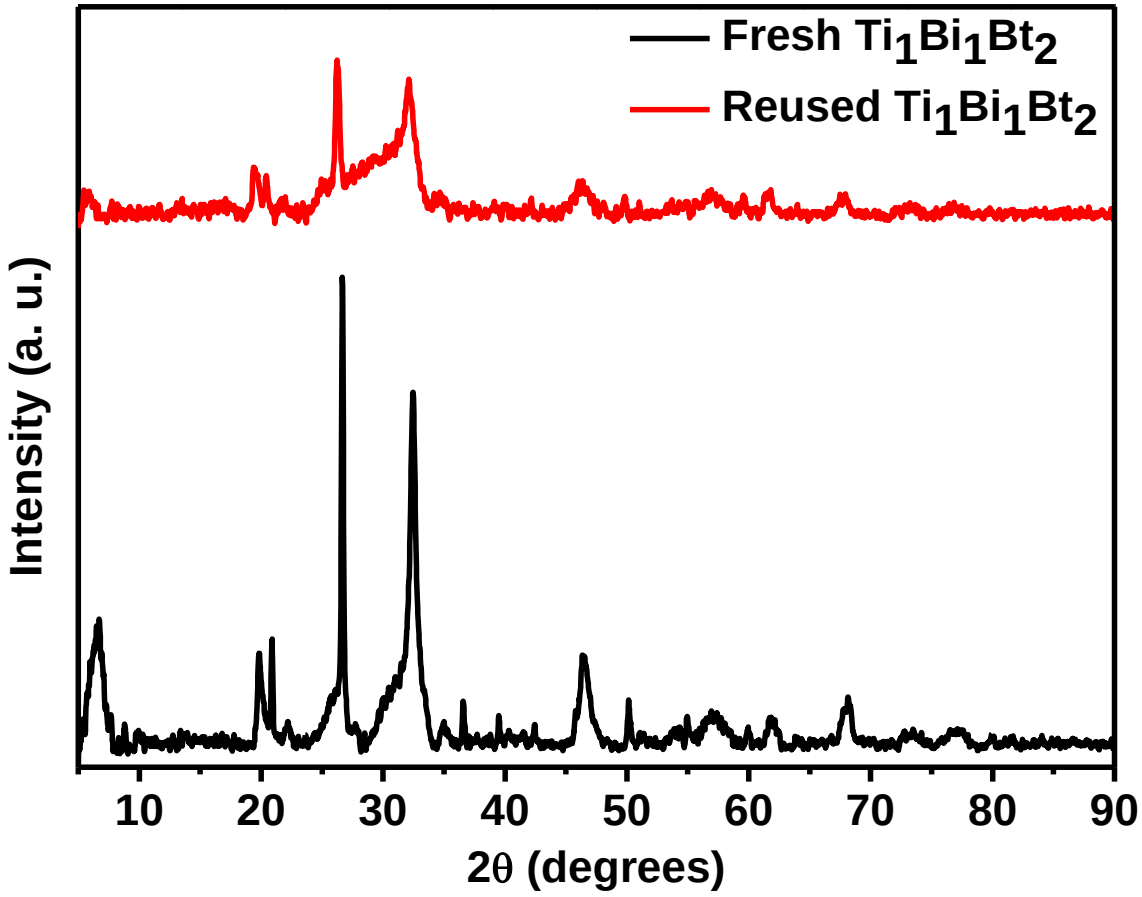



**Figure S3**. PXRD diffractogram of $Ti_1Bi_1Bt_2$ before and after being used in 6 photocatalytic cycles.

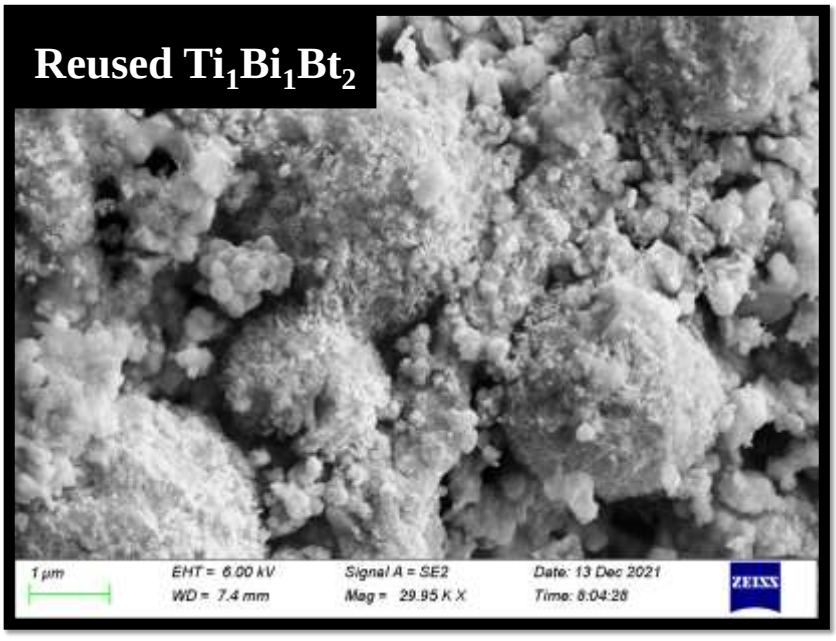



**Figure S4**. SEM micrograph of $Ti_1Bi_1Bt_2$ after being used in 6 photocatalytic cycles.

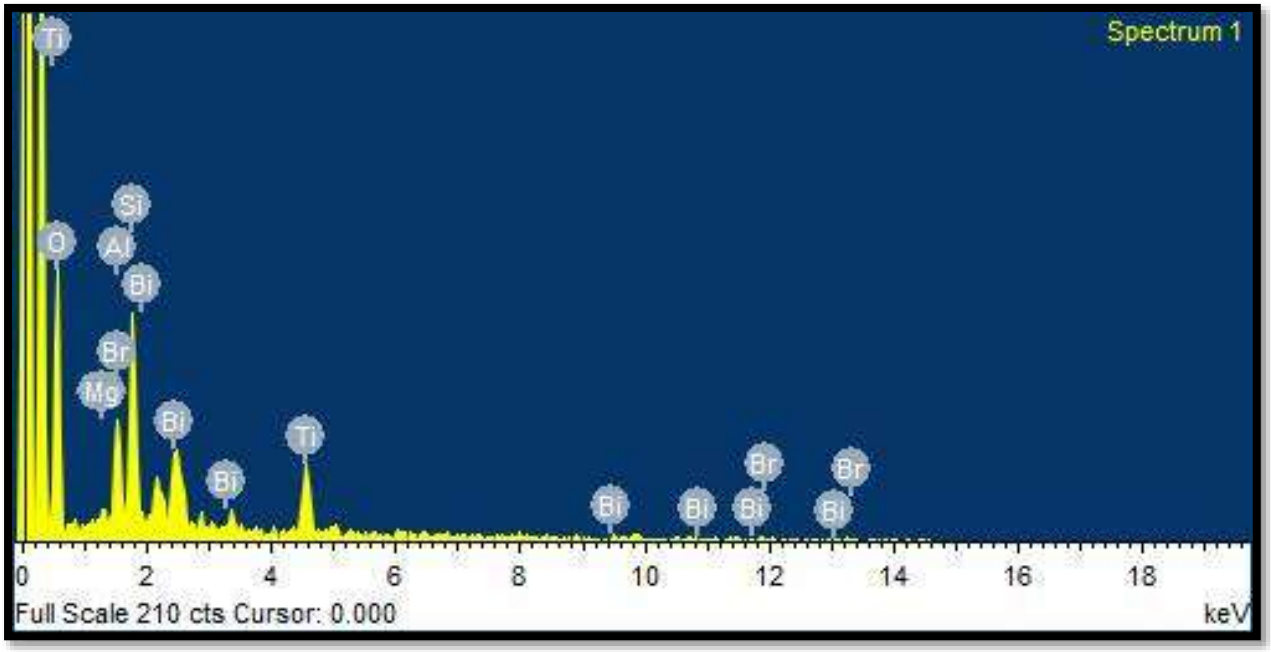



**Figure S5**. EDS spectra of $Ti_1Bi_1Bt_2$ after being used in 6 photocatalytic cycles.

**Table S1. Elemental composition of $Ti_1Bi_1Bt_2$ after being used in 6 photocatalytic cycles.**

| Atomic (%) of all the elements reused $Ti_1Bi_1Bt_2$ | | | | | | | | | |
|---|---|---|---|---|---|---|---|---|---|
| **Na** | **K** | **Mg** | **Fe** | **Al** | **Si** | **Ti** | **Bi** | **O** | **Br** |
| - | - | 0.55 | - | 4.89 | 9.36 | 6.42 | 2.25 | 76.43 | 0.10 |

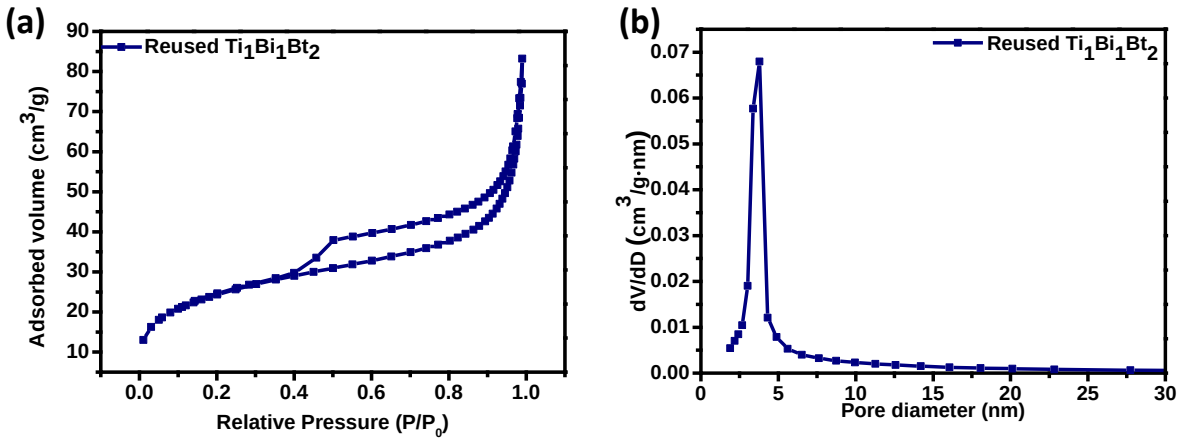



**Figure S6**. BET isotherm and pore size distribution curve for $Ti_1Bi_1Bt_2$ after being used in 6 photocatalytic cycles.

**Table S2. BET Specific Surface Area, Pore Volume, and Pore size of reused $Ti_1Bi_1Bt_2$.**

| Sample | BET surface area ($m^2/g$) | Pore volume ($cm^3/g$) | Pore size (nm) |
|---|---|---|---|
| $Ti_1Bi_1Bt_2$ | 106.7 | 0.112 | 5.5 |